

Università degli Studi di Napoli “Federico II”



Facoltà di Scienze Matematiche, Fisiche e Naturali

Tesi di Dottorato in Fisica

XIX ciclo

Dalitz plot analysis of $\eta \rightarrow \pi^0 \pi^0 \pi^0$
with KLOE experiment

Dott. Francesco Perfetto

Coordinator:
Prof. Gennaro Miele

Supervisors:
Prof. Marco Napolitano
Dott. Fabio Ambrosino

Contents

Introduction	1
1 The KLOE experiment at DAΦNE	3
1.1 The collider DAΦNE	3
1.2 The DAΦNE luminosity at KLOE	5
1.3 The KLOE detector	7
1.3.1 The beam-pipe	8
1.3.2 The drift chamber	8
1.3.3 The electromagnetic calorimeter	12
1.3.4 The quadrupole calorimeters (QCAL)	18
1.4 The trigger system	20
1.5 The data acquisition system	23
1.6 MonteCarlo: detector simulation and physics generators	25
2 Physics at KLOE and η in $3\pi^0$ decay	27
2.1 Kaon physics	28
2.1.1 Semileptonic K_L decays and the K_L lifetime	28
2.1.2 Measurement of the absolute Branching Ratio $K^+ \rightarrow \mu^+ \nu_\mu(\gamma)$	29
2.1.3 Measurement of the K^\pm semileptonic decays absolute Branching Ratios	30
2.1.4 Measurement of the charged kaon lifetime	31
2.1.5 V_{us} extraction	32
2.2 ϕ -radiative decays	34
2.2.1 $\phi \rightarrow f_0(980)\gamma \rightarrow \pi^+\pi^-\gamma$ and $\phi \rightarrow f_0(980)\gamma \rightarrow \pi^0\pi^0\gamma$	35
2.2.2 $BR(\phi \rightarrow \eta'\gamma)/BR(\phi \rightarrow \eta\gamma)$	37
2.3 Hadronic cross-section	39
2.4 $\eta \rightarrow 3\pi^0$ within a chiral approach	40
2.4.1 Standard Chiral Perturbation Theory	41
2.4.2 Chiral symmetry	42
2.4.3 Effective chiral Lagrangian	45

2.4.4	$\eta \rightarrow \pi^0\pi^0\pi^0$ decay	47
2.5	Dalitz plot of $\eta \rightarrow \pi^0\pi^0\pi^0$ decay	49
2.5.1	Theoretical and experimental results on the Dalitz plot parameter	51
3	Data reconstruction and event classification	53
3.1	Data reconstruction	53
3.1.1	Clustering	53
3.1.2	Tracking	56
3.1.3	Vertexing	58
3.2	The background rejection filter: FILFO	58
3.3	Event Classification: EVCL	59
4	Selection of $\eta \rightarrow \pi^0\pi^0\pi^0$ decays	61
4.1	Event Classification: fully neutral radiative decays	62
4.2	Topological selection of the $\phi \rightarrow \eta\gamma \rightarrow 7\gamma$ events	64
4.3	Kinematic fit	64
4.4	Photon pairing	67
5	Analysis	75
5.1	Resolution and efficiency	75
5.2	Fit of Dalitz-plot procedure	80
5.2.1	Testing of goodness of fit	81
5.3	Analysis on MonteCarlo	82
5.4	Data sample	85
5.5	Analysis on data	86
5.6	The systematic checks	89
5.6.1	Systematics on resolution	89
5.6.2	Systematics on efficiency evaluation	92
5.6.3	Systematics on background evaluation	96
5.6.4	M_η value on data	98
5.6.5	Fit range	98
5.7	Results	100
	Conclusions	103
A		105
A.1	The method of maximum likelihood	105
	Bibliografia	109

List of Figures

1.1	<i>Scheme of the DAΦNE collider apparatus.</i>	4
1.2	<i>Integrated luminosity in pb^{-1} as function of the number of days of data taking for the years 2001 ÷ 2005.</i>	6
1.3	<i>Last KLOE run peak and integrated luminosity.</i>	6
1.4	<i>Section of the KLOE detector.</i>	7
1.5	<i>The beam-pipe.</i>	8
1.6	<i>The KLOE drift chamber at the end of the wire stringing.</i>	9
1.7	<i>Drift cells configuration at $z = 0$; a portion of chamber at boundary between small cells (inner layers) and big cells (outer layers) is shown. Full dots indicate sense wires, circles indicate field wires.</i>	10
1.8	<i>KLOE drift chamber geometry: the z-axis is defined along the beam direction. The stereo angle ε_k is defined in such a way that the stereo drop δ is constant.</i>	11
1.9	<i>Example of hardware and software efficiency for a small cell.</i>	12
1.10	<i>Momentum resolution as function of polar angle, using Bhabha events.</i>	12
1.11	<i>The KLOE calorimeter.</i>	13
1.12	<i>Schematic view of the fiber-lead composite of each module of the electromagnetic calorimeter.</i>	14
1.13	<i>(Top) Linearity of the calorimeter energy response as a function of the photon energy; (Bottom) energy resolution of the calorimeter as a function of the photon energy. The two curves are evaluated with radiative Bhabha events.</i>	15
1.14	<i>Time resolution of the calorimeter as a function of the photon energy, for radiative ϕ decays.</i>	16
1.15	<i>Photon detection efficiency using: $e^+e^-\gamma$ (Bhabha radiative), $\phi \rightarrow \pi^+\pi^-\pi^0$, $K_L \rightarrow \pi^+\pi^-\pi^0$.</i>	17
1.16	<i>Schematic view of a quadrupole calorimeter.</i>	19
1.17	<i>Trigger scheme.</i>	21
1.18	<i>Scheme of the DAQ-system hardware.</i>	24

2.1	<i>Lepton mass distribution of the K_{13}^- sample tagged by $K_{\mu 2}^+$ events.</i>	31
2.2	<i>Fit of $V_{us}f_+(0)$ using KLOE measurement of BRs and of K_L lifetime and a quadratic parametrization of the form factors.</i>	33
2.3	<i>View of the $V_{us} - V_{ud}$ plane. The bound from measurement and the unitarity line are shown.</i>	34
2.4	<i>KL fit and of NS fit.</i>	36
2.5	<i>Dalitz plot for data clearly shows the presence of S_γ (top band) and $\omega\pi$ processes (bottom-left band).</i>	38
2.6	<i>Cross section for $e^+e^- \rightarrow \pi^+\pi^-$.</i>	41
3.1	<i>Definitions of the variables used in the s-t relations classification.</i>	56
3.2	<i>Logic scheme of the KLOE offline reconstruction.</i>	60
4.1	<i>Scheme of the production mechanism of the η meson and decay chain into the $3\pi^0$ final state.</i>	62
4.2	<i>The invariant mass of three pions system. The distribution before (red line) and after (blue line) a kinematic fit with no mass constraints are superimposed.</i>	67
4.3	<i>χ^2 distribution. Top: linear scale; Bottom: logarithmic scale.</i>	68
4.4	<i>MonteCarlo photon energy spectrum.</i>	69
4.5	<i>Energy resolution for photons. The straight lines represents the result of fit with the function: $\frac{\sigma_E}{E} = P_0 \left(1 - e^{-\frac{P_1}{E}} + \frac{P_2}{E} + \frac{P_3}{\sqrt{E}} \right)$.</i>	70
4.6	<i>ζ distribution after the selection procedure.</i>	71
4.7	<i>χ_0^2 shapes for events with right (straight line) and wrong (dotted line) photon pairing.</i>	72
4.8	<i>Distribution of the difference between the best and secon best combination $\Delta\chi^2$, for events with right (straight line) and wrong (dotted line) photon pairing.</i>	72
4.9	<i>From top left in clockwise direction: reconstructed z variable for Low, Medium I, Medium II, High purity samples.</i>	74
5.1	<i>Dalitz plot for pure phase space $\eta \rightarrow 3\pi^0$ decay. Left: in variables of kinetic energies of decay product (where T_{π_i} and $\langle T_\pi \rangle$ are kinetic energy of each pion i and mean kinetic energy of three π^0, respectively, in the η rest frame). Right: the distribution $z = \frac{f^2}{\rho_{max}^2}$.</i>	76
5.2	<i>Left: z distribution after selection and reconstruction. Right: the resolution on z. From top to bottom: Low, Medium I, Medium II, High purity samples.</i>	77
5.3	<i>From top left in clockwise direction: the resolution of the z variable after the second kinematic fit for Low, Medium I, Medium II, High purity samples.</i>	78

5.4	<i>From top left in clockwise direction: the efficiency as function of z variable for Low, Medium I, Medium II, High purity samples.</i>	79
5.5	<i>Results of the fit to the Dalitz plot on MonteCarlo for different values of α in input. From top to bottom: the results in the ranges $(0 - 1)$, $(0 - 0.8)$, $(0 - 0.7)$ and $(0 - 0.6)$. Left: Low purity sample. Right: Medium I purity sample.</i>	83
5.6	<i>Results of the fit to the Dalitz plot on MonteCarlo for different values of α in input. From top to bottom: the results in the ranges $(0 - 1)$, $(0 - 0.8)$, $(0 - 0.7)$ and $(0 - 0.6)$. Left: MediumII purity sample. Right: High purity sample.</i>	84
5.7	<i>From top left in clockwise direction: the z distribution on data for Low, Medium I, Medium II, High purity samples.</i>	85
5.8	<i>Data MonteCarlo comparison of the Dalitz plot density distribution for the $\eta \rightarrow 3\pi^0$ decay. The effect on the phase due to the different value of the η mass has been overdrawn.</i>	87
5.9	<i>Distribution of $Z_{\text{data}}/Z_{\text{MC}}$ (left) and $Z'_{\text{data}}/Z_{\text{MC}}$ (right).</i>	88
5.10	<i>Data–MonteCarlo ratio of the z distribution obtained using on data. Left: $M_\eta = 547.30$ MeV; right: $M_\eta = 547.822$ MeV; the linear fit is superimposed. Note that p_1 equals to two times the slope parameter α.</i>	89
5.11	<i>Data–MonteCarlo comparison on invariant mass of π^0. From top to bottom: Low purity, Medium purity I, Medium purity II, High purity samples. Left: linear scale. Right: log scale.</i>	90
5.12	<i>Photons energy spectrum data (dots) are compared to MonteCarlo (solid). Top: linear scale. Center: log scale. Bottom: bin by bin normalized data–MonteCarlo discrepancy.</i>	91
5.13	<i>Comparison data vs MonteCarlo for the distribution of $E_{\pi^0} - \frac{M_\eta}{3}$ in the bin $z = 0$. From top to bottom: Low purity, Medium purity I, Medium purity II, High purity samples. Left: linear scale. Right: log scale.</i>	93
5.14	<i>From top to bottom: Low purity, Medium purity I, Medium purity II, High purity samples. Left: distribution of the RMS in bins of E_{π^0}. Right: data MonteCarlo discrepancy in the RMS distribution.</i>	94
5.15	<i>Ratio between weighed and not weighed efficiencies as function of z. The errors take into account the correlations between the efficiencies. From top left in clockwise direction: for Low, Medium I, Medium II, High purity samples.</i>	96
5.16	<i>Background composition. From top to bottom: Low purity, Medium purity I, Medium purity II, High purity samples. Left: linear scale. Right: log scale.</i>	99

- 5.17 *Comparison between data and fitted function. Blue points are data and the histogram is the function.* 101

List of Tables

1.1	<i>DAΦNE Parameter list.</i>	5
1.2	<i>Cross sections for several e^+e^- interaction processes at $\sqrt{s} = 1.02$ GeV. For the process $e^+e^- \rightarrow \phi$, the visible cross section is listed.</i>	25
2.1	<i>ϕ meson decays and their Branching Ratio [2].</i>	27
2.2	<i>The KL-NS fit results: Interval of maximal variations for the f_0 parameters resulting from the systematic uncertainties studies done on both fits.</i>	37
2.3	<i>The KL-NS fit results: Interval of maximal variations for the f_0 parameters resulting from the systematic uncertainties studies done on both fits.</i>	37
2.4	<i>Theoretical results for the slope parameter of the various approximations.</i>	51
2.5	<i>Experimental results for the slope parameter in the neutral decay. We have added in quadrature the statistical and systematic errors quoted in [41].</i>	51
4.1	<i>Number of prompt clusters and ECL filter efficiency for totally neutral radiative decays.</i>	63
5.1	<i>Results of fit to Dalitz plot for different purity samples. For each sample, the slope parameter α has been evaluated in the fit range $(0, 1)$ and $(0, 0.7)$.</i>	86
5.2	<i>Fitted results for the slope parameter α. The results refer to a value of η mass on data: $M_\eta = 547.822$ MeV.</i>	88
5.3	<i>Fitted results for the slope parameter α taking into account the data MonteCarlo discrepancy on resolution.</i>	92
5.4	<i>Fitted results for the slope α taking into account the data MonteCarlo discrepancy in combinatorial background evaluation.</i>	98
5.5	<i>Fitted results for the slope parameter α: where $M_{\eta_I} = (547.822 + 0.069)$ MeV, and $M_{\eta_{II}} = (547.822 - 0.069)$ MeV.</i>	98

5.6	<i>Summary table of systematic uncertainties. The total systematic uncertainty is obtained as square root of the sum of the square of each term.</i>	100
-----	--	-----

The thesis is divided into five chapters.

The first chapter is devoted to a short description of the DAΦNE collider and the KLOE detector. The performance of the electromagnetic calorimeter and of the drift chamber are listed. A description of the trigger system and of the data acquisition system are then given.

In the second chapter, an overview of the results obtained from the analysis of 2001 ÷ 2002 KLOE data is presented. A brief discussion of the theoretical aspects of the eta decay into three pions final states is given with a particular emphasis to the $\eta \rightarrow 3\pi^0$ decay. In the final part of the chapter, a description of the Dalitz plot of $\eta \rightarrow 3\pi^0$ is given, as well as a brief discussion of the theoretical and experimental results.

The third chapter is dedicated to describe the reconstruction package for neutral and charged particles and the basic ideas for the event classification implemented at KLOE.

The fourth and fifth chapters give a detailed description of the data analysis, performed using $\mathcal{L}_{int} = 418 \text{ pb}^{-1}$ of e^+e^- collisions collected in the 2001 ÷ 2002 data taking. In the fourth, in some detail, the selection procedure of $\phi \rightarrow \eta\gamma \rightarrow \pi^0\pi^0\pi^0\gamma \rightarrow 7\gamma$ including a short description of the kinematic fit, aiming to ensure a kinematic closure of the event, is first discussed. The rest of the chapter is entirely devoted to a description of the photon pairing algorithm.

In the fifth chapter, the algorithm is used to construct the Dalitz plot variable. After discussing the resolution and efficiency, determined through MonteCarlo studies, the slope parameter α is extracted from a fit to the theoretically predicted functional form of the distribution.

Finally a complete study of the systematic effects on the fitted parameter value is provided.

Result of this analysis is then presented.

Chapter 1

The KLOE experiment at DAΦNE

The KLOE experiment has been recording e^+e^- collisions at DAΦNE, the ϕ -factory at Laboratori Nazionali in Frascati, since April 1999. In March 2006, it was successfully concluded. In this chapter the DAΦNE collider and the KLOE detector are presented. Also an overview of the MonteCarlo simulation of the experiment is given.

1.1 The collider DAΦNE

DAΦNE (Double Anular ϕ -factory for Nice Experiments) [1] is an electron-positron collider, designed to work at the center of mass energy $\sqrt{s} \simeq 1020$ MeV, corresponding to the resonance peak of the vector meson ϕ , with mass $M_\phi = (1019.460 \pm 0.019)$ MeV [2], see Figure 1.1.

Electron and positron beams are stored in two separate rings, to reduce beam-beam effects. The two rings intersect in two collision points, IP, with an horizontal half crossing angle of ± 12.5 mrad, which results in a small momentum component (~ 13 MeV in the horizontal plane) of the ϕ mesons produced. At one the KLOE detector is located, while the other is alternatively occupied by two experiments: DEAR and FINUDA to study atomic and nuclear physics. The DAΦNE design accepts a maximum number of 120 bunches corresponding to a bunch crossing period of 2.7 ns. The finite crossing angle results in a small average ϕ momentum of about 13 MeV along the transverse x -axis. The main parameters of the collider corresponding to

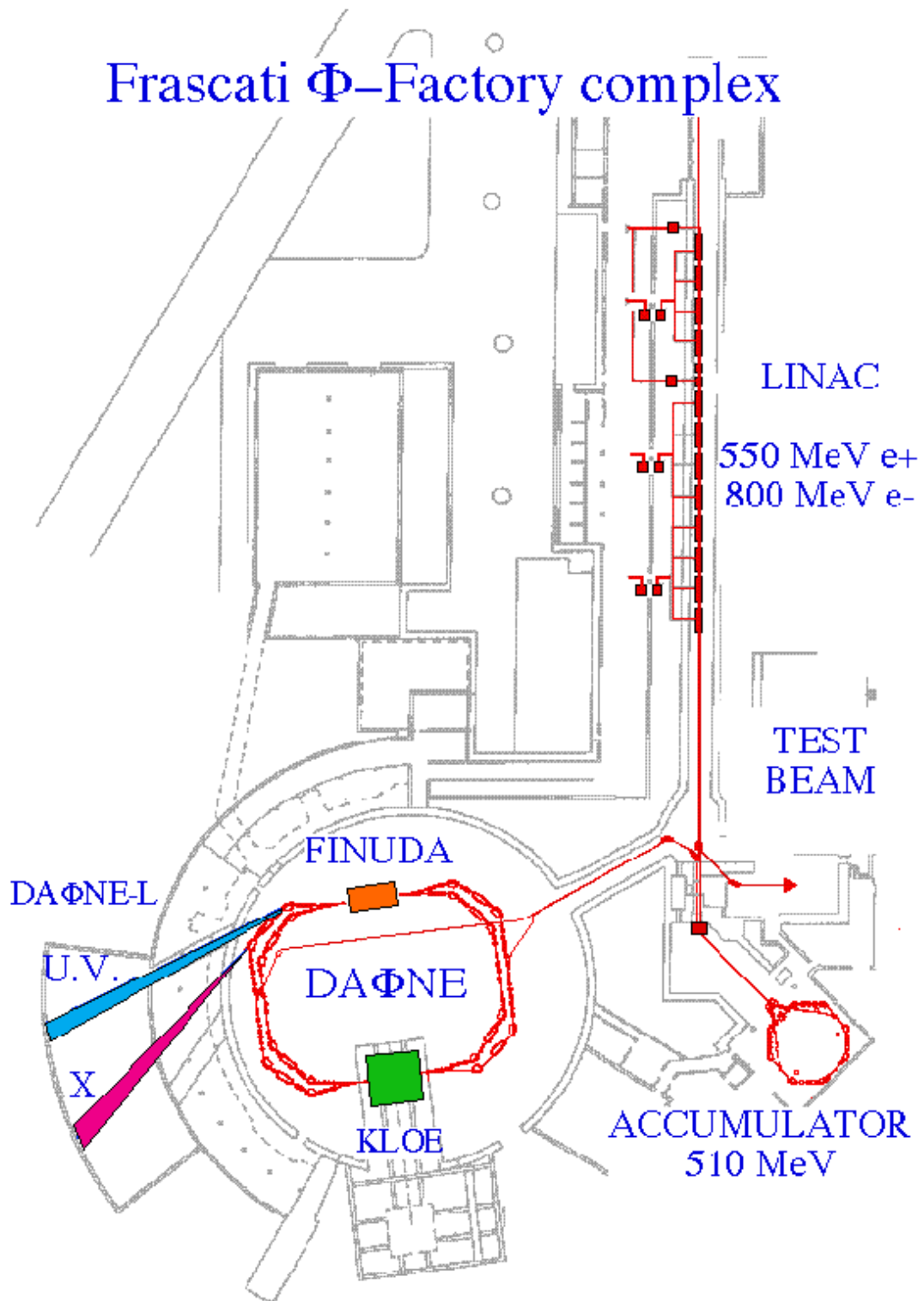


Figure 1.1: Scheme of the DAΦNE collider apparatus.

the last KLOE run are listed in Table 1.1.

Energy	0.51 GeV
Trajectory length	97.69 m
RF frequency	368.26 MHz
Harmonic number	120
Damping time, τ_E/τ_x	17.8/36.0 ms
Beam current e^-e^+	2/1.4 Amps
Number of colliding bunches	111
Beta functions β_x/β_y	1.7/0.017 m
Emittance, ε_x (KLOE)	0.34 mm mrad
Coupling at 0 current	0.3 %
Tunes ν_x/ν_y	0.091/0.166 e^- 0.109/0.191 e^+

Table 1.1: DAΦNE Parameter list.

1.2 The DAΦNE luminosity at KLOE

First collisions in the KLOE interaction region after the KLOE installation were detected on April 14, 1999. During the first data taking (1999 ÷ 2000), a total integrated luminosity of $\simeq 2.4 \text{ pb}^{-1}$ has been collected, with instantaneous luminosity peak between 3 and $5 \cdot 10^{30} \text{ cm}^{-2} \text{ s}^{-1}$. This value lower than the one expected ($5 \cdot 10^{32} \text{ cm}^{-2} \text{ s}^{-1}$) has been improved with some changes:

- the magnetic field of KLOE has been reduced from 6 to 5.6 kGauss,
- the KLOE interaction region has been modified in the optics and supports,
- colliding current has been increased due to the vacuum conditioning and the continuous improvements of the feedback system.

In the 2004 ÷ 2006 KLOE run, DAΦNE has delivered an integrated luminosity in excess of 2 fb^{-1} on energy 1019.4 MeV see Figure 1.2 and, in the last part of the run $> 0.25 \text{ fb}^{-1}$ off peak 1000 MeV.

A high statistic scan of the ϕ resonance has been also performed collecting

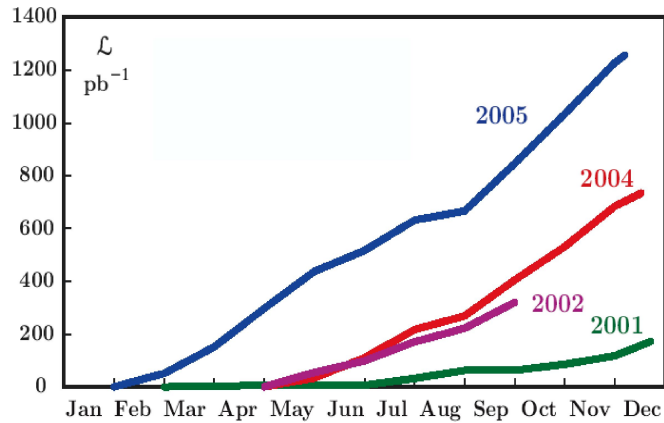


Figure 1.2: *Integrated luminosity in pb^{-1} as function of the number of days of data taking for the years 2001 ÷ 2005.*

more than 10 pb^{-1} per point at 4 different energies (1010, 1018, 1023, and 1030 MeV).

As shown in Figure 1.3 the machine performance have been continuously improving during the on-energy run. The highest peak and daily integrated

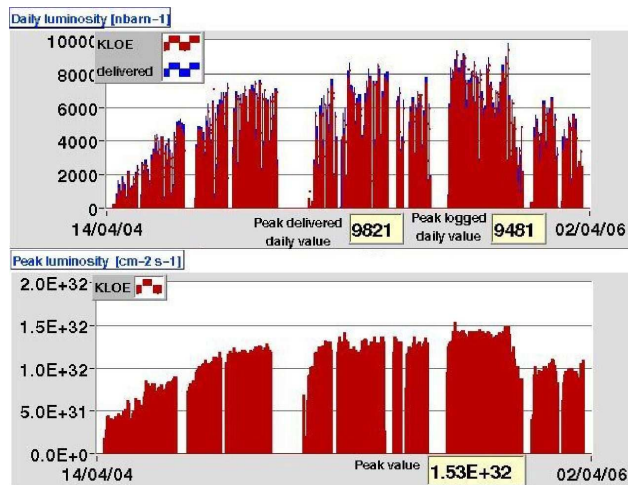


Figure 1.3: *Last KLOE run peak and integrated luminosity.*

luminosities measured by KLOE have been $L_{peak} = 1.53 \cdot 10^{32} \text{ cm}^{-2} \text{ s}^{-1}$ and $L_{day} = 10 \text{ pb}^{-1}$, respectively.

1.3 The KLOE detector

The KLOE detector consist of a superconducting coil able to furnish a magnetic field up to 6 kGauss, whose iron return is designed to keep the field as much as possible uniform and parallel to the beam axis; a drift chamber, to track the charged particles; an electromagnetic calorimeter, to detect neutral particles; two more tile calorimeters surrounding the quadrupoles, to complete the calorimetric hermeticity. A section of the KLOE detector is shown in Figure 1.4.

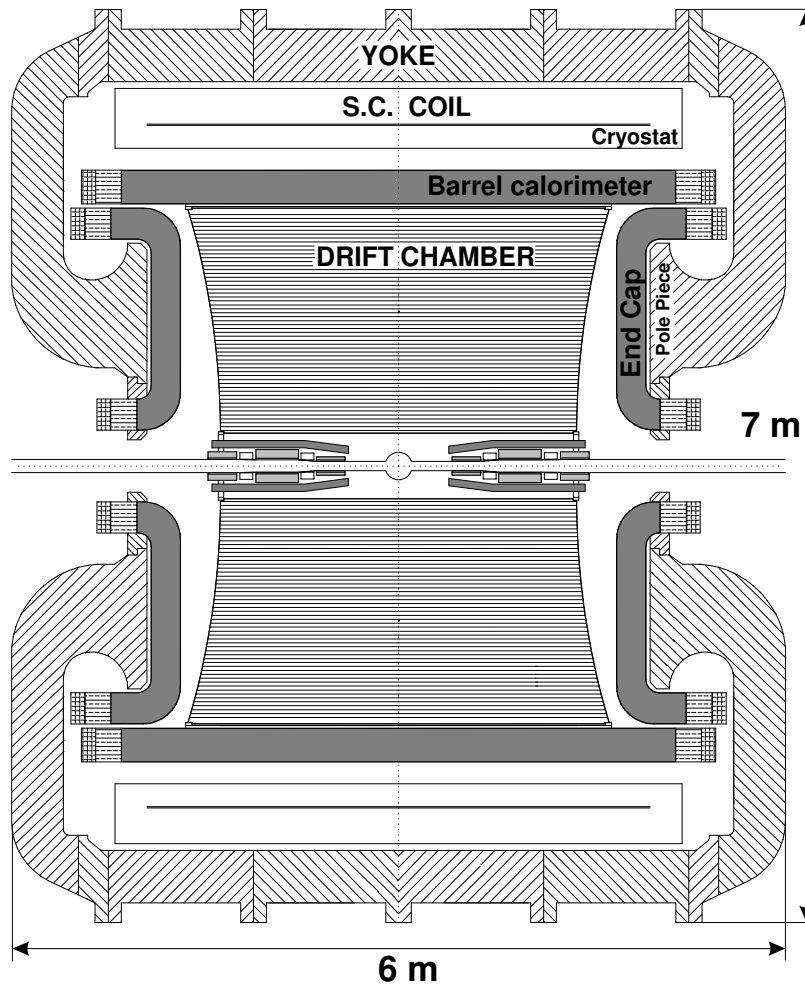


Figure 1.4: Section of the KLOE detector.

In the following we will refer to an axes system where the z -axis lies along

the beams and the x and y -axes are the standard ones, x horizontal and y vertical.

1.3.1 The beam-pipe

The interaction region consists of a sphere (see Figure 1.5) of 10 cm radius, corresponding to $\sim 17K_S$ decay length in order to avoid regeneration.

The wall of the beam-pipe is made of AlBeMet, an alloy of beryl-aluminum 60%–40% with thickness 0.5 mm. A small layer of beryl, thick 0.05 mm guarantees continuity to the pipe inside the sphere. Beryl has been chosen because of its low atomic number in order to reduce multiple scattering, regeneration, energy loss of particles and photon conversion.



Figure 1.5: *The beam-pipe.*

1.3.2 The drift chamber

The KLOE tracking detector is a cylindrical drift chamber [3], see Figure 1.6, whose length is variable from 2.8 m near the beam-pipe to 3.3 m near the calorimeter walls; the outer radius is 2 m, the inner radius is 25 cm. The drift chamber has the following properties:

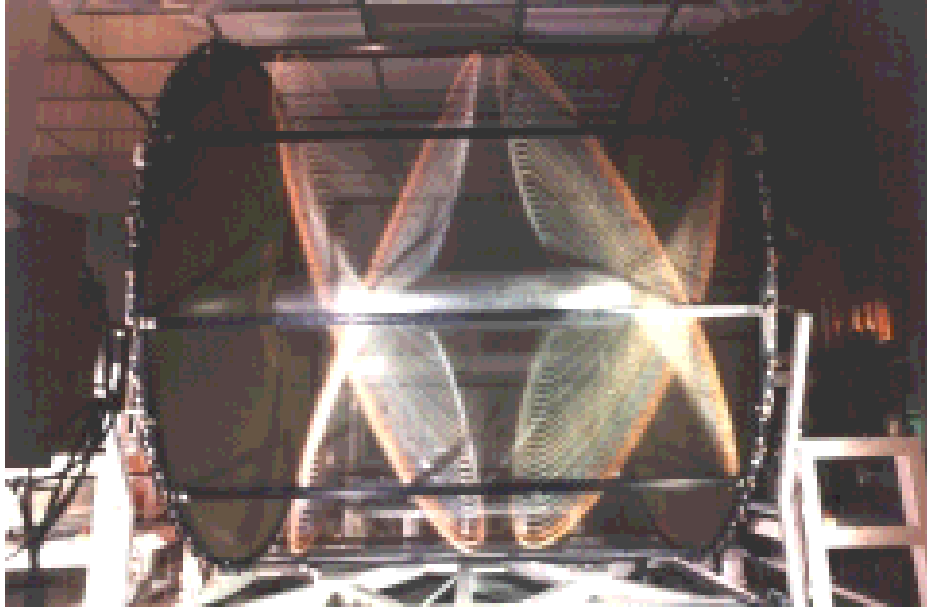


Figure 1.6: *The KLOE drift chamber at the end of the wire stringing.*

- high and uniform reconstruction efficiency over a large volume, in order to reconstruct correctly particles that decay inside its sensitive volume (such as K_L);
- very good momentum resolution ($\Delta p_\perp/p_\perp$) for low momentum tracks ($50 < p < 300$ MeV). In this energy range the dominant contribution to the momentum resolution is multiple scattering:

$$\frac{\Delta p_\perp}{p_\perp} = \frac{0.053}{|B|L\beta} \sqrt{\frac{L}{X_0}}$$

where p_\perp is the transverse momentum in GeV, β is the velocity of the particle, L is the total track length in m, B is the magnetic field in T and X_0 is the radiation length;

- it is transparent to low energy photons (down to 20 MeV);
- track resolution in the transverse plane $\sigma_{R\phi} \simeq 200 \mu\text{m}$ and a vertex resolution $\sigma_{vtx} \simeq 1$ mm.

The chamber has a uniform cell structure. The uniform filling of the chamber has been achieved through a structure of drift cells “almost” square

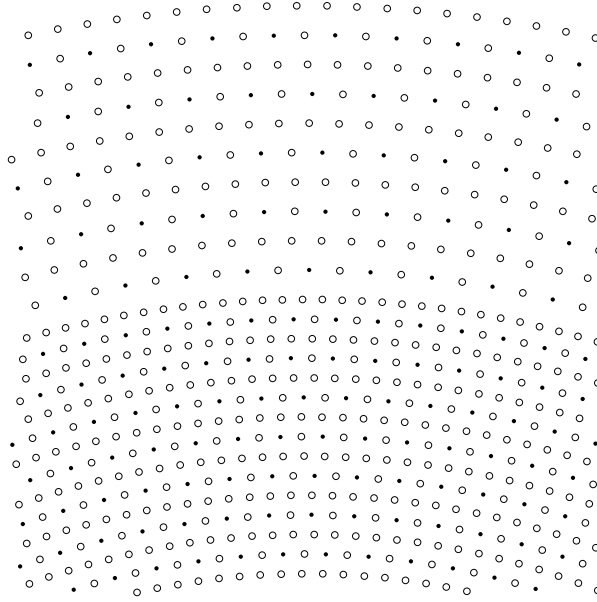


Figure 1.7: *Drift cells configuration at $z = 0$; a portion of chamber at boundary between small cells (inner layers) and big cells (outer layers) is shown. Full dots indicate sense wires, circles indicate field wires.*

shaped (see Figure 1.7), arranged in coaxial layers with alternating stereo angles which increases in magnitude with radius from ± 60 to ± 150 mrad.

The stereo angle is defined as the angle between the wire and a line parallel to the z -axis passing through the point on the plate of the DC, where the wire is connected, see Figure 1.8. The ratio of field to sense wires (3:1) is a satisfactory compromise in maximizing the track sampling frequency, while maintaining the electrostatic stability of the drift cell. The sense wires are made of gold-plated tungsten and their diameter is $25 \mu\text{m}$. The field wires are made of silver-plated aluminum and their diameter is $80 \mu\text{m}$; to the field wires are applied ~ 1900 V. There are 12 inner and 46 outer layers, the corresponding cell areas are 2×2 and $3 \times 3 \text{ cm}^2$, respectively, for a total of 12582 single-sense-wire cells and 52140 wires.

Materials were chosen in order to minimize the density along the path of neutral kaons, charged particles and photons. A carbon fiber composite ($\leq 0.1X_0$) has been chosen for the chamber shell.

The gas used is a 90% helium, 10% isobutane mixture. The helium is the active component of the mixture and thanks to its low atomic mass reduces the effect of multiple scattering and regeneration. The isobutane acts like quencher, it absorbs UV photons produced in recombination processes in or-

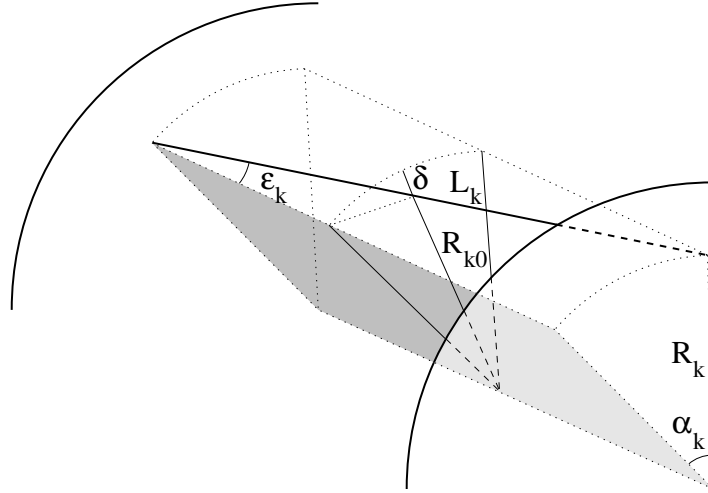


Figure 1.8: *KLOE drift chamber geometry: the z -axis is defined along the beam direction. The stereo angle ε_k is defined in such a way that the stereo drop δ is constant.*

der to avoid the production of discharges in the DC, it can't be more than 10% due to its flammability. The mixture has a radiation length $X_0 \simeq 1300$ m, while taking into account also the presence of the wires, the average radiation length in the whole chamber volume is about $X_0 \simeq 900$ m.

The cell efficiency is determined using cosmic ray tracks with more than 96 hits. The “hardware efficiency” is defined as the ratio of the number of hits found in a cell to the number of tracks crossing the cell. This efficiency is $\simeq 99.6\%$ both for small and big cells and it is constant over the whole drift chamber volume. The “software efficiency” is defined requiring the hit found in the cell to be used by the track fit and it is $\simeq 97\%$. The “software” and “hardware” efficiencies are shown in Figure 1.9. As can be seen, the software efficiency is lower for small drift distances, this is due to the worse resolution close to the wires due to non-linearity of space to time (s-t) relations.

Using samples of Bhabha-scattering events, the momentum resolution for 510 MeV e^\pm has been evaluated. It can be seen in Figure 1.10 that for $50^\circ < \theta < 130^\circ$ (θ being the angle between the z -axis and the direction of the particle, polar angle of emission) the momentum resolution are $\sigma_p \simeq 1.3$ MeV and $\sigma_p/p = 2.5 \times 10^{-3}$.

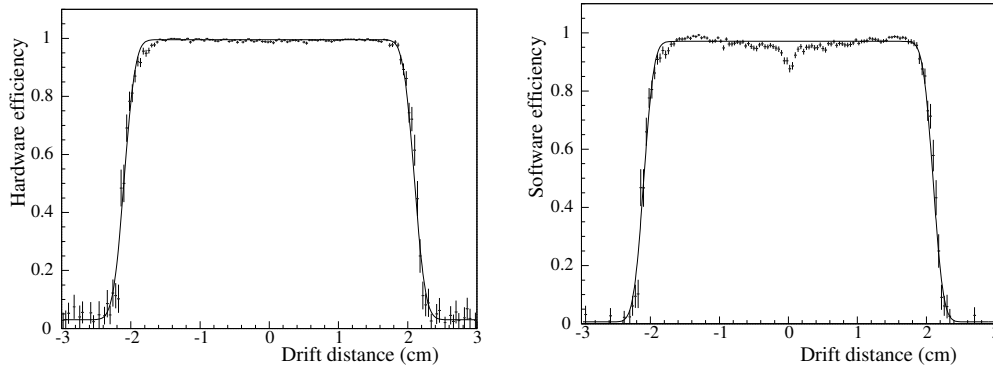


Figure 1.9: Example of hardware and software efficiency for a small cell.

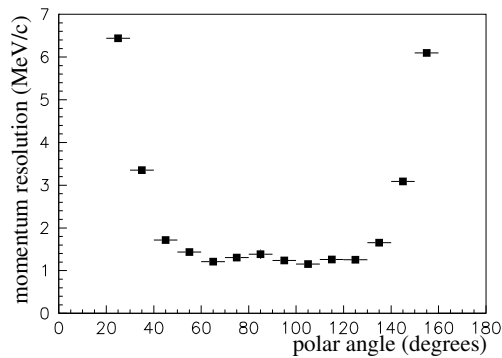


Figure 1.10: Momentum resolution as function of polar angle, using Bhabha events.

1.3.3 The electromagnetic calorimeter

The KLOE EMC [4], is a fine-sampling lead scintillating-fiber calorimeter with photomultiplier read out Figure 1.11. The calorimeter has the following properties:

- a very good time resolution ($\simeq 100$ ps) and a good determination ($\simeq 1$ cm) of the photon conversion point, in order to allow the K^0 neutral decay vertex determination with an accuracy of few mm. The good position resolution together with the large radius ($\simeq 2$ m) consent to have a very good resolution on the angle of the photon conversion point;

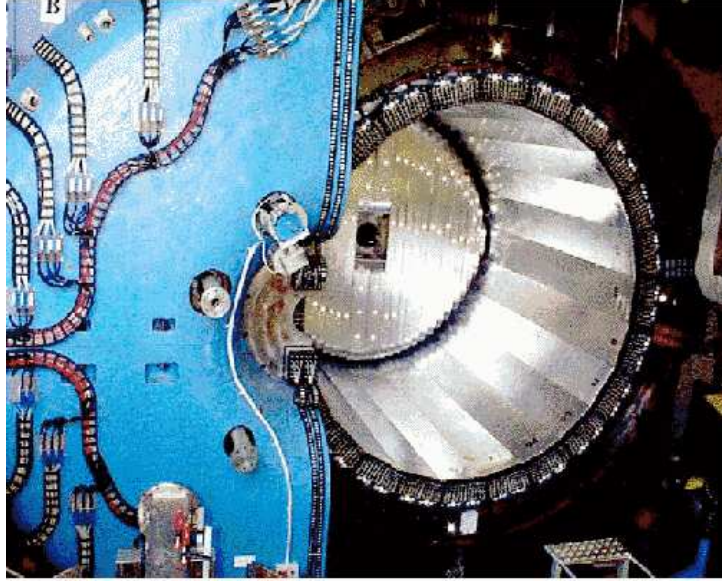


Figure 1.11: *The KLOE calorimeter.*

- an high hermeticity (98% of the solid angle), thanks to which multi-photon process has an acceptable geometrical efficiency and events with different number of photons can be separated correctly.
The energy resolution is good ($5.7\%/\sqrt{E[\text{GeV}]}$) and the calorimeter is fully efficient over the range $20 \div 300$ MeV;
- it has also a very fast time response, that is used to trigger events at first stage.

A lead-scintillating fiber sampling calorimeter has been designed to fulfill these requirements. Scintillating fibers offer several advantages, in particular they provide good light transmission over the required distances, up to ~ 4.3 m. Superior timing accuracy is obtained because of single mode propagation. The calorimeter shape is adapted to the geometrical requirements obtaining good hermeticity. The cylindrical barrel consists of 24 modules of trapezoidal shape 4.3 m long, 23 cm thick and ~ 60 cm wide. Each endcap consists of 32 vertical modules $0.7 \div 3.9$ m long and 23 cm thick. The modular scheme of calorimeter can be seen in Figure 1.12.

The barrel covers a region between 40° and 310° , the endcaps covers the angles included between 9° and 46° and between 134° and 171° respectively. The cross-section of the modules is rectangular, of variable width. Modules are bent at the upper and lower ends to allow insertion into the

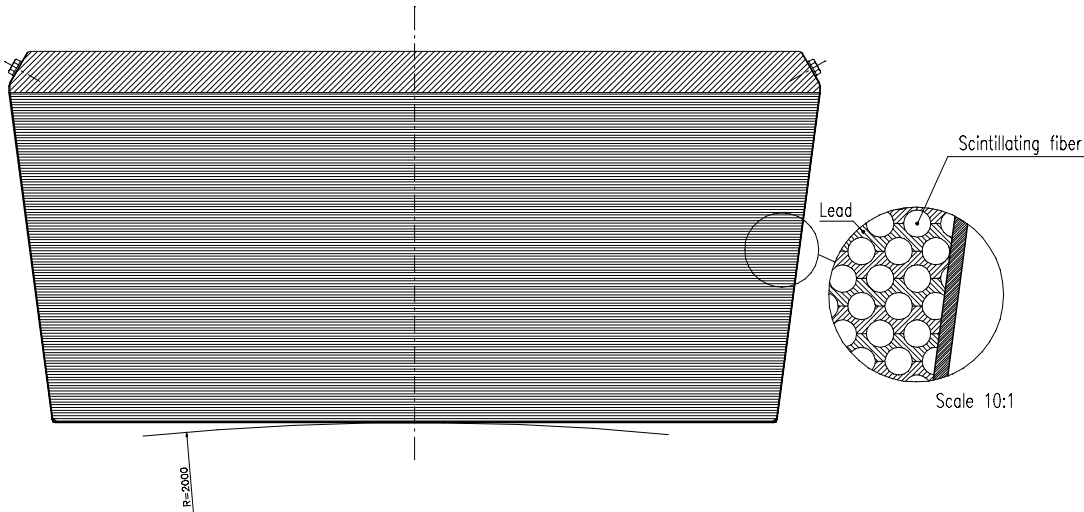


Figure 1.12: *Schematic view of the fiber-lead composite of each module of the electromagnetic calorimeter.*

barrel calorimeter and also to maintain the photo-tube axes parallel to the magnetic field. Due to the large overlap of barrel and endcaps, the KLOE calorimeter has no inactive gap at the interface between those components. The central endcap modules are vertically divided into two halves to allow the passage of the beam-pipe.

All modules are made of 200 grooved, 0.55 mm thick lead foils alternating with 200 layers of scintillating fibers with diameter 1 mm, glued in the grooves with a special epoxy, which is not harmful to the fiber plastic. Fibers are mostly orthogonal to the entering particles in order to avoid channeling. The ratio by volume of the different component material is: lead: fiber: epoxy = 42:48:10, the high scintillator content is necessary to maximize the number of collected photons per MeV released by the impinging particle, so to optimize the energy and time resolutions. The attenuation length of the fibers is $\lambda \geq 3$ m, while the average density is 5 g/cm^3 , the radiation length is ~ 1.5 cm and the overall thickness of the calorimeter is ~ 15 radiation length.

Light is collected on both sides of each module, via light pipes which match almost square portions of the module end faces to 4880 photo-tubes. The read-out splits the calorimeter into five planes in depth, each deep 4.4 cm with the exception of the last which is 5.2 cm deep. In the transverse direction each plane is subdivided into cells 4.4 cm wide. The set made of 5 cells lined up, one for each transverse plane is named “column”.

The read-out $r - \phi (x - z)$ granularity for the EMC is finally $\sim 4.4 \times 4.4 \text{ cm}^2$ slightly varying in size across the modules. This allows a very good spatial resolution.

The energy deposit in each cell is obtained from the charge measured at each side of the modules by the ADC's. The cell time is derived by time intervals measured at each side of the modules by the TDC's. The difference of the signal arrival times at both ends allows to reconstruct the coordinate along the fibers. Therefore the resolution on the z longitudinal coordinate depends on the statistics of photoelectrons: $\sigma_z \sim 9 \text{ mm}/\sqrt{E[\text{GeV}]}$.

The energy resolution and the linearity of the energy response have been measured using photons from radiative Bhabha events and from $\phi \rightarrow \pi^+\pi^-\pi^0$ events. In both cases the photon energy E_γ is estimated by tracks momenta (reconstructed by the drift chamber) and it is compared with the measured cluster energy E_{CL} . The fractional resolution σ_E/E_γ and the relative deviation from linearity $(E_\gamma - E_{CL})/E_\gamma$, obtained from radiative Bhabha events are plotted in Figure 1.13 as function of the photon energy. Linearity is

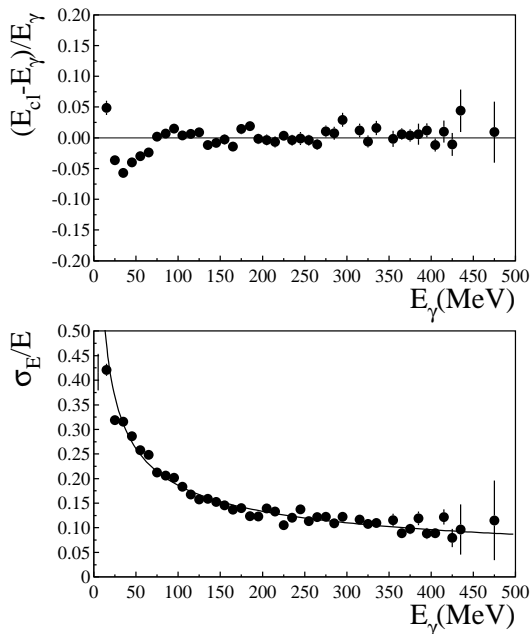


Figure 1.13: (Top) Linearity of the calorimeter energy response as a function of the photon energy; (Bottom) energy resolution of the calorimeter as a function of the photon energy. The two curves are evaluated with radiative Bhabha events.

better than 1% for $E_\gamma > 75 \text{ MeV}$, while deviations from linearity at the

$4 \div 5\%$ level are observed for low energies, probably due to the loss of shower fragments. The fit of the energy resolution to the function $a/\sqrt{E[\text{GeV}]} + b$ gives a negligible constant term, proving that the resolution is dominated by sampling fluctuations, and gives a stochastic term $a = 5.7\%$:

$$\frac{\sigma_E}{E} = \frac{5.7\%}{\sqrt{E(\text{GeV})}} \quad (1.1)$$

Compatible results are obtained from $\phi \rightarrow \pi^+\pi^-\pi^0$.

The time resolution derived by the analysis of various radiative ϕ decays is shown in Figure 1.14.

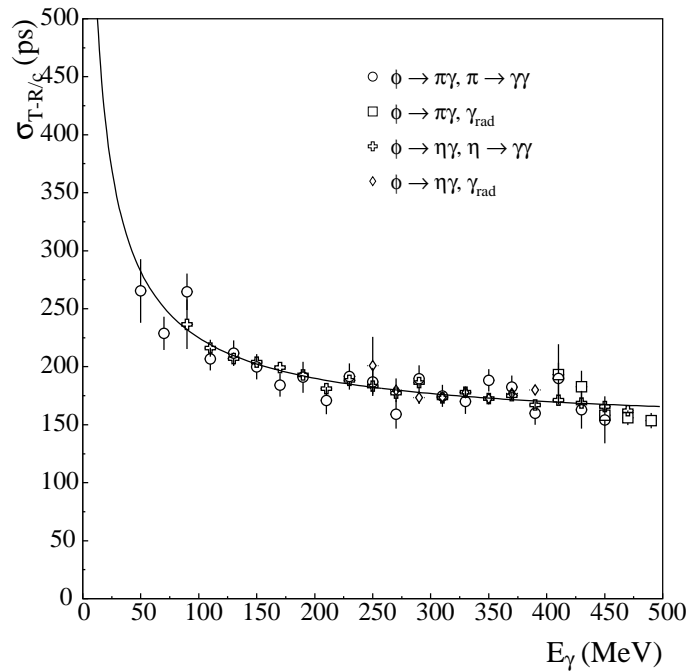


Figure 1.14: Time resolution of the calorimeter as a function of the photon energy, for radiative ϕ decays.

Good agreement between the measurements for different channels is observed down to 100 MeV. The curve in the plot is the result of a fit:

$$\sigma_t = \frac{54 \text{ ps}}{\sqrt{E[\text{GeV}]}} \oplus 140 \text{ ps} \quad (1.2)$$

where the sampling fluctuation term is in agreement with test beam data [5] and the second term is a constant to be added in quadrature. The constant term is given by the quadrature sum of two contributions: the intrinsic time spread due to the finite length of the luminous point in the beam direction, which contributes for ~ 125 ps, and the resolution of the synchronization with the DAΦNE radio-frequency, which contribute for ~ 50 ps. Compatible results are obtained from $\phi \rightarrow \pi^+\pi^-\pi^0$ and from radiative Bhabha decays.

The photon detection efficiency is an important quantity for various analysis. Three data samples have been used to estimate it: radiative Bhabha events and $\phi \rightarrow \pi^+\pi^-\pi^0$ decays, which provide a source of photons coming from the interaction point, and $K_L \rightarrow \pi^+\pi^-\pi^0$ decays, in which the photons originate from a K_L decay vertex in the DC volume. The detection efficiency ε_γ , resulting from these three analysis, are shown as a function of the photon energy in Figure 1.15.

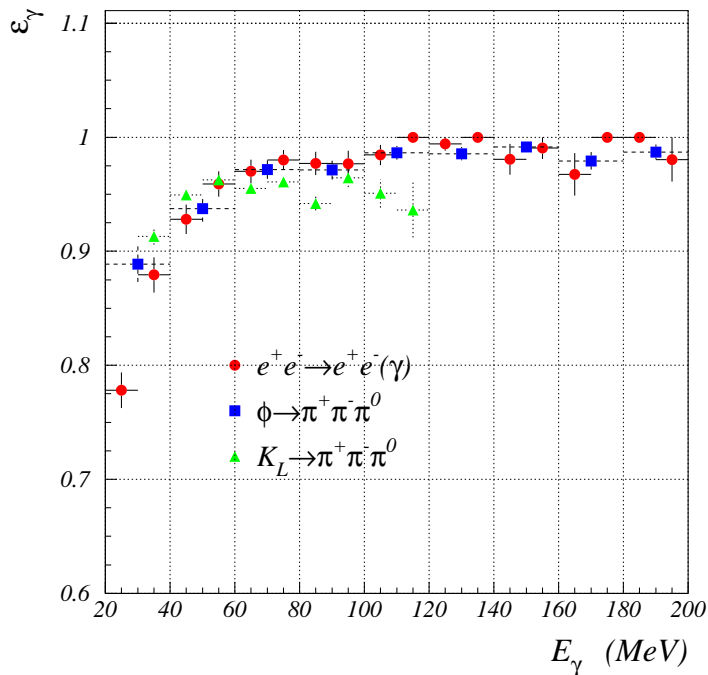


Figure 1.15: Photon detection efficiency using: $e^+e^-\gamma$ (Bhabha radiative), $\phi \rightarrow \pi^+\pi^-\pi^0$, $K_L \rightarrow \pi^+\pi^-\pi^0$.

A constant value of more than 98% is observed above 100 MeV, while a loss in efficiency is evident below 100 MeV.

1.3.4 The quadrupole calorimeters (QCAL)

In order to achieve the maximum possible luminosity, the last focusing quadrupoles are very close to the interaction point, inside the KLOE detector. The presence of this quadrupoles limits the geometrical acceptance for photons coming from K_L^0 decays increasing by a factor 5 the probability to lose one single photon, then a sensitive detector covering the quadrupoles is certainly welcome.

Detector design must satisfy stringent weight and volume requirements to fit between the quadrupoles and the drift chamber inner wall. The adopted solution is a sampling calorimeter made of lead and scintillator tiles see Figure 1.16.

The calorimeter is divided in 16 radial section whose light is collected by wavelength shifting fibers. Each fiber curved and shared between two non adjacent sector allowing to place the PMs only on the side far from the interaction point and avoiding double hits on the same fiber.

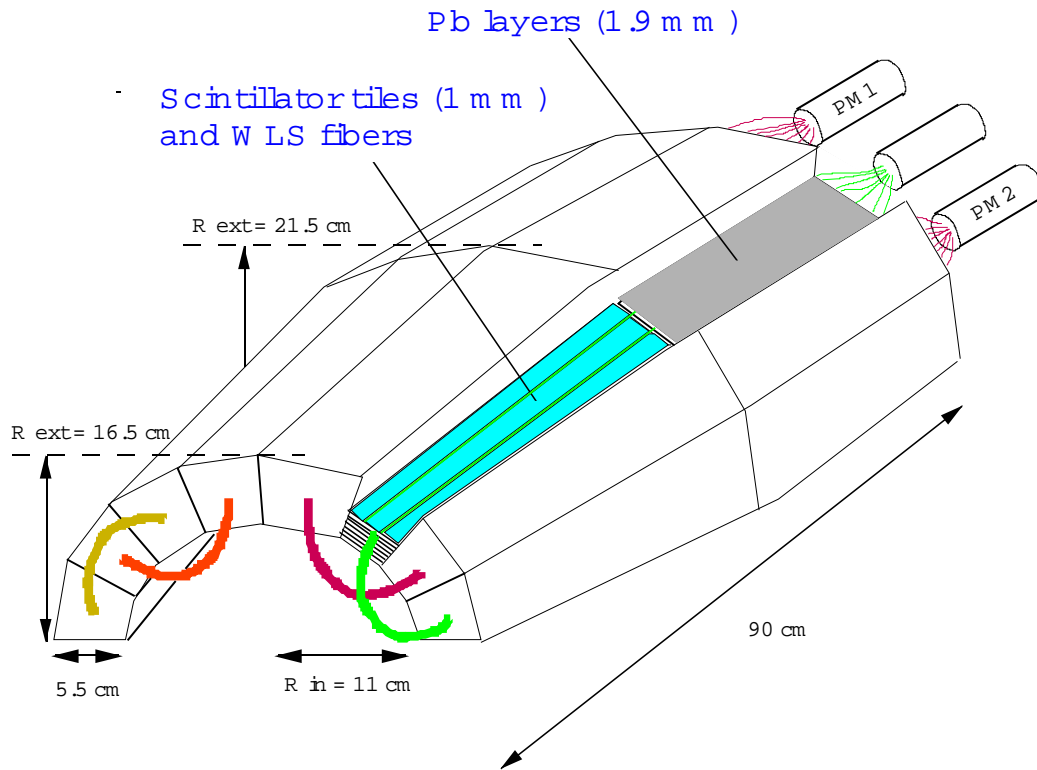
Looking from the interaction point each radial sector has a conical part (50 cm long) followed by a cylindrical one (31 cm long). Each sector contains 16 lead planes (2 mm thick) and 15 scintillator layers (1 mm thick) for a total of ~ 5.5 radiation lengths. PMs are of mesh-dynode type to reduce the effect of magnetic field.¹ The signal coming out from each PMs is splitted in two: the first is shaped and sent to the ADC, the second is discriminated and sent to the TDC. Main request for the QCAL detector is the photon detection efficiency. This can be measured using cosmic rays selected by the drift chamber. The energy released by a cosmic MIP is equivalent to that of a 75 MeV photon.

The efficiency for the single sector is 98 %, but when both signal at the fiber ends are requested the efficiency drop down to 75 %. The hit coordinate along the fiber is determined by the difference in the arrival time at two ends from:

$$z = L - v \frac{t_2 - t_1}{2} \quad (1.3)$$

where L is half of the total fiber length and v is the light speed in the fiber. Photon detection efficiency has been evaluated using $K_L^0 \rightarrow \pi^0 \pi^0 \pi^0$ and

¹Nonetheless a gain reduction of $\sim 60\%$ has been observed once the PMs have been installed inside the KLOE magnetic field.



KLOE - QCAL

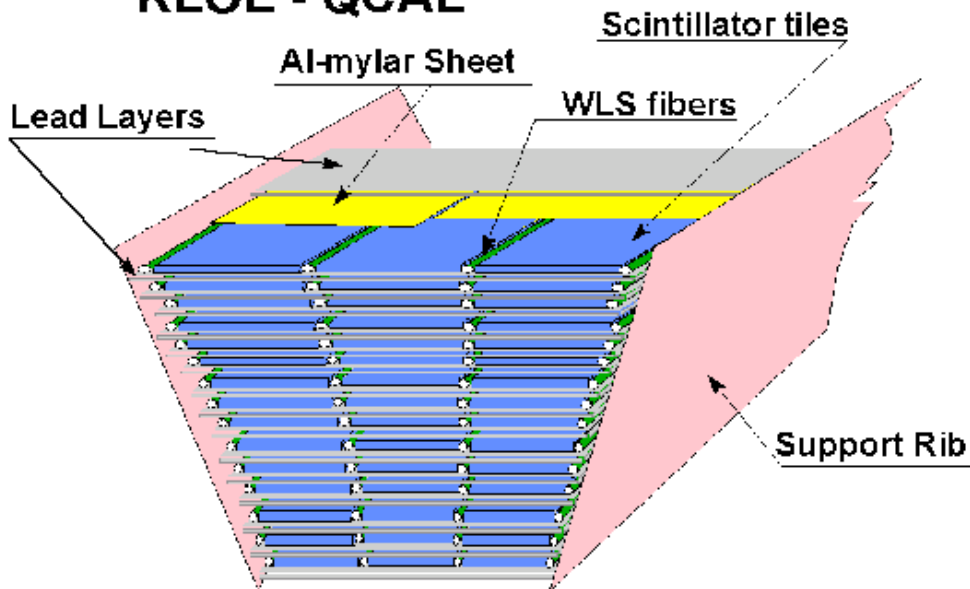


Figure 1.16: Schematic view of a quadrupole calorimeter.

$K_L^0 \rightarrow \pi^+\pi^-\pi^0$ samples and looking for a photon not detected by calorimeter that intersects the QCAL region. The result for a single photon efficiency is $92 \pm 4\%$.

Time resolution obtained with cosmic rays events is:

$$\sigma(t) = 0.9 \pm 0.2 \text{ ns} \quad (1.4)$$

corresponding to:

$$\sigma(t) = \frac{240 \text{ ns}}{\sqrt{E(\text{GeV})}} \quad (1.5)$$

Energy resolution is expected to be larger than 40% and indicates that QCAL detector can be used as photon counter but not a precise calorimeter.

1.4 The trigger system

The main goal of the KLOE trigger system [6] is to:

- produce a trigger signal for all ϕ events;
- recognize Bhabha and cosmic-ray events and accept a downscaled sample for calibration purposes;
- reject the machine background.

There are two main sources of background.

One is due to Bhabha events at small angles, where electrons and positrons hit two focusing quadrupoles located very close to the IP and produce showers inside the detector.

The other source is due to particle losses from the DAΦNE beams. These off-momentum particles come from beam-gas interactions or Touschek scattering. The trigger is based on local energy deposit in calorimeter and multiplicity information from the drift chamber. It is composed by two levels (see Figure 1.17) in order to both produce an early trigger with good timing to start the Front End Electronic (FEE) operations and to use as much information as possible from the drift chamber. Specifically, after the arrival of a first level trigger, additional information is collected from the drift chamber, which is used, together with the calorimetric information, to confirm the former and to start the DAQ system. The calorimeter triggers on local energy deposits larger than a programmable threshold. Two thresholds are given for each EMC signal, the first at low energy ~ 50 MeV in order to

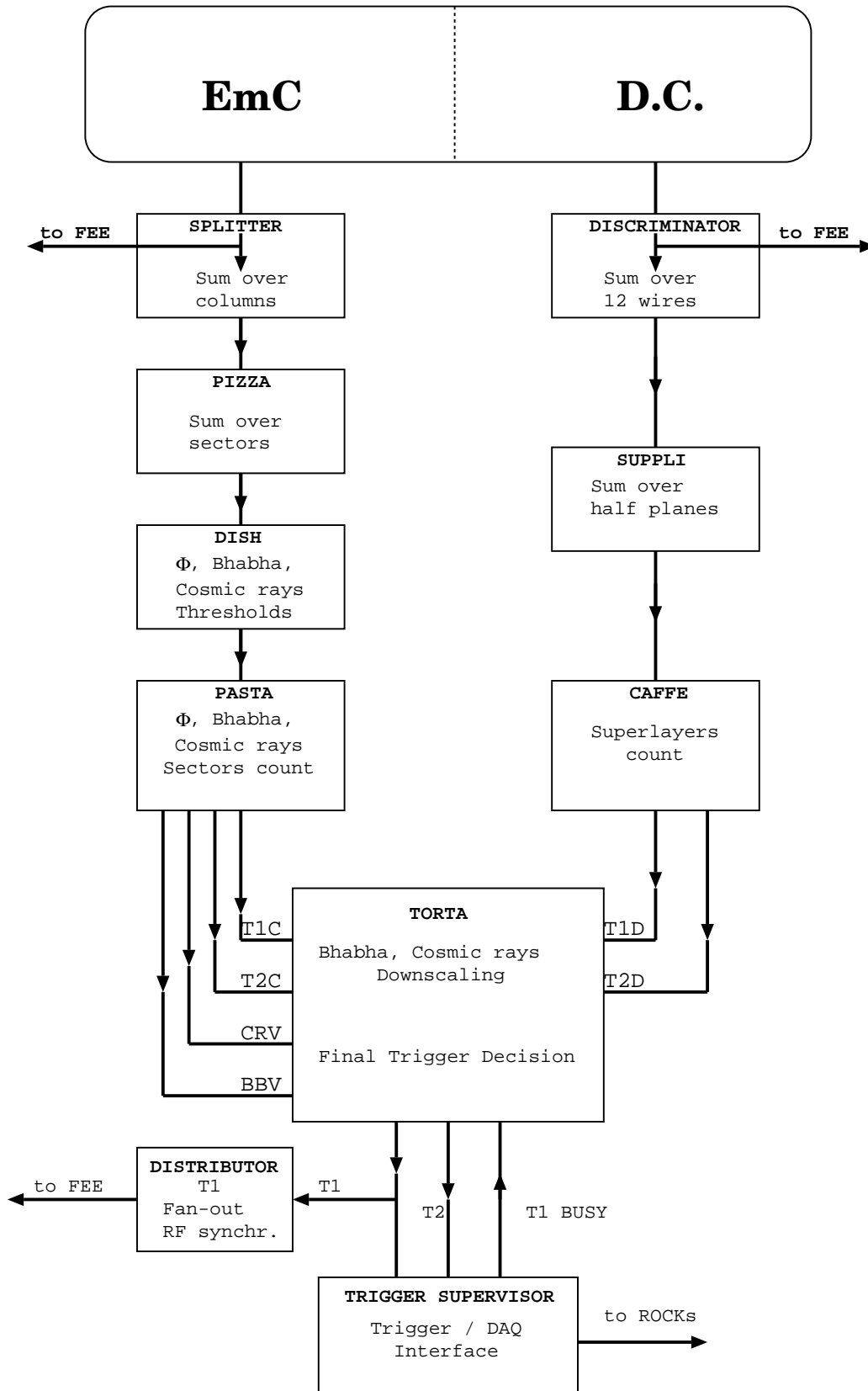


Figure 1.17: Trigger scheme.

trigger on low energy particles from ϕ decays entering the calorimeter (Low Energy Threshold, LET), and the second at high energy ~ 350 MeV in order to identify and reject (or accept as downscaled sample) Bhabha events (BhaBha Trigger, BBT).

The drift chamber triggers on the multiplicity of fired wires: each sense wire signal, after preamplification, is fed into the discriminator card where signals for the TDCs and the trigger are formed; for the trigger they are formed to a width of 250 ns, i.e. the coincidence width which optimizes both signal efficiency and background rejection, and produces a fast trigger signal.

The **first level** trigger algorithm can be summarized as follows:

- ϕ trigger: (2 calorimeter LET hits with Barrel-Barrel, Barrel-Endcap or Endcap-Endcap topology) OR (15 drift chamber hits within 250 ns).
- *Bhabha veto*: 2 calorimeter BBT sectors with Barrel-Barrel or Endcap-Endcap topology.

The level one trigger T1 sets a $2 \mu\text{s}$ long acknowledge signal, which vetoes other first level triggers and allows signals formation from the drift chamber cells.

Before being distributed to the calorimeter FEE, the first level trigger is synchronized with a resolution of 50 ps with the DAΦNE radiofrequency divided by 4 ($T = 10.8$ ns). Therefore the calorimeter TDCs measure the time with respect to a bunch crossing coming n periods after the collision that originated the event, where n has to be determined by the offline reconstruction of the event. This technique allows us to preserve the resolution on time measurement at the level of pico-second, which would be otherwise spoiled by the intrinsic jitter of the trigger signal formation.

At the end of the dead time the trigger system asks for a confirmation of the level 1 decision. The signal from these dedicated channels are treated in the same way as those used to define the ϕ or Bhabha calorimetric triggers but with threshold chosen to be equal to the average energy released in a cell by a minimum ionizing particle MIP ($40 \div 50$ MeV). Once two sectors are above threshold, the cosmic rays bit is activated and the event flagged. To avoid rejection of $\mu^+\mu^-$ events, which trigger easily the external planes of the calorimeter, a third level trigger (T3) has been developed. Each event detected as cosmic ray events by the second level trigger are flagged and not rejected, then these events pass through the T3 filter before being written on tape. The T3 filter performs a fast preliminary pattern recognition looking for tracks coming from the interaction point. If no track is coming from the IP the event is rejected. The level two trigger T2 gives the stop to chamber

TDCs and starts the data acquisition.

The **second level** algorithm can be summarized in this way:

- *ϕ trigger*: (at least 1 calorimeter hit in the Barrel or 3 hit in the same Endcap) OR (40 drift chamber hits integrated during 850 ns after T1).
- *Cosmic flag*: 2 hits on the external plane of the calorimeter with Barrel-Barrel or Barrel-Endcap topology.

1.5 The data acquisition system

The KLOE data acquisition system [7] (DAQ) was designed to collect data from more than 23000 electronic channels (13000 DC and 10000 EmC channels) at a maximum rate of 50 Mbytes/s. A two level concentration scheme has been adopted, Figure 1.18.

In the first level *sub-events* are processed, where a sub-event is a piece of an event produced by a subset of the front end electronics (FEE). The FEE are housed in crates together with read-out controllers (ROCK's). The crates are organized in 10 chains.

A ROCK manager, the ROCKM, reads sub-events, associated to a trigger number, from a chain through a custom bus, the *C-bus*. The ROCKM's are housed in second level crates together with CPU's equipped with FDDI interfaces. The CPU's reads the data from the ROCKM's and send it to the CPU online farms. The addresses of the online farm processors is provided by a Data Flow Controller (DFC). The DFC guarantees that all sub-events with the same trigger number are sent to the same CPU online farm. After arriving the online farm processor, the sub-events from different chains, associated to the same trigger number, are merged together to build a whole event, and are written in YBOS format into a circular buffer. Here the formatted events are read by the two processes: the *Recorder*, which writes events to disk, and on tapes; the *Spy-Daemon*, which writes events in a spy buffer for online monitoring, events in a spy buffer for online monitoring, event display, and detector calibration.

These tasks are accomplished by numerous processes. Among these, the *Trgmon* process, reading information about trigger sectors, provides a fast monitor of quantities such as instantaneous luminosity, background level, and data rates. The *L3* process selects Bhabha, $\gamma\gamma$, and CR events used for

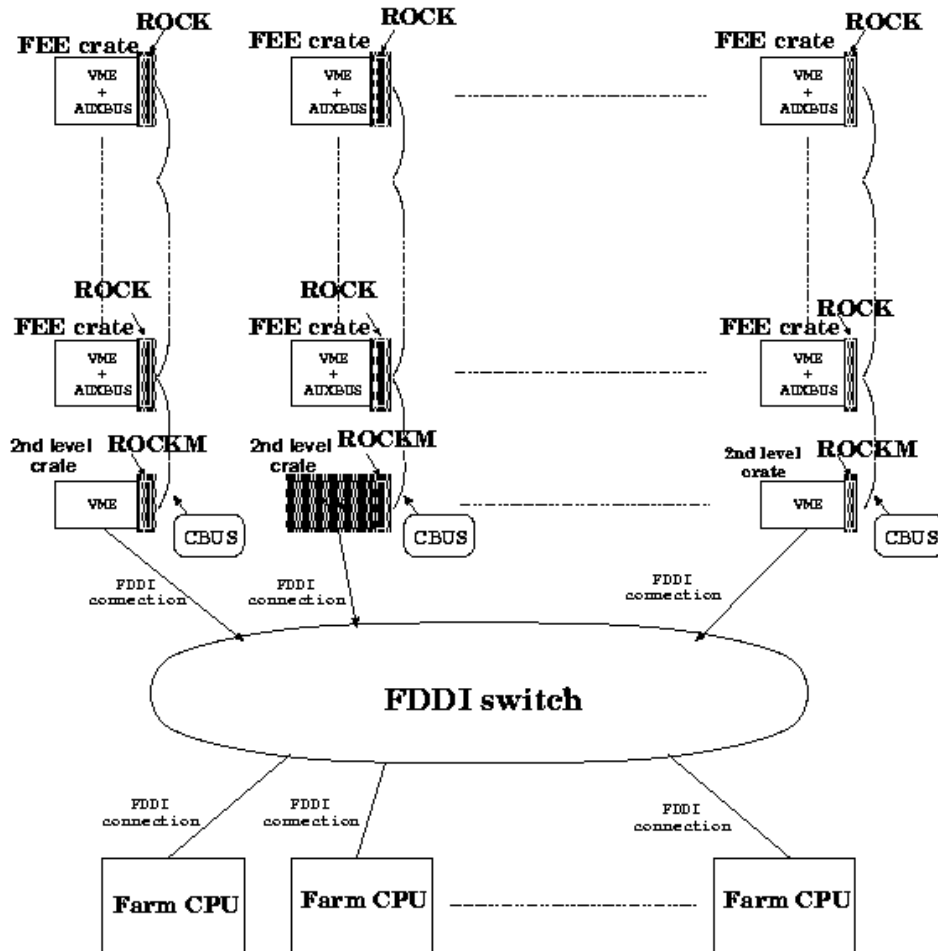


Figure 1.18: Scheme of the DAQ-system hardware.

detector online calibration and monitoring. Finally, the *Trkmon* process, calculates for each run the average ϕ momentum and position by using Bhabha events, and checks drift chamber wire efficiencies.

1.6 MonteCarlo: detector simulation and physics generators

The KLOE MonteCarlo program, GEANFI, is based on the GEANT 3.21 library [8] widely used in current high-energy and astroparticle physics experiments. GEANFI incorporates a detailed description of the KLOE apparatus, including:

- the new interaction region: the beam pipe, the low-beta quadrupoles, and the QCAL calorimeters;
- the drift chamber;
- the endcap and barrel calorimeters;
- the superconducting magnet and the return yoke structure

A set of specialized routines has been developed to simulate the response of each detector, starting from the basic quantities obtained from the GEANT particle-tracking and energy deposition routines. Moreover the simulation of $\frac{dE}{dX}$ measurement in drift chamber and the treatment of nuclear interactions/regeneration in drift chamber wall and beam pipe are inserted.

GEANFI contains the code to generate the physics of interest at DAΦNE. The cross section for the relevant processes in e^+e^- collisions at $\sqrt{s} = 1.02$ GeV are listed in Table 1.2.

A precise Bhabha-event is required for the measurement of the luminosity. To reach an accuracy of a few per mill for the effective cross-section radiative corrections must be properly treated. BABAYAGA [10] generator [8, 9] has been interfaced with GEANFI. This generator is based on the application to

Process	Polar Angle	$\sigma(\mu)$ b
$e^+e^- \rightarrow e^+e^-(\gamma)$	$20^\circ < \theta < 160^\circ$	6.2
$e^+e^- \rightarrow \mu^+\mu^-(\gamma)$	$20^\circ < \theta < 160^\circ$	0.085
$e^+e^- \rightarrow \pi^+\pi^-(\gamma)$	$20^\circ < \theta < 160^\circ$	0.080
$e^+e^- \rightarrow \gamma\gamma(\gamma)$	$20^\circ < \theta < 160^\circ$	0.30
$e^+e^- \rightarrow \omega\pi^0$		0.008
$e^+e^- \rightarrow \phi$		3.1

Table 1.2: Cross sections for several e^+e^- interaction processes at $\sqrt{s} = 1.02$ GeV. For the process $e^+e^- \rightarrow \phi$, the visible cross section is listed.

QED of the parton-shower method originally developed for perturbative QCD

calculations. The generator takes into account corrections due to initial-state radiation (ISR), final-state radiation (FSR), and ISR-FSR interference, and has an estimated accuracy of 0.5%. BABAYAGA can also be used to generate $e^+e^- \rightarrow \mu^+\mu^-$ and $e^+e^- \rightarrow \pi^+\pi^-$ events.

The routines in the GEANT library simulate two and three body decays according to pure phase-space distributions. Only the main decay modes of muons, pions, kaons, and mesons are simulated. We have enriched the list of simulated particle-decay modes to include rare decays and refined the kinematic distributions of the secondaries to include the correlations expected from the matrix elements for the different decay processes.

The generator for ϕ events, BABAYAGA, selects the ϕ decay channel and declares the decay products to GEANT. Initial-state radiation and the beam-energy spread of the machine ($\Delta E_{beam}/E_{beam} = 0.05\%$) are taken into account event by event in the simulation of the decay kinematics.

All decays modes of the η and η' mesons are simulated.

Chapter 2

Physics at KLOE and η in $3\pi^0$ decay

Most of the ϕ mesons decay are in charged kaons or neutral kaons, so that kaon physics is the largest part of KLOE program. Other particles, produced in ϕ decays with enough abundance to improve the existing experimental measurements, are ρ , η , η' , a_0 and f_0 .

In Table 2.1 the ϕ meson decays and their Branching Ratio are reported. Furthermore, thanks to the radiative return that reduce the center of mass

Canale	<i>BR</i>
K^+K^-	$49.2 \pm 0.6 \%$
$K_S^0K_L^0$	$34.0 \pm 0.5 \%$
$\rho\pi + \pi^+\pi^-\pi^0$	$15.3 \pm 0.4 \%$
$\eta\gamma$	$1.301 \pm 0.024 \%$
$\pi^0\gamma$	$(1.25 \pm 0.07) \times 10^{-3}$
e^+e^-	$(2.97 \pm 0.04) \times 10^{-4}$
$\mu^+\mu^-$	$(2.86 \pm 0.19) \times 10^{-4}$
ηe^+e^-	$(1.15 \pm 0.10) \times 10^{-4}$
$\pi^+\pi^-$	$(7.3 \pm 1.3) \times 10^{-5}$

Table 2.1: ϕ meson decays and their Branching Ratio [2].

energy of the colliding beams, KLOE can measure the hadronic cross-section $e^+e^- \rightarrow \pi^+\pi^-$, in the crucial region from $\pi\pi$ threshold to the ϕ resonance.

An overview of the results obtained from the analysis of 2001 ÷ 2002 data ($\sim 500 \text{ pb}^{-1}$) is presented in the first part of this chapter.

The $\eta \rightarrow 3\pi^0$ decay within the chiral perturbation theory framework is the

subject of the second part of this chapter.

2.1 Kaon physics

Kaons are produced at a ϕ -factory in a pure antisymmetric initial state with quantum numbers $J^{PC} = 1^{--}$. At DAΦNE the ϕ mesons are produced practically at rest, with only a small momentum (~ 13 MeV/c) in the plane of the orbit, so that the kaons are produced practically back to back.

Infact the peculiar characteristic of KLOE is the tagging technique.

The tagging allow us to select clean kaon beams of K^\pm or of $K_{S,L}$ and to measure absolute Branching Ratios. In particular, a K_S beam is tagged using events with a K_L interaction in the calorimeter; K_L mesons are tagged detecting $K_S \rightarrow \pi^+\pi^-$ decays. Charged kaons are tagged using two body decays, $K^\pm \rightarrow \mu^\pm\nu$ and $K^\pm \rightarrow \pi^\pm\pi^0$.

Perfect tagging requires that the detection efficiency of the tagging mode be independent of the decay mode of the tagged kaon. In reality, some dependency of the tagging efficiency on the decay mode of the signal kaon exists. This dependence must be carefully measured using MonteCarlo and data control samples for each BR measurement.

2.1.1 Semileptonic K_L decays and the K_L lifetime

KLOE has measured the dominant K_L Branching Ratios using the K_L beam tagged by $K_S \rightarrow \pi^+\pi^-$ decays [11]. About 13×10^6 tagged K_L decays are used for the measurement, and $\sim 4 \times 10^6$ to evaluate efficiencies.

For K_{e3} , $K_{\mu3}$, and $\pi^+\pi^-\pi^0$ decays we compute smallest of the two values of $\Delta = E_{miss} - p_{miss}$ assuming each charged particle to be pion and muon (muon and pion). The distribution in this variable shows two well separated peaks corresponding to the three modes mentioned. Fitting the distribution with MonteCarlo obtained shapes for each mode, gives the number of events in each channel.

To select $K_L \rightarrow 3\pi^0$ events, at least three photons are required from the K_L decay vertex. The reconstruction efficiency and purity of the selected sample are both about 99%.

The resulting Branching Ratios are:

$$BR(K_L \rightarrow \pi e \nu(\gamma)) = 0.4007 \pm 0.0006 \pm 0.0014_{Tag+Trk} \quad (2.1)$$

$$BR(K_L \rightarrow \pi \mu \nu(\gamma)) = 0.2698 \pm 0.0006 \pm 0.0014_{Tag+Trk} \quad (2.2)$$

$$BR(K_L \rightarrow 3\pi^0) = 0.1997 \pm 0.0005 \pm 0.0019_{Tag+\gamma count} \quad (2.3)$$

$$BR(K_L \rightarrow \pi^+ \pi^- \pi^0(\gamma)) = 0.1263 \pm 0.0005 \pm 0.0011_{Tag+Trk} \quad (2.4)$$

after imposing the constraint $\sum BR(K_L) = 1$.

This corresponds to also measuring the lifetime by counting the number of decays in a time interval for a beam of known intensity.

The K_L lifetime has been also measured directly [12], employing 10^7 $K_L \rightarrow 3\pi^0$ events. The result is:

$$\tau_L = (50.97 \pm 0.17 \pm 0.25) \text{ ns}, \quad (2.5)$$

which together with that from the K_L Branching Ratio measurements gives the KLOE average:

$$\tau_L = (50.84 \pm 0.23) \text{ ns}. \quad (2.6)$$

2.1.2 Measurement of the absolute Branching Ratio

$$K^+ \rightarrow \mu^+ \nu_\mu(\gamma)$$

The measurement has been performed using 175 pb^{-1} of data collected in 2002 [13]. The data sample has been split in two uncorrelated subsamples, 60 pb^{-1} have been used for the BR measurement, the remaining 115 pb^{-1} have been used to evaluate the efficiencies and the background.

The $K^- \rightarrow \mu^- \nu_\mu$ tag has been required in order to minimize the effect of the nuclear interactions on the signal side.

The signal is given by a K^+ , moving outwards in the DC with momentum $70 < p_K < 130 \text{ MeV}/c$ and having point of closest approach with $0 < \sqrt{x_{PCA}^2 + y_{PCA}^2} < 10 \text{ cm}$ and $|z_{PCA}| < 20 \text{ cm}$. The kaon decay in the DC fiducial volume ($40 < \sqrt{x_V^2 + y_V^2} < 150 \text{ cm}$) is required. The number of $K^+ \rightarrow \mu^+ \nu_\mu(\gamma)$ decays is obtained counting the events with $225 < p^* < 400 \text{ MeV}/c$. The background is given by $K^+ \rightarrow \pi^+ \pi^0$ and $K^+ \rightarrow \pi^0 l^+ \nu_l$.

The number of signal events we found is $N_{K^+ \rightarrow \mu^+ \nu_\mu(\gamma)} = 865, 283$. The efficiency has been evaluated on a control sample of pure $K \mu \nu$ events selected using only calorimeter information: $\varepsilon = 0.3153 \pm 0.0002$.

Many possible sources of systematic effects have been taken into account;

the most important being related to trigger, energy cuts and fiducial volume acceptances. The Branching Ratio has been obtained from:

$$BR(K^+ \rightarrow \mu^+ \nu_\mu(\gamma)) = \frac{N_{K^+ \rightarrow \mu^+ \nu_\mu(\gamma)}}{N_{Tag}} \times \frac{1}{\varepsilon} \quad (2.7)$$

and is:

$$BR(K^+ \rightarrow \mu^+ \nu_\mu(\gamma)) = 0.6366 \pm 0.0009_{stat.} \pm 0.0015_{syst.} \quad (2.8)$$

corresponding to a total accuracy of 0.27%.

2.1.3 Measurement of the K^\pm semileptonic decays absolute Branching Ratios

The measurement of the semileptonic Branching Ratios has been performed on 410 pb^{-1} of self-triggering tags collected in 2001 and 2002. The whole sample has been split in four subsamples defined by different decay modes for the tagging kaon: two charged and 2 possible tags ($K_{\mu 2}$ and $K_{\pi 2}$; for the latter the identification of the π^0 is also required). This redundancy allows the study of systematics. The kaon tracks and decay vertexes are defined as in the $K_{\mu 2}$ analysis. Moreover it is required that the secondary track, extrapolated to the calorimeter, points to an energy deposit.

In order to reject the two body decay events with $p^* > 195 \text{ MeV}$ have been discarded; p^* is the momentum of the secondary particle on the signal side, evaluated in the pion mass hypothesis.

The π^0 reconstruction is then required looking for two neutral clusters in the EMC having time of flight consistent with the one expected for photons emitted at the kaon decay vertex. Other sources of background are $K^\pm \rightarrow \pi^\pm \pi^0 \pi^0$ with a π^0 undergoing a Dalitz decay and $K^\pm \rightarrow \pi^\pm \pi^0$ with an early decay $\pi^\pm \rightarrow \mu^\pm \nu$. The former are discarded requiring $E_{miss} - P_{miss} < 90 \text{ MeV}$, the latter using the missing momentum of the secondary track in the pion rest frame $P_{sec}^* < 90 \text{ MeV}$. Then the spectrum of the lepton mass (m_{lept}^2) is obtained from the speed of the lepton computed from the time of flight.

The number of K_{e3} and $K_{\mu 3}$ decays is then obtained by fitting the m_{lept}^2 distribution with the MC distributions for the signals and background sources (Figure 2.1). The Branching Ratios have been evaluated separately for each tag sample. Corrections have been applied in order to account for data-MC differences in tracking and calorimeter clustering.

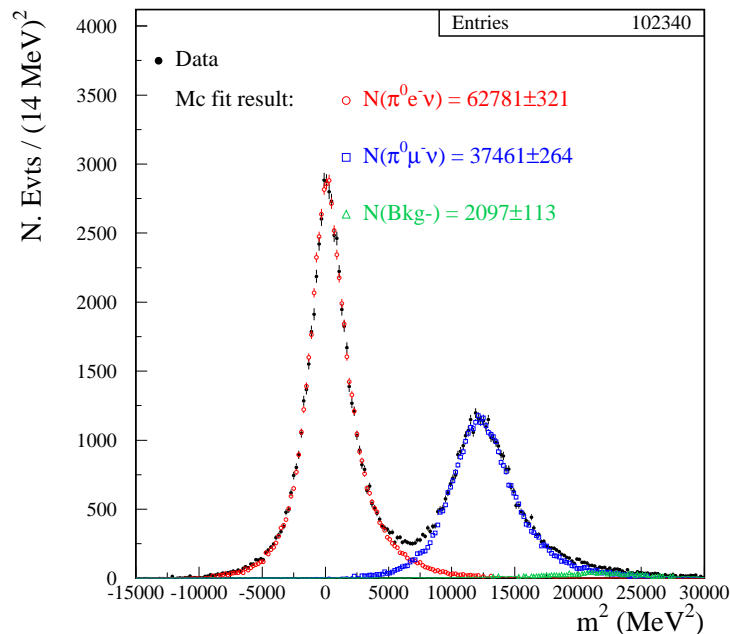


Figure 2.1: *Lepton mass distribution of the K_{l3}^- sample tagged by $K_{\mu 2}^+$ events.*

About 190 000 K_{e3}^\pm and 100 000 $K_{\mu 3}^\pm$ decays have been selected. The preliminary Branching Ratios obtained are:

$$BR(K_{e3}^\pm) = (5.047 \pm 0.046_{Stat+Tag})\% \quad (2.9)$$

$$BR(K_{\mu 3}^\pm) = (3.310 \pm 0.040_{Stat+Tag})\% \quad (2.10)$$

The values are averages over the four different tag samples for each channel. Correlations have been taken into account. The error is dominated by the uncertainty on data/MC efficiency corrections and the systematic error evaluation from the signal selection efficiency still has to be completed.

2.1.4 Measurement of the charged kaon lifetime

The measurement is performed using 230 pb^{-1} . The data sample has been split in two uncorrelated subsamples, 150 pb^{-1} have been used for the measurement, the remaining 80 pb^{-1} have been used to evaluate the efficiencies. Both charges $K_{\mu 2}$ tags have been used.

There are two methods available for the measurement: the kaon decay length

and the kaon decay time. The two methods have allow cross checks and studies of systematics; their resolutions are comparable.

The method relying on the measurement of the charged kaon decay length requires as first the reconstruction of the kaon decay vertex in the fiducial volume (as previously defined) using only DC information. Once the decay vertex has been identified the kaon track is extrapolated backward to the interaction point with 2 mm steps, taking into account the dE/dx to evaluate its velocity βc . Then the proper time can be obtained from the equation:

$$\tau^* = \sum_i \Delta T_i = \sum_i \frac{\sqrt{1 - \beta_i^2}}{\beta_i} \Delta l_i \quad (2.11)$$

The efficiency has been evaluated directly on data. The control sample has been selected using calorimetric information only, looking for a neutral vertex: two clusters in time fired by the photons coming from the π^0 decay. The proper time is fitted between 16 and 30 ns correcting for the efficiency. Resolution effects have been taken into account.

The preliminary result we have obtained for the K^+ is:

$$\tau^+ = (12.377 \pm 0.044 \pm 0.065) \text{ ns} \quad (2.12)$$

with $\chi^2 = 17.7/15$, corresponding to a χ^2 probability $P(\chi^2) = 28.4\%$.

The second method relies on the measurement of the kaon decay time. It requires the backward extrapolation to the interaction point of the tagging kaon track and the forward extrapolation of the helix of the kaon on the signal side. Stepping along the helix we look for the π^0 decay vertex without looking at the real kaon track. For each photon it is possible to measure the proper time

$$\tau^* = (t_\gamma - \frac{r_\gamma}{c} - t_\phi) \cdot \sqrt{1 - \beta_K^2} \quad (2.13)$$

and then, fitting the obtained distribution, the charged kaon lifetime. The work concerning this second method is in progress.

2.1.5 V_{us} extraction

The measurements presented above allow the extraction V_{us} .

The Branching Ratio of the semileptonic decays and the charged kaon lifetime are connected to the value of V_{us} [14]:

$$\frac{BR(K \rightarrow \pi l \nu_l)}{\tau_K} \propto |V_{us} f_+(0)|^2 \quad (2.14)$$

Using as input the KLOE measurements of the semileptonic Branching Ratios for neutral and charged kaons (K_{Le3} , $K_{L\mu3}$, K_{Se3} , K_{e3}^\pm , $K_{\mu3}^\pm$), and of the K_L lifetime and using a quadratic parametrization of the form factors ($\lambda'_+ = 0.02496(80)$, $\lambda''_+ = 0.00162(35)$ and $\lambda_0 = 0.01587(95)$) we have obtained:

$$V_{us} \times f_+(0) = 0.2160 \pm 0.005 \quad (2.15)$$

with $\chi^2/dof = 1.9/4$ (Figure 2.2). The Branching Ratio of the purely lep-

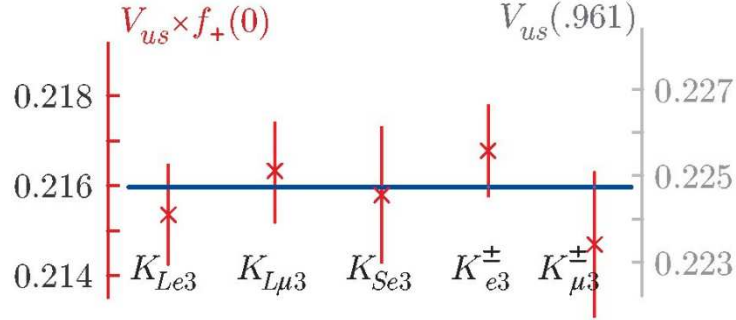


Figure 2.2: Fit of $|V_{us}f_+(0)|$ using KLOE measurement of BRs and of K_L lifetime and a quadratic parametrization of the form factors.

tonic decay, $K_{\mu2}$, can be used, together with the lattice calculation of the ratio f_K/f_π and the V_{ud} value from super-allowed β decay, to evaluate V_{us} as pointed out in [15].

$$\frac{BR(K \rightarrow \mu\nu_\mu(\gamma))}{BR(\pi \rightarrow \mu\nu_\mu(\gamma))} \propto \left| \frac{V_{us}}{V_{ud}} \right|^2 \times \left(\frac{f_K}{f_\pi} \right)^2 \quad (2.16)$$

Taking $f_K/f_\pi = 1.198 \pm 0.003^{+0.016}_{-0.005}$ from [16], we obtain:

$$\left| \frac{V_{us}}{V_{ud}} \right| = 0.2294 \pm 0.0026. \quad (2.17)$$

It is then possible to perform a fit in the $V_{us} - V_{ud}$ plane (Figure 2.3) taking $V_{ud} = 0.97377 \pm 0.00027$ from [17] and the KLOE estimates for V_{us}/V_{ud} from $K_{\mu2}$ and V_{us} from K_{l3} . The results we obtain are:

$$V_{us} = 0.2243 \pm 0.0016 \quad (2.18)$$

$$V_{ud} = 0.97377 \pm 0.00027 \quad (2.19)$$

with $P(\chi^2) = 0.43$.

Assuming also the unitarity:

$$V_{us} = 0.2264 \pm 0.0009 \quad (2.20)$$

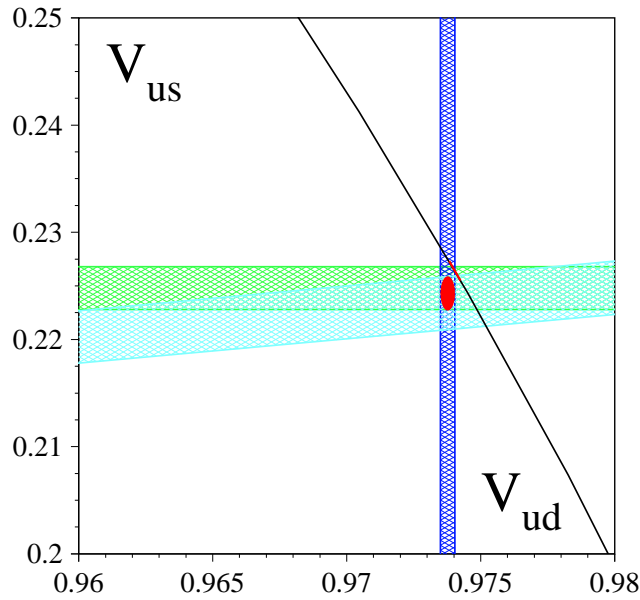


Figure 2.3: View of the $V_{us} - V_{ud}$ plane. The bound from measurement and the unitarity line are shown.

which is in agreement within the errors.

2.2 ϕ -radiative decays

A ϕ -factory can contribute to study both the scalar and pseudoscalar mesons. The lighter mesons $f_0(980)$ and $a_0(980)$ are accessible through the $\phi(1020) \rightarrow S\gamma$ radiative decays, which study can answer to the questions about the structure of that scalar mesons. While the Branching Ratio of the decay $\phi \rightarrow \eta'\gamma$ is particularly interesting since its value can probe the $s\bar{s}$ and gluonium contents of the η' ; and the ratio $BR(\phi \rightarrow \eta'\gamma)/BR(\phi \rightarrow \eta\gamma)$ is related to the $\eta - \eta'$ mixing angle.

2.2.1 $\phi \rightarrow f_0(980)\gamma \rightarrow \pi^+\pi^-\gamma$ and $\phi \rightarrow f_0(980)\gamma \rightarrow \pi^0\pi^0\gamma$

In that works we fit the $\pi^+\pi^-$ invariant mass spectrum to disentangle the contribution from the scalar meson; we use three different approaches in the description of the scalar amplitude:

- **Kaon-loop model (KL)** [18]: the ϕ meson couples to the scalar through a loop of K^+K^- ; the quantity $g_{S\pi\pi}$, g_{SKK} , M_S are free parameters in the fit.
- **No-Structure model (NS)** [19]: a direct coupling of the ϕ to the f_0 is assumed, with a subsequent coupling of the f_0 to the $\pi\pi$ pair. The f_0 amplitude is a Breit-Wigner with a mass dependent width.
- **Scattering-Amplitudes model (SA)** [20]: the amplitude is the sum of the scattering amplitudes $\pi\pi \rightarrow \pi\pi$ and $\pi\pi \rightarrow KK$ with shape fixed by experimental input.

We look for $f_0(980) \rightarrow \pi^+\pi^-$ decays in events $e^+e^- \rightarrow \pi^+\pi^-\gamma$. The main contribution to the decay under study comes from $e^+e^- \rightarrow \pi^+\pi^-\gamma$ events with a photon from initial state (ISR), dominating for small photon polar angle θ_γ or final state (FSR) radiation.

In the low mass region, $400 < m_{\pi^+\pi^-} < 600$ MeV, there is a small contribution from $\phi \rightarrow \rho^\pm\pi^\pm$ with $\rho^\pm \rightarrow \pi^\pm\gamma$ ($\rho\pi$ term); possible contribution from $\phi \rightarrow f_0(600)\gamma$ is considered.

We search for the $f_0(980)$ signal as a deviation from the expected shape. The function to fit the $m_{\pi^+\pi^-}$ spectrum take into account the following term: *ISR+FSR+ $\rho\pi$ +scalar \pm interference(scalar, FSR)+(residual background)*. A sizeable interference term between FSR and f_0 decay is expected in the “ m ” spectrum because of the quantum numbers of the $\pi^+\pi^-$ pair which are the same if it is produced through FSR and f_0 decay ($J^{PC} = 0^{++}$ for FSR and f_0 , $J^{PC} = 1^{--}$ for ISR).

We fit the data in the region $420 < m_{\pi^+\pi^-} < 1010$ MeV using bins 1.2 MeV wide, see Figure 2.4. Concerning the fits KL and NS, the peak around 980 MeV is well interpreted as due to the $\phi \rightarrow f_0(980)\gamma$ contribution, with a destructive interference with FSR; the non-scalar part is well described by the parametrization used, while we are not sensitive to the $\rho\pi$ term.

The f_0 signal appears as an excess of events in the region between 900 and 1000 MeV. In the KL fit the contribution from $f_0(600)$ (or σ) is unnecessary to describe the spectrum. The results of the fits suggest the f_0 to be strongly coupled to kaons and to the ϕ .

In Table 2.2 we show intervals of maximal variations for the f_0 parameters resulting from the systematic uncertainties done on both fits. The SA fit

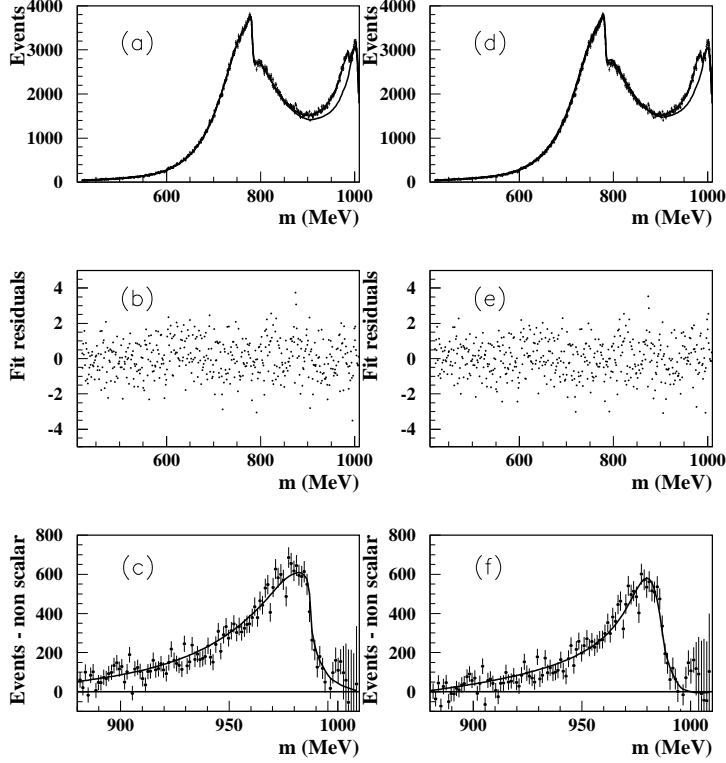


Figure 2.4: *KL fit and of NS fit.*

gives a marginal agreement. In the $\phi \rightarrow f_0(980)\gamma \rightarrow \pi^0\pi^0\gamma$ we extract the light meson parameters with a sample of $L_{int} = 450 \text{ pb}^{-1}$. The high statistics allows us to study the density in the Dalitz plot, $m_{\pi^0\pi^0}$ versus $m_{\pi^0\gamma}$, see Figure 2.5.

The process under study is $e^+e^- \rightarrow \pi^0\pi^0\gamma$ and the two main contribution are:

- $e^+e^- \rightarrow \omega\pi^0 \rightarrow \pi^0\pi^0\gamma$ ($\omega\pi$);
- $\phi \rightarrow S\gamma \rightarrow \pi^0\pi^0\gamma$ ($S\gamma$);

where S is $f_0(600) + f_0(980)$. We found a reasonable \sqrt{s} dependence of the cross section for the two processes.

In order to study the interference between the $\omega\pi$ and $S\gamma$ channels we do not divide the events in categories and we just fit the whole Dalitz. We present preliminary results about the fit to the Dalitz plot with improved KL

Parameter	KL	NS
m_{f_0} (MeV)	980–987	973–981
$g_{f_0 K^+ K^-}$ (GeV)	5.0–6.3	1.6–2.3
$g_{f_0 \pi^+ \pi^-}$ (GeV)	3.0–4.2	0.9–1.1
$R = g_{f_0 K^+ K^-}^2 / g_{f_0 \pi^+ \pi^-}^2$	2.2–2.8	2.6–4.4
$g_{\phi f_0 \gamma}$ (GeV $^{-1}$)	–	1.2–2.0

Table 2.2: *The KL-NS fit results: Interval of maximal variations for the f_0 parameters resulting from the systematic uncertainties studies done on both fits.*

parametrization from [21]: with a KK scattering phase; new parametrization of $\pi\pi$ scattering phase; scalar contributions from $f_0(980)$ and $f_0(600)(\sigma)$. The combined fit to the $\pi\pi$ scattering data and to already published KLOE data on $\phi \rightarrow S\gamma$ produces six different sets of parameters able to describe both distributions. In the KL fit we live as free parameters the mass of f_0 , the couplings $g_{f_0 \pi^+ \pi^-}$ and $g_{f_0 K^+ K^-}$, the VMD description; we fixed the $\pi\pi/KK$ phase and the $f_0(600)$ to the results of Achasov [21].

The preliminary results indicate a strong coupling of the $f_0(980)$ to kaons, in agreement with our own measurement in the $\pi^+ \pi^- \gamma$ final state, see Table 2.3. The presence of a $f_0(600)$ is needed to accurately describe the data. The fit with the NS approach is in progress.

	$f_0(980) + f_0(600)(M_{f_0(600)} \text{ fixed})$	$f_0(980) + f_0(600)(M_{f_0(600)} \text{ free})$
$M_{f_0(980)}$ (MeV)	$976.8 \pm 0.3 \pm 10.5$	$974.8 \pm 0.6 \pm 12.5$
$g_{f_0(980) K^+ K^-}$ (GeV)	$3.76 \pm 0.04 \pm 1.16$	$3.49 \pm 0.08 \pm 0.57$
$g_{f_0(980) \pi^+ \pi^-}$ (GeV)	$-1.43 \pm 0.01 \pm 0.60$	$-1.29 \pm 0.04 \pm 0.77$
$M_{f_0(600)}$ (MeV)	461 – 543	$551 \pm 15 - 76$
χ^2/ndf	2753/2676	2734/2675
$P(\chi^2)$	14.5%	20.8%

Table 2.3: *The KL-NS fit results: Interval of maximal variations for the f_0 parameters resulting from the systematic uncertainties studies done on both fits.*

2.2.2 $BR(\phi \rightarrow \eta' \gamma) / BR(\phi \rightarrow \eta \gamma)$

In order to measure the ratio $R = BR(\phi \rightarrow \eta' \gamma) / BR(\phi \rightarrow \eta \gamma)$ we search for $\phi \rightarrow \eta' \gamma$ with $\pi^+ \pi^- \gamma$ final state; it can be produced in two different decay

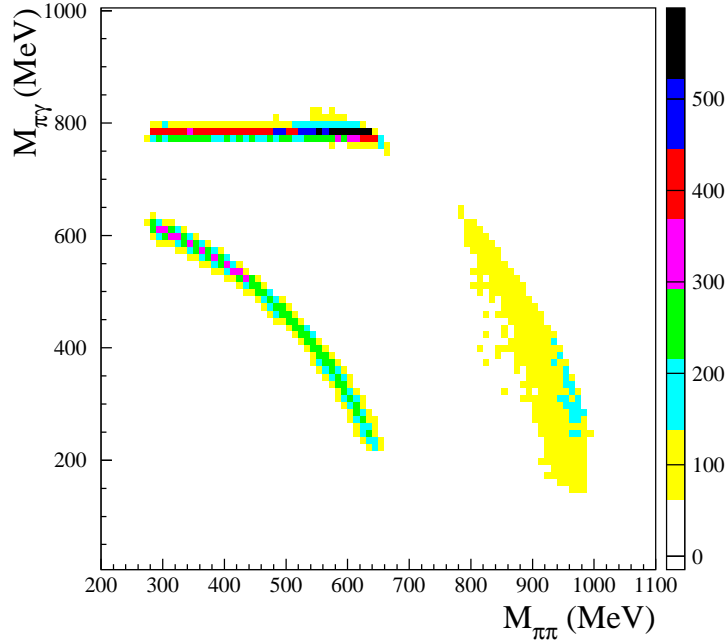


Figure 2.5: Dalitz plot for data clearly shows the presence of S_γ (top band) and $\omega\pi$ processes (bottom-left band).

chains:

$$\begin{aligned} \phi &\rightarrow \eta'\gamma, \quad \eta' \rightarrow \pi^+\pi^-\eta, \quad \eta \rightarrow 3\pi^0 \\ \phi &\rightarrow \eta'\gamma, \quad \eta' \rightarrow \pi^0\pi^0\eta, \quad \eta \rightarrow \pi^+\pi^-\pi^0 \end{aligned}$$

and for $\phi \rightarrow \eta\gamma$ with 7γ final state; it can be produced by:

$$\phi \rightarrow \eta\gamma, \quad \eta \rightarrow \pi^0\pi^0\pi^0$$

The following requirements are used to isolate all signal events:

- seven clusters in the calorimeter with $|t_{clu} - r_{clu}/c| < 5\sigma_t$, and $\theta_\gamma > 21^\circ$ respect to the beam direction.

For charged final state we ask also:

- one charged vertex in a cylinder with a 4 cm radius and a 16 cm height around the interaction point

All events identified as $K_S K_L$ pair are rejected. A kinematic fit is performed with energy-momentum conservation imposed, and the χ^2 is used as selection

variable. From the analysis of 427 pb^{-1} we select 3750 candidate events for $\phi \rightarrow \eta'\gamma$, the background, as estimated from MonteCarlo simulation of all physical processes that can be identified as signal, is 345

$$N_{sig} = N_{obs} - N_{backg.} = 3405 \pm 65_{stat} \pm 28_{syst}$$

Combining the previous measurement with the study of $\phi \rightarrow \eta\gamma$ decays ($N_{\eta \rightarrow 3\pi^0} = 1665000 \pm 1300$) we can calculate the ratio of the two Branching Ratios:

$$R = \frac{N_{\eta'\gamma}}{N_{\eta\gamma}} \frac{\varepsilon_{\eta\gamma} BR_{\eta\gamma}}{\varepsilon_{\eta'\gamma}^{char} BR_{\eta'\gamma}^{char} + \varepsilon_{\eta'\gamma}^{neu} BR_{\eta'\gamma}^{neu}} \cdot K_\rho$$

$$BR_{\eta'\gamma}^{char} = BR(\eta' \rightarrow \pi^+\pi^-\eta) \cdot BR(\eta \rightarrow 3\pi^0)$$

$$BR_{\eta'\gamma}^{neu} = BR(\eta' \rightarrow \pi^0\pi^0\eta) \cdot BR(\eta \rightarrow \pi^+\pi^-\pi^0)$$

The factor K_ρ is a correction to the observed decay rate due to the interference between $\phi \rightarrow \eta(\eta')\gamma$ and $\rho \rightarrow \eta(\eta')\gamma$. The main source of systematic error comes from the uncertainty on the $\eta' \rightarrow \pi^+\pi^-\eta$ and $\eta' \rightarrow \pi^0\pi^0\eta$ Branching Ratios (3%). Using the expression for R we obtain the result [22]:

$$R = (4.74 \pm 0.09_{stat} \pm 0.20_{sys}) \cdot 10^{-3}$$

and the pseudoscalar mixing angle:

$$\varphi_P = (41.4 \pm 0.3_{stat} \pm 0.7_{sys} \pm 0.6_{th})^\circ,$$

calculated using the procedure described in [23].

2.3 Hadronic cross-section

The precision measurement of the muon anomaly a_μ at the Brookhaven National Laboratory [24] has led to renewed interest in an accurate measurement of the cross section for e^+e^- annihilation into hadrons.

Infact, the hadronic contribution to a_μ at low energy cannot be computed, but it is related to $\sigma(e^+e^- \rightarrow \text{hadrons})$ via a dispersion integral.

The process $e^+e^- \rightarrow \pi^+\pi^-$ below 1 GeV accounts for the 62% of the total hadronic contribution. The most recent measurements of $\sigma(e^+e^- \rightarrow \pi^+\pi^-)$ for values of \sqrt{s} between 619 and 691 MeV come from the CMD-2 experiment at VEPP-2M where the quoted systematic error is 0.6% and the contribution of statistical error on a_μ^{hadr} is $\sim 0.7\%$ [25, 26].

These data together with τ and e^+e^- data up to 3 GeV, have been used to produce a prediction for comparison with the BNL result [27]. There is however a rather strong disagreement between a_μ^{hadr} value obtained using τ decay data after isospin-breaking corrections and $e^+e^- \rightarrow \pi^+\pi^-$ data. Moreover, the $e^+e^- \rightarrow \pi^+\pi^-$ base result disagrees by $\sim 3\sigma$ with the direct measurement of a_μ .

KLOE can measure the hadronic cross section via the “radiative return” [28]: Initial State Radiation (ISR) from the beams can lower the value of \sqrt{s} down to the $\pi^+\pi^-$ threshold.

KLOE $\pi\pi\gamma$ events are selected asking for two charged tracks coming from the interaction region with an angle respect to the beam pipe $50^\circ < \theta < 130^\circ$. Additional cuts on the momentum, $p_T > 160$ MeV or $|p_Z| > 90$ MeV, are used to reject tracks spiraling along the beam line.

In order to suppress the events in which the $\pi\pi$ invariant mass is reduced by the presence of a Final State Radiated (FSR) photon, a cut on the missing momentum angle, $\theta_{miss} < 15^\circ$ or $\theta_{miss} > 165^\circ$, is imposed.

Background from Bhabha scattering, $\phi \rightarrow \pi^+\pi^-\pi^0$ decays and $e^+e^- \rightarrow \mu^+\mu^-\gamma$ events is suppressed using a particle identification method based on the time of flight, the energy deposit in the calorimeter and the kinematic closure of the event in the hypothesis of only one photon in the final state.

Residual background is evaluated from the fit of the mass distribution of the charged particles and subtracted. Selected efficiency is better than 96%. The PHOKHARA generator [29], is then used to relate $\sigma(e^+e^- \rightarrow \pi^+\pi^-\gamma)$ to $\sigma(e^+e^- \rightarrow \pi^+\pi^-)$. After correcting for the vacuum polarization the bare $e^+e^- \rightarrow \pi^+\pi^-$ cross section shown in Figure 2.6 is obtained.

These values has been used to evaluate the contribution to a_μ^{had} due to the $\pi^+\pi^-$ channel in the energy range $0.35 < s_\pi < 0.95$ GeV². The resulting value (in 10^{-10} units) is:

$$a_\mu^{\pi\pi}(0.35, 0.95) = 388.7 \pm 0.8_{stat} \pm 3.5_{syst} \pm 3.5_{th} \quad (2.21)$$

where the theoretical error comes from the knowledge of the vacuum polarization and the Bhabha cross section used to determine the luminosity.

2.4 $\eta \rightarrow 3\pi^0$ within a chiral approach

A major tool in η decay studies is Chiral Perturbation Theory (ChPT) [30, 31]; in the following a short description of ChPT is given.

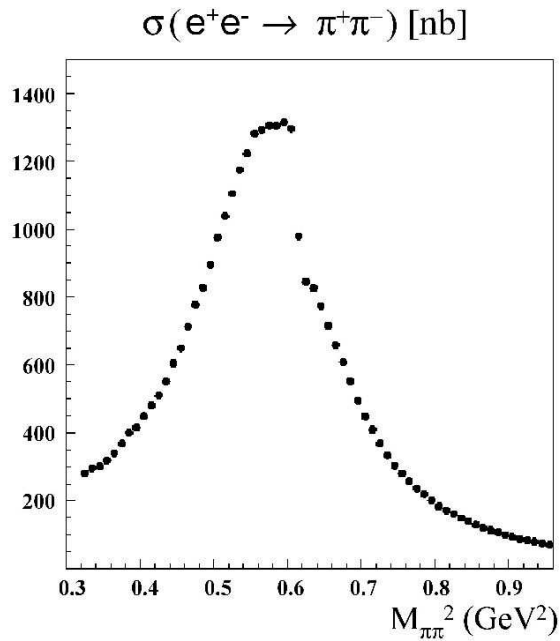


Figure 2.6: *Cross section for $e^+e^- \rightarrow \pi^+\pi^-$.*

2.4.1 Standard Chiral Perturbation Theory

QCD is nowadays the established theory of the strong interactions. Owing to its asymptotic-free nature, perturbation theory can be applied at short distances; the resulting predictions have achieved a remarkable success, explaining a wide range of phenomena where large momentum transfers are involved. In the low-energy domain, however, the growing of the running QCD coupling and the associated confinement of quarks and gluons make very difficult to perform a thorough analysis of the QCD dynamics in terms of these fundamental degrees of freedom.

A description in terms of the hadronic asymptotic states seems more adequate; unfortunately, given the richness of the hadronic spectrum, this is also a formidable task.

At very low energies, a great simplification of the strong-interaction dynamics occurs. Below the resonance region ($E < M_\rho$), the hadronic spectrum only contains an octet of very light pseudoscalar particles (π, K, η), whose interactions can be easily understood with global symmetry considerations. This has allowed the development of a powerful theoretical framework, Chiral Perturbation Theory (ChPT), to systematically analyze the lowenergy implications of the QCD symmetries. This formalism is based on two key

ingredients: the chiral symmetry properties of QCD and the concept of EFT.

2.4.2 Chiral symmetry

The best definition of symmetry for our purposes is probably that due to the mathematician Herman Weyl who said that a system is symmetric when one can do something to it and, after making this change, the system looks the same as it did before [32]. The importance of symmetry in physics is due to an important result –Noethers theorem– which connects each symmetry of a system with a corresponding conserved current and conservation law [33]. In order to understand the relevance of symmetry within QCD, we must introduce the idea of “chirality”, defined by the operators

$$\Gamma_{L,R} = \frac{1}{2}(1 \pm \gamma_5) = \frac{1}{2} \begin{pmatrix} 1 & \pm 1 \\ \pm 1 & 1 \end{pmatrix} \quad (2.22)$$

which project left and right-handed components of the Dirac wavefunction via

$$\Psi_L = \Gamma_L \Psi \quad \Psi_R = \Gamma_R \Psi \quad \text{with} \quad \Psi = \Psi_L + \Psi_R \quad (2.23)$$

In terms of these chirality states the quark component of the QCD Lagrangian can be written as

$$\bar{q} (i \not{D} - m) q = \bar{q}_L i \not{D} q_L + \bar{q}_R i \not{D} q_R - \bar{q}_L m q_R - \bar{q}_R m q_L \quad (2.24)$$

The reason that these chirality states are called left and right-handed can be seen by examining helicity eigenstates of the free Dirac equation. In the high energy (or massless) limit we note that

$$u(p) = \sqrt{\frac{E+m}{2E}} \begin{pmatrix} \chi \\ \frac{\vec{\sigma} \cdot \vec{p}}{E+m} \chi \end{pmatrix} \stackrel{E \gg M}{\sim} \sqrt{\frac{1}{2}} \begin{pmatrix} \chi \\ \vec{\sigma} \cdot \hat{p} \chi \end{pmatrix} \quad (2.25)$$

Left and right-handed helicity eigenstates then can be identified as

$$u_L(p) \sim \sqrt{\frac{1}{2}} \begin{pmatrix} \chi \\ -\chi \end{pmatrix}, \quad u_R(p) \sim \sqrt{\frac{1}{2}} \begin{pmatrix} \chi \\ \chi \end{pmatrix} \quad (2.26)$$

But

$$\Gamma_L u_L = u_L, \quad \Gamma_R u_L = 0 \quad (2.27)$$

$$\Gamma_R u_R = u_R, \quad \Gamma_L u_R = 0 \quad (2.28)$$

so that in this limit chirality is identical with helicity

$$\Gamma_{L,R} \sim \text{helicity!} \quad (2.29)$$

With this background, we now return QCD and observe that in the limit as $m_u = m_d = m_s = 0$

$$\mathcal{L}_{QCD}^1 = \bar{q} (i \not{D} - m) q - \frac{1}{2} \text{tr} G_{\mu\nu} G^{\mu\nu} \quad (2.30)$$

became:

$$\bar{q}_L i \not{D} q_L + \bar{q}_R i \not{D} q_R \quad (2.31)$$

and this is invariant under independent global left- and right-handed rotations

$$q_L \rightarrow \exp \left(i \sum_j \lambda_j \alpha_j \right) q_L, \quad (2.32)$$

$$q_R \rightarrow \exp \left(i \sum_j \lambda_j \beta_j \right) q_R \quad (2.33)$$

$$(2.34)$$

This invariance is called $SU(3)_L \otimes SU(3)_R$ or chiral $SU(3) \times SU(3)$. Continuing to neglect the light quark masses, we see that in a chiral symmetric world one would expect to have eight left-handed and eight right-handed-conserved Noether's currents

$$\bar{q}_L \gamma_\mu \frac{1}{2} \lambda^i q_L, \quad \bar{q}_R \gamma_\mu \frac{1}{2} \lambda^i q_R. \quad (2.35)$$

¹Here the covariant derivative is

$$iD_\mu = i\partial_\mu - gA_\mu^a \frac{\lambda^a}{2} \quad (1)$$

where λ^a (with $a = 1, \dots, 8$) are the $SU(3)$ Gell-Mann matrices, operating in color space, and the color-field tensor is defined by

$$G_{\mu\nu} = \partial_\mu A_\nu - \partial_\nu A_\mu - g[A_\mu, A_\nu]. \quad (2)$$

Equivalently, by taking the sum and difference we would have eight conserved vector and eight conserved axial vector currents

$$V_\mu^i = \bar{q}\gamma_\mu \frac{1}{2}\lambda_i q, \quad A_\mu^i = \bar{q}\gamma_\mu \gamma_5 \frac{1}{2}\lambda_i q. \quad (2.36)$$

There exist eight $(3^2 - 1)$ time-independent charges

$$Q_i = \int d^3x V_i^0(\vec{x}, t), \quad (2.37)$$

and there exist various supermultiplets of particles having identical spin-parity and (approximately) the same mass in the configurations-singlet, octet, decuplet, etc. demanded by $SU(3)$ invariance.

If chiral symmetry were realized in the conventional fashion one would expect there also to exist corresponding nearly degenerate but opposite parity states generated by the action of the time-independent axial charges $Q_i^5 = \int d^3x A_0^i(\vec{x}, t)$ on these states.

We observe that the symmetry $SU(3)_R \times SU(3)_L$ of the QCD lagrangian not is a vacuum symmetry:

$$Q_i|0\rangle = 0 \quad Q_i^5|0\rangle \neq 0 \quad (2.38)$$

So, according to Goldstones argument, one would expect there to exist eight massless pseudoscalar states-one for each spontaneously broken $SU(3)$ axial generator, which would be the Goldstone bosons of QCD. Examination of the particle data tables reveals, however, that no such massless 0^- particles exist. There do exist eight 0^- particles $-\pi^\pm, \pi^0, K^\pm, K^0, \bar{K}^0, \eta^-$ which are much lighter than their hadronic siblings. However, these states are certainly not massless and this causes us to ask what has gone wrong with what appears to be rigorous reasoning. The answer is found in the feature that our discussion thus far has neglected the piece of the QCD Lagrangian which is associated with quark mass and can be written in the form

$$\mathcal{L}_{QCD}^m = -(\bar{u}_L u_R + \bar{u}_R u_L) m_u - (\bar{d}_L d_R + \bar{d}_R d_L) m_d \quad (2.39)$$

Since clearly this term breaks the chiral symmetry

$$\bar{q}_L q_R \rightarrow \bar{q}_L \exp\left(i \sum_j \lambda_j \alpha_j\right) \times \exp\left(i \sum_j \lambda_j \beta_j\right) q_R \neq \bar{q}_L q_R \quad (2.40)$$

we have a violation of the conditions under which Goldstones theorem applies. The associated pseudoscalar bosons are not required to be massless

$$m_G^2 \neq 0 \quad (2.41)$$

but since their mass arises only from the breaking of the symmetry the various “would-be” Goldstone masses are expected to be proportional to the symmetry breaking parameters

$$m_G^2 \propto m_u, m_d, m_s \quad (2.42)$$

To the extent that such quark masses are small the eight pseudoscalar masses are not required to be massless, merely much lighter than other hadronic masses in the spectrum, as found in nature.

2.4.3 Effective chiral Lagrangian

The existence of a set of particles –the pseudoscalar mesons– which are notably less massive than other hadrons suggests the possibility of generating an effective field theory which correctly incorporates the chiral symmetry of the underlying QCD Lagrangian in describing the low energy interactions of these would be Goldstone particles.

We infer then that the lowest order effective chiral Lagrangian can be written as

$$\mathcal{L}_2 = \frac{F_\pi^2}{4} \text{Tr} (\partial_\mu U \partial^\mu U^\dagger) + \frac{m_\pi^2}{4} F_\pi^2 \text{Tr} (U + U^\dagger) \quad (2.43)$$

where the subscript 2 indicates that we are working at two-derivative order or one power of chiral symmetry breaking i.e. m_π^2 .

The matrix $U \in SU(3)$ is defined as:

$$U(\phi) \equiv \exp \left\{ i\sqrt{2} \frac{\Phi}{F_\pi} \right\} \quad (2.44)$$

with $F_\pi = 92.4$ MeV, pion decay constant, and Φ as:

$$\Phi(x) = \frac{\vec{\lambda}}{\sqrt{2}} \vec{\phi} = \begin{pmatrix} \frac{1}{\sqrt{2}}\pi^0 + \frac{1}{\sqrt{6}}\eta_8 & \pi^+ & K^+ \\ \pi & \frac{1}{\sqrt{2}}\pi^0 + \frac{1}{\sqrt{6}}\eta_8 & K^0 \\ K & \bar{K}^0 & \frac{2}{\sqrt{6}}\eta_8 \end{pmatrix}. \quad (2.45)$$

if we expand to lowest order in $\vec{\phi}$

$$\text{Tr} (\partial_\mu U \partial^\mu U^\dagger) = \text{Tr} \frac{i}{F_\pi} \vec{\tau} \cdot \partial_\mu \vec{\phi} \times \frac{-i}{F_\pi} \vec{\tau} \cdot \partial^\mu \vec{\phi} = \frac{2}{F_\pi^2} \partial_\mu \vec{\phi} \cdot \partial^\mu \vec{\phi} \quad (2.46)$$

$$\text{Tr} (U + U^\dagger) = \text{Tr} \left(2 - \frac{1}{F_\pi^2} \vec{\tau} \cdot \vec{\phi} \vec{\tau} \cdot \vec{\phi} \right) = \text{const} - \frac{2}{F_\pi^2} \vec{\phi} \cdot \vec{\phi} \quad (2.47)$$

we reproduce the free pion Lagrangian, as required,

$$\mathcal{L}_2 = \frac{1}{2} \partial_\mu \vec{\phi} \partial^\mu \vec{\phi} - \frac{1}{2} m_\pi^2 \vec{\phi} \vec{\phi} + \mathcal{O}(\phi^4). \quad (2.48)$$

Including a generalized chiral symmetry breaking term, one has

$$\begin{aligned} \frac{F_\pi^2}{4} \text{Tr} \partial_\mu U \partial^\mu U^\dagger &= \frac{1}{2} \sum_{j=1}^8 \partial_\mu \phi_j \partial^\mu \phi_j + \dots \\ \frac{F_\pi^2}{4} \text{Tr} 2 B_0 m (U + U^\dagger) &= \text{const} - \frac{1}{2} (m_u + m_d) B_0 \sum_{j=1}^3 \phi_j^2 \\ &\quad - \frac{1}{4} (m_u + m_d + 2m_s) B_0 \sum_{j=4}^7 \phi_j^2 \\ &\quad - \frac{1}{6} (m_u + m_d + 4m_s) B_0 \phi_8^2 \end{aligned}$$

where B^0 is a constant and m is the quark mass matrix $m = (m_u, m_d, m_s)_{diag}$. We can then identify the meson masses as

$$m_\pi^2 = 2\hat{m}B_0 \quad (2.49)$$

$$m_K^2 = (\hat{m} + m_s) B_0 \quad (2.50)$$

$$m_\eta^2 = \frac{2}{3} (\hat{m} + 2m_s) B_0 \quad (2.51)$$

where $\hat{m} = \frac{1}{2}(m_u + m_d)$ is the mean light quark mass. This system of three equations is overdetermined, and we find by simple algebra

$$3m_\eta^2 + m_\pi^2 - 4m_K^2 = 0 \quad (2.52)$$

Moreover, expanding \mathcal{L}_2 to order ϕ^4 we determine values for the pion scattering lengths (Weinberg):

$$a_0^0 = \frac{7m_\pi^2}{32\pi F_\pi^2} \quad a_0^2 = -\frac{m_\pi^2}{16\pi F_\pi^2} \quad a_1^1 = \frac{m_\pi^2}{24\pi F_\pi^2}. \quad (2.53)$$

Loop diagrams, of course, produce terms $\mathcal{O}(p^4, p^2, m^2, m^4)$ and contain divergences. However, just as in QED such infinities can be observed into renormalizing phenomenological chiral couplings, and the most general “four

derivative" Lagrangian has been given by Gasser and Leutwyler [30]:

$$\begin{aligned} \mathcal{L}_4 = \sum_{i=1}^{10} L_i \mathcal{O}_i = & L_1 [Tr (D_\mu U D^\mu U^\dagger)]^2 + L_2 Tr (D_\mu U D_\nu U^\dagger) \cdot Tr (D^\mu U D^\nu U^\dagger) \\ & + L_3 Tr (D_\mu U D^\mu U^\dagger D_\nu U D^\nu U^\dagger) + L_4 Tr (D_\mu U D^\mu U^\dagger) Tr (\chi U^\dagger + U \chi^\dagger) \\ & + L_5 Tr (D_\mu U D^\mu U^\dagger (\chi U^\dagger + U \chi^\dagger)) + L_6 [(\chi U^\dagger + U \chi^\dagger)]^2 \\ & + L_7 [(\chi U^\dagger - U \chi^\dagger)]^2 + L_8 (\chi U^\dagger \chi U^\dagger + U \chi^\dagger U \chi^\dagger) \\ & + i L_9 Tr (F_{\mu\nu}^L D^\mu U D^\nu U^\dagger + F_{\mu\nu}^R D^\mu U^\dagger D^\nu U) + L_{10} Tr (F_{\mu\nu}^L U F^{R\mu\nu} U^\dagger) \end{aligned}$$

where the covariant derivative is defined via

$$D_\mu U = \partial_\mu U + \{A_\mu, U\} + [V_\mu, U], \quad (2.54)$$

the constants $L_i, i = 1, 2, \dots, 10$ are arbitrary (not determined from chiral symmetry alone) and $F_{\mu\nu}^L, F_{\mu\nu}^R$ are external field strength tensors defined via

$$F_{\mu\nu}^{L,R} = \partial_\mu F_\nu^{L,R} - \partial_\nu F_\mu^{L,R} - i [F_\mu^{L,R}, F_\nu^{L,R}] \quad (2.55)$$

$$F_\mu^{L,R} = V_\mu \pm A_\mu. \quad (2.56)$$

The important question to ask at this point is why stop at order four derivatives. Clearly if two loop amplitudes from \mathcal{L}_2 or one-loop corrections from \mathcal{L}_4 are calculated, divergences will arise which are of six derivative character. Why not include these ?

The answer is that the chiral procedure represents an expansion in energy-momentum. Corrections to the lowest order (tree level) predictions from one loop corrections from \mathcal{L}_2 or tree level contributions from \mathcal{L}_4 are $\mathcal{O}(E^2/\Lambda_\chi^2)$ where $\Lambda_\chi \sim 4\pi F_\pi \sim 1$ GeV is the chiral scale. Thus chiral perturbation theory is a low energy procedure. It is only to the extent that the energy is small compared to the chiral scale that it makes sense to truncate the expansion at the four-derivative level. Realistically this means that we deal with processes involving $E < 500$ MeV, and, as we shall describe below, for such reactions the procedure is found to work very well.

2.4.4 $\eta \rightarrow \pi^0 \pi^0 \pi^0$ decay

The η is an isospin singlet and a pseudo-scalar. Three pions in an angular momentum 0 configuration cannot have isospin zero as well, but isospin 1 is

allowed.

The decay $\eta \rightarrow 3\pi$ thus has to proceed via isospin breaking effects. Electromagnetism is known to play a fairly minor role (which is justified according to Sutherland's theorem [34]), except via the kinematical effects due to the charged and neutral pion mass difference.

This decay goes primarily through the strong isospin breaking part of QCD:

$$\mathcal{L}_I = -\frac{1}{2} (m_u - m_d) (\bar{u}u - d\bar{d}). \quad (2.57)$$

This itself has isospin 1 and there is thus to lowest order in isospin breaking a relation between $\eta \rightarrow \pi^+\pi^-\pi^0$ and $\eta \rightarrow \pi^0\pi^0\pi^0$.

Thus, labelling the three momenta of pions as p_1, p_2, p_3 and $s_i = (p_\eta - p_i)^2$, the amplitude for the neutral decay satisfies:

$$\begin{aligned} A_{\eta \rightarrow 3\pi^0}(s_1, s_2, s_3) &= A_{\eta \rightarrow \pi^0\pi^+\pi^-}(s_1, s_2, s_3) + A_{\eta \rightarrow \pi^0\pi^+\pi^-}(s_2, s_3, s_1) \\ &\quad + A_{\eta \rightarrow \pi^0\pi^+\pi^-}(s_3, s_1, s_2) \end{aligned}$$

see [35] for a detailed derivation of this result.

The lowest order of ChPT contribution from the quark mass difference, using current algebra methods, is

$$A_{\eta \rightarrow \pi^+\pi^-\pi^0}(s_1, s_2, s_3) = \frac{B_0(m_u - m_d)}{3\sqrt{3}F_\pi^2} \left\{ 1 + \frac{3(s_1 - s_0)}{m_\eta^2 - m_\pi^2} \right\} \quad (2.58)$$

or, with $Q^2 \equiv (m_s^2 - \hat{m}^2)/(m_d^2 - m_u^2)$ and $\hat{m} = (m_u + m_d)/2$, it becomes

$$A_{\eta \rightarrow \pi^+\pi^-\pi^0}(s_1, s_2, s_3) = \frac{1}{Q^2} \frac{m_K^2}{m_\pi^2} (m_\pi^2 - m_K^2) \frac{M(s_1, s_2, s_3)}{3\sqrt{3}F_\pi^2} \quad (2.59)$$

with at lowest order,

$$M(s_1, s_2, s_3) = \frac{3s_1 - 4m_\pi^2}{m_\eta^2 - m_\pi^2} \quad (2.60)$$

That the decay rate $\Gamma(\eta \rightarrow 3\pi)$ is thus proportional to Q^{-4} , allows a precise measurement of Q . To illustrate this we take Q from the baryon mass difference, $Q \sim 24$, and obtain at lowest order

$$\Gamma(\eta \rightarrow \pi^+\pi^-\pi^0) = 88 \text{ eV}, \quad \Gamma(\eta \rightarrow \pi^0\pi^0\pi^0) = 134 \text{ eV} \quad (2.61)$$

in strong disagreement with the experimental results

$$\Gamma^{exp}(\eta \rightarrow \pi^+\pi^-\pi^0) = (291 \pm 22) \text{ eV} \quad (2.62a)$$

$$\Gamma^{exp}(\eta \rightarrow \pi^0\pi^0\pi^0) = (419 \pm 27) \text{ eV}. \quad (2.62b)$$

An alternative determination from $(m_{K^+}^2 - m_{K^0}^2) \sim Q^{-2}$ gives $Q = 20.0 \pm 1.5$ and leads to a lowest order prediction

$$\Gamma(\eta \rightarrow \pi^+\pi^-\pi^0) \sim 140 \text{ eV} \quad (2.63)$$

The p^4 , p^6 calculations [36] that mainly include the effects of the final state rescattering, give a very large enhancement ($\Gamma(\eta \rightarrow \pi^+\pi^-\pi^0) \sim 240 \text{ eV}$) but the discrepancy between the experimental and theoretical results is always present.

The Dalitz plot distribution of $\eta \rightarrow 3\pi^0$ thus provide a check on the various theoretical assumptions.

2.5 Dalitz plot of $\eta \rightarrow \pi^0\pi^0\pi^0$ decay

The partial decay rate of a particle of mass M into n bodies in its rest frame is given in terms of the Lorentz-invariant matrix element \mathcal{A} by:

$$d\Gamma = \frac{2\pi^4}{2M} \sum_{spin} |\mathcal{A}|^2 d\Phi_n(P; p_1, \dots, p_n) \quad (2.64)$$

where $d\Phi_n$ is an element of n -body phase space given by:

$$d\Phi_n = \delta^4(P - \sum_{i=1}^n p_i) \prod_{i=1}^n \frac{d^3p_i}{(2\pi)^3 2E_i} \quad (2.65)$$

In general the matrix element may be unknown; in the extreme case of a constant matrix element the transition rate, and indeed the momentum distributions of the final state particles, are governed by the phase space factor. It is important therefore to be able to compute the latter. In principle, any deviations from phase space provide information about the matrix element. The present work is devoted to the investigation of the dynamic of $\eta \rightarrow 3\pi^0$. The $\eta \rightarrow \pi^0\pi^0\pi^0$ is a three body decay, so there are $3 \times 4 = 12$ variables, namely the quadri-momenta of each pion.

Then we can subtract 3 for the three known masses of the pions, and 4 for the energy-momentum conservation (we consider the decay in the reference frame in which the η is at rest).

We are left with 5 variables, 2 of them define the orientation of the decay

plane, the other 3 the way the three particles are produced in the decay plane, one is an angle around the normal to the plane and finally the 2 remaining variable describe the dynamic of decay. The scatter plot in these two variables is called Dalitz plot.

If $|\mathcal{A}|^2$ is constant, the allowed region of the plot will be uniformly populated, a non uniformity in the plot gives immediate information on $|\mathcal{A}|^2$. Since the three decay particles have equal masses it is convenient to make this symmetry explicit by using all three energies simultaneously and by plotting in polar coordinates (ρ, ϕ) defined as:

$$E_1 = \frac{M_\eta}{3} \left[1 + \varepsilon \rho \cos \left(\phi - \frac{2\pi}{3} \right) \right] \quad (2.66)$$

$$E_2 = \frac{M_\eta}{3} \left[1 + \varepsilon \rho \cos \left(\phi + \frac{2\pi}{3} \right) \right] \quad (2.67)$$

$$E_3 = \frac{M_\eta}{3} [1 + \varepsilon \rho \cos \phi] \quad (2.68)$$

with:

$$\varepsilon = 1 - \frac{3m_{\pi^0}}{M_\eta} \quad (2.69)$$

The curve bounding the kinematically accessible region is then obtained by the equation:

$$1 = (1 + x) \rho^2 + x \rho^3 \cos 3\phi \quad (2.70)$$

where $x = 2\varepsilon/(2 - \varepsilon)^2$. It is seen that ε characterizes the curve completely, its value for $\eta \rightarrow 3\pi^0$ decay is 0.26.

The experimental Dalitz plot is linearized by introducing the variable z :

$$z = \frac{2}{3} \sum_{i=1}^3 \left(\frac{3E_i - m_\eta}{m_\eta - 3m_{\pi^0}} \right)^2 = \frac{\rho^2}{\rho_{max}^2} \quad (2.71)$$

where ρ is the distance from the center of Dalitz plot.

In ring intervals $[\rho, \rho + d\rho]$ around this center the plot density should be constant. The coefficient α in the expansion of the decay amplitude around the center of the Dalitz plot

$$|\mathcal{A}|^2 \sim 1 + 2\alpha z \quad (2.72)$$

is a measure of non uniformity.

2.5.1 Theoretical and experimental results on the Dalitz plot parameter

In Table 2.4 we show the theoretical and experimental results for the slope parameter α . Note that the one loop predictions of the neutral slope α is not zero; the loop themselves do give a contribution, whereas the contributions from the three level and tadpole diagrams at $\mathcal{O}(p^4)$ happen vanish.

	α
<i>tree</i>	0.000
<i>one-loop</i> [30]	0.015
<i>dispersive</i> [37]	-0.014 -0.007
<i>tree dispersive</i> [38]	-0.006
<i>absolute dispersive</i> [38]	-0.007
<i>unitary</i> [39]	-0.031

Table 2.4: *Theoretical results for the slope parameter of the various approximations.*

The precise value is dependent on the procedure used and is sensitive to fairly small changes. The number quoted $\alpha = 0.015$ has been obtained from the representation of the amplitude provided in [30].

The experimental results are shown in Table 2.5.

	α
Alde [40]	-0.022 ± 0.023
Crystal Barrel [41]	-0.052 ± 0.019
Crystal Ball [42]	-0.031 ± 0.004

Table 2.5: *Experimental results for the slope parameter in the neutral decay. We have added in quadrature the statistical and systematical errors quoted in [41].*

The large negative slope parameter α measured by Crisall Ball Collaboration with a unprecedented precision is in agreement with the theoretical result obtained in the chiral unitary approach based on the Bethe–Salpeter equation, but is not compatible with the theoretical investigations see Table 2.4. A new measurement of the slope parameter could be helpful to clarify the theoretical and experimental scenario.

Chapter 3

Data reconstruction and event classification

3.1 Data reconstruction

The reconstruction of raw data, which are written to mass storage by the DAQ system, starts with the translation, performed through the detector maps, of electronic addresses into geographical detector addresses: time and position of the DC hits and time, position and released energy of the EMC cells. These quantities are then processed in order to reconstruct the physical quantities of the events.

3.1.1 Clustering

The clustering algorithm for the KLOE Electromagnetic Calorimeter, has to reconstruct the energy, impact point and the arrival time of each photons that reach the calorimeter.

Let us call *cell* a calorimeter segment, which is defined as the smallest calorimeter physical channel viewed by two photo-multipliers in the plane transversal to the fibre direction. For each cell two time signals, $t^{A,B}$ and two amplitude signals $S^{A,B}$ are recorded from the photo-multipliers on the

two side of the fibre. The longitudinal position of the energy deposit is derived from the time difference between the two ends of the fibre, $t^A - t^B$. Let us define some useful variables:

- the TDC calibration constants $c^{A,B}$, in $\text{ns}/\text{TDC counts}$;
- the average times measured in a dedicate run $T^{A,B}$;
- the fine corrections to the time offsets $t_0^{A,B}$;
- the cell length L (cm);
- the light velocity in the fibres v (cm/ns);

The particle arrival time t and its coordinate z along the fibre direction are obtained from these variables as:

$$t = \frac{t^A + t^B}{2} - \frac{t_0^A + t_0^B}{2} - \frac{L}{2v} \quad (3.1)$$

$$z = \frac{v}{2} [t^A - t^B - (t_0^A - t_0^B)] \quad (3.2)$$

with

$$t^{A,B} = c^{A,B} \times T^{A,B} \quad (3.3)$$

The energy signal on each side of a cell i is defined as:

$$E_i^{A,B} = \frac{S_i^{A,B} - S_{0,i}^{A,B}}{S_{M,i}} \times k_E \quad (3.4)$$

where S are the ADC counts, $S_{0,i}$ are the zero offsets of the amplitude scale, $S_{M,i}$ is the response for a minimum ionising particle crossing the calorimeter centre and k_E is a scale factor, that gives the energy scale in MeV. The energy of the cell is obtained as the average of the two sides weighted with a factor that takes into account the attenuation due to the light propagation along the fibre:

$$E_i^{cell} = \frac{E_i^A A_i^A + E_i^B A_i^B}{2} \quad (3.5)$$

The *clustering algorithm* works to put together cells hit by the same particle: joining the adjacent cells to form pre-clusters and then these pre-clusters are joined or split using both time and position informations.

The cluster time is defined as the energy weighted average of the times of the cells belonging to it:

$$t_{cl} = \frac{\sum_{cells} E_i t_i}{\sum_{cells} E_i} \quad (3.6)$$

The same procedure is used for the three coordinates of the clusters:

$$x_{cl} = \frac{\sum_{cells} E_i x_i}{\sum_{cells} E_i} \quad (3.7)$$

$$y_{cl} = \frac{\sum_{cells} E_i y_i}{\sum_{cells} E_i} \quad (3.8)$$

$$z_{cl} = \frac{\sum_{cells} E_i z_i}{\sum_{cells} E_i} \quad (3.9)$$

A significant systematic effect induced by the clustering is the production of spurious clusters from the splitting of a unique energy deposit in the calorimeter.

This effect is strongly dependent on the energy of the particle releasing its energy and on the position of the cluster in the EMC and affects the photon multiplicity observed by the detector in a given event. For this reason it has been studied on well-defined photons samples such as those produced in $e^+e^- \rightarrow e^+e^-\gamma$ events and in ϕ radiative decays. The probability of having a cluster splitting is computed as a function of cluster energy and polar angle, and is finally used to unfold the true multiplicities from the observed ones.

After cluster reconstruction, an estimate of the reference time of the event (the absolute $T0$) is given by assuming that the first cluster in time is due to a prompt photon coming from the origin; this photon must have at least 50 MeV and must lie farther than 60 cm from the collision axis. The hypothesis of the being a prompt cluster reasonably fits a large set of events (radiative ϕ decays, $K_S^0 K_L^0$ with at least a γ or a π^0 produced, $e^+e^- \rightarrow e^+e^-\gamma$), but is inadequate to describe K^+K^- events: in the charged kaon case, after event classification, a new estimation of the $T0$ must be done. Once that the absolute $T0$ is determined, it is taken as reference for all the times of the event.

3.1.2 Tracking

The tracking and vertexing procedure [43, 44] are based on the algorithms developed for the ARGUS drift chamber [45], and are modified to take into account the stereo geometry of the KLOE drift chamber and to optimize the vertex-finding efficiency over all the detecting volume.

The chamber operates with a helium-based gas mixture to minimize the tracks multiple scattering.

Due to the large cell dimensions the drift velocity is not saturated and the cell response is not linear. Specific sets of space to time relations (s-t relations), which allow to reconstruct the distance of closest approach of the particle to the sense wire, are computed as function of the drift time. Due to the square shape of the drift cell and to the deformations induced on it by the stereo geometry, the s-t relations depend on the spatial coordinates of the cell and on the incidence direction of the track in the cell. This dependence has been parametrized according to two variables (defined as shown in Figure 3.1): the track incidence angle $\tilde{\phi}$ and the shape parameter β , which takes into

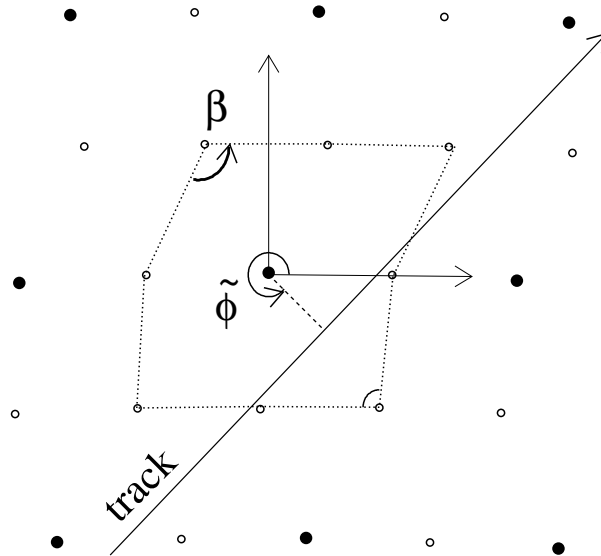


Figure 3.1: *Definitions of the variables used in the s-t relations classification.*

account the peculiar geometry of the upper part of the cell. It has been seen [46] that 232 parameterizations accounting for cell type (small or big), track orientation, and cell shape, are a reasonable compromise which allows a good description of the s-t relations and a limited number of parameterizations. The s-t relations are parametrized in terms of a 5th order Chebychev poly-

nomial, $d(C_k, t - T_0)$, and the C_k are 6×232 coefficients.

The track reconstruction procedure starts with the **pattern recognition**. The pattern recognition gives also a first estimate of the track parameters. Owing to the stereo geometry of the drift chamber, the hits are distributed on 2 nearby curves when projected onto the x - y plane. One of these curve is made up by the hits which fire wires with the positive stereo angle and the other one by the hits of wires with negative angle.

The pattern recognition first combines the hits on each view separately. The 2D candidates are then matched and merged to define the final track candidate. In merging the two views the z information is also extracted and an evaluation of the parameters describing the trajectory is made.

The **track fit** is a least-square fit of the track candidates whose initial parameters are taken from the pattern recognition results. The ultimate goal is to give the best estimation of the particle momenta and positions. The fit yields the parameters \vec{q} which minimize the quadratic form:

$$\chi^2 = [\vec{d}_{meas} - \vec{d}_{\vec{q}}]^T W [\vec{d}_{meas} - \vec{d}_{\vec{q}}]$$

where \vec{d}_{meas} are the measured drift distances, $\vec{d}_{\vec{q}}$ are the distances of the closest approach of the track to each wire and W is the inverse covariance matrix of the measured coordinates. The minimization is performed using an iterative procedure in which the track model is locally linearized. Energy loss and multiple scattering suffered by particles in crossing the drift chamber are also taken in account. The track fit procedure also contains some additional features designed to increase the performance of the hit assignments using the parameters available at the track fit level, which are more refined than those available at pattern recognition level. These are:

- **Hit addition:** an ansatz is made to add hits that were not associated to any track candidate by the pattern recognition. Each hit is added or not on the basis of its contribution to the χ^2 .
- **Hit rejection:** hits associated to tracks by the pattern recognition may be removed if their contribution to the χ^2 is too large.
- **Track joining:** tries to merge two candidate tracks which could have been produced by the same particle and split by the pattern recognition.
- **Track splitting:** it operates in the opposite way if the track joining, it tries to split single tracks corresponding to two different physical signals.

3.1.3 Vertexing

After reconstructing tracks, the vertex fit [44] aims to reconstruct the positions of the decay vertexes in the DC volume.

In order to reconstruct the ϕ decay vertex tracks are extrapolated toward the nominal interaction point, taking into account the energy losses on the DC inner walls. For the other vertexes an iterative procedure is used to obtain the point of closest approach for all tracks. Pairs of tracks are searched, whose trajectories show an acceptable crossing point, both in the x - y plane and along the z coordinate. A χ^2 minimization is applied in order to obtain the best possible estimate of the vertex position, and if such procedure converges, the vertex is kept.

Vertexes are classified according to the quality of the fit. At this level, even more than one vertex can belong to a given track. A merging procedure is performed to join 2-tracks vertexes together, so obtaining vertexes with 3 or more tracks (this is particularly relevant for the $K^\pm \rightarrow \pi^\pm \pi^+ \pi^-$ decay). An hypothesis test which compares the 4-tracks vertexes versus the 2-tracks vertexes is done. On the bases of the χ^2 the two hypotheses are taped.

3.2 The background rejection filter: FILFO

The background-rejection algorithm is based on calorimeter clustering and DC hit counting, so that background events can be eliminated before DC reconstruction, which is the most CPU-intensive section of our reconstruction program. The main FILFO features are the downscaling of Bhabha and cosmic events, and machine background rejection.

For the identification of background events, cuts are applied on the number of clusters; the number of DC hits; the total energy in the calorimeter; the average polar angle, position, and depth of the (two) most energetic cluster(s); and the ratio between the number of hits in the innermost DC layers and the total number of DC hits. These cuts have been studied to minimize losses for physics channels. Additionally, a simple cut on anomalously large energy deposits in any calorimeter region is included to reject rare machine background topologies due to sporadic beam-loss events.

3.3 Event Classification: EVCL

Events surviving the rejection filters and reconstructed by means of drift chamber information are finally classified into distinct categories (data streams) by the event-selection algorithms, according to the different hypotheses for the final state.

Selection algorithms must correctly separate the various ϕ decay channels with the highest possible efficiency and minimize the contaminations from the other streams. In order to avoid correlations, the same event can be tagged by more than one algorithm and saved in different data streams. Moreover, biases are avoided by adopting rather loose and simple selection criteria. This also allows to reduce the CPU time needed for the event classification to a very small fraction with respect to the complete data reconstruction chain. The main streams defined in the event classification are, see Figure 3.2:

- $\phi \rightarrow K^+K^-$ (KPM);
- $\phi \rightarrow K_S^0K_L^0$ (KLS);
- $\phi \rightarrow \rho\pi, \pi^+\pi^-\pi^0$ (RPI);
- ϕ radiative decays (RAD);
- Bhabha and cosmic events useful for detector calibration (CLB). Also $e^+e^- \rightarrow \mu^+\mu^-$ and $e^+e^- \rightarrow \pi^+\pi^-$ events are collected within this sample;
- All events not identified by any of the EvCl algorithms (UFO);
- Bhabha scattering.

To save space on tape, only a little part of UFO events are kept, since a sizable amount of such events are unidentified Φ decays (for instance K^+K^- events in which both kaons have decayed in the interaction region without reaching the tracking volume) or machine background events.

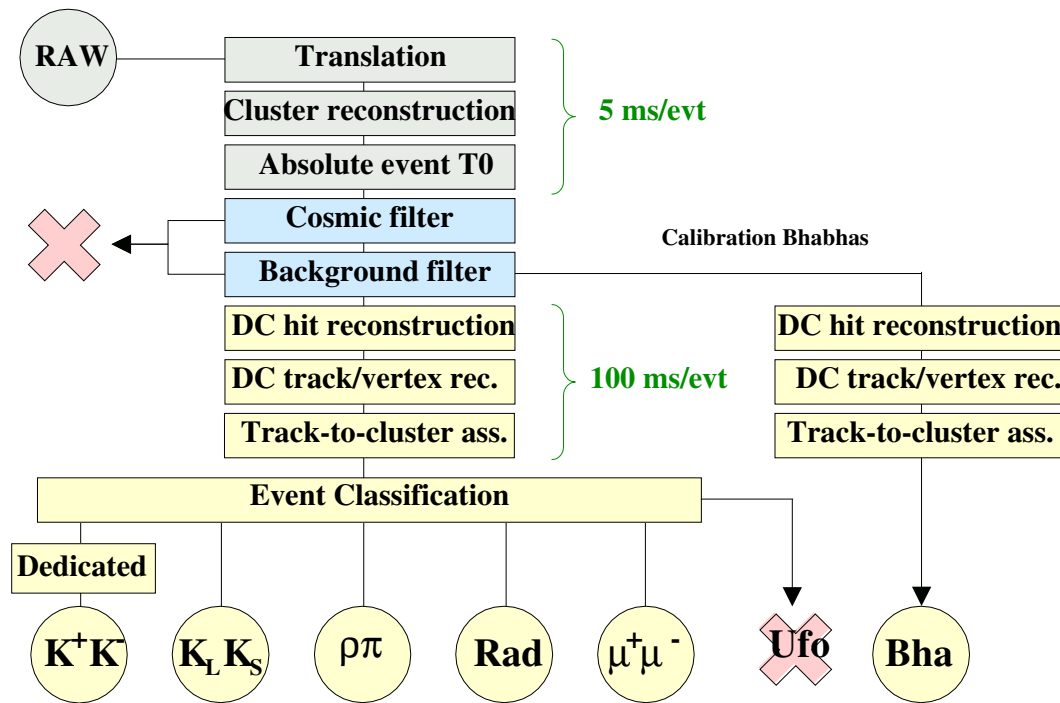


Figure 3.2: Logic scheme of the KLOE offline reconstruction.

Chapter 4

Selection of $\eta \rightarrow \pi^0 \pi^0 \pi^0$ decays

The DAΦNE collider is a ϕ -factory in which the ϕ meson is produced with a cross section of $\sim 3.1 \mu\text{b}$. Although the ϕ meson decays in the η particle with a branching fraction of [2]:

$$BR(\phi \rightarrow \eta\gamma) = (1.301 \pm 0.024)\% \quad (4.1)$$

the high statistics collected ($L = 2 \text{ fb}^{-1}$ corresponding to $7 \cdot 10^9$ ϕ mesons) allows to have $\sim 100 \cdot 10^6$ η mesons, so it is possible to regard DAΦNE as an η -factory.

Then the η decays into the searched channel $\eta \rightarrow 3\pi^0$ with [2]:

$$BR(\eta \rightarrow 3\pi^0) = (32.51 \pm 0.28)\% \quad (4.2)$$

The final state of the whole process is the production of 7γ 's, since the π^0 decays into two photons almost every time,¹ with:

$$BR_{TOT} = 4 \cdot 10^{-3}. \quad (4.3)$$

The production and decay chain has been depicted in Figure 4.1.

In this chapter the procedure of selection of $\phi \rightarrow \eta\gamma \rightarrow \pi^0 \pi^0 \pi^0 \gamma \rightarrow 7\gamma$ is presented. We will describe how the fully neutral radiative decays are identified in the RAD stream (see Section 3.3). A shortly description of the kinematic fit and the pairing photons procedure will be given.

¹ $BR(\pi^0 \rightarrow \gamma\gamma) = (98.798 \pm 0.032)\%$.

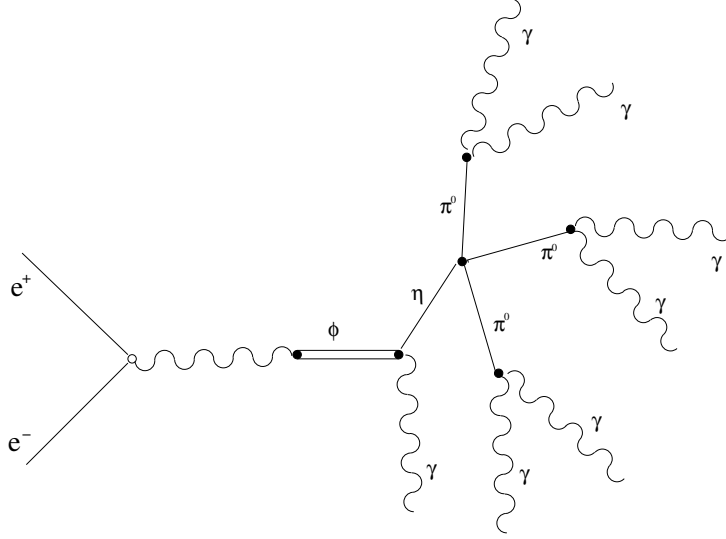


Figure 4.1: Scheme of the production mechanism of the η meson and decay chain into the $3\pi^0$ final state.

4.1 Event Classification: fully neutral radiative decays

The relevant feature of the fully neutral radiative decays is that only prompt photons are present in the final state.

Prompt means that the β^2 of all cluster is almost equal to unity, since all the photons can be assumed to be produced in the IP of DAΦNE.

In order to reduce the double-writing, these decays have to be kept separated from the most relevant ϕ non radiative fully neutral decays that are $K_L K_S \rightarrow n\pi^0$ with $n = 4, 5$ and K_L interacting in the calorimeter (the so called K_L crash events) with $K_S \rightarrow \pi^0\pi^0$. A suitable discriminant variable considered is the reconstructed energy of the most energetic cluster.

The selection can be summarized as follows:

- absence of reconstructed tracks in the drift chamber;
- total collected energy in the calorimeter $E_{tot} > 700$ MeV;
- $P_{tot}^3 > 100$;

² $\beta = \frac{r_{cl}}{cT_{cl}}$ where r_{cl} and T_{cl} are respectively the distance of the cluster centroid from the origin of the coordinates and the time of the cluster and c the light velocity. β is the velocity of the particle provided it comes from the interaction region.

³ P_{tot} is the (modulus of the) total momentum of the photons obtained summing the

- logical OR of the two following conditions:
 - at least 1 (not associated) cluster with $E_{cl} > 280$ MeV and $\langle\beta\rangle_{n_{cl}} > 0.85$;
 - number of reconstructed cluster in the calorimeter $n_{cl} > 6$ AND $\beta > 0.95$.

The efficiencies have been evaluated on Monte Carlo samples of the various channels, and they turn out to be of the order of 90% or better for the channels with less than 9 photons in the final state, while the efficiency for $K_L K_S \rightarrow anything$ is about 1.2% corresponding to a double-writing of $4 \cdot 10^{-3}$ of the collected events see Table 4.1. However the efficiency goes down to $5 \div 10\%$ for the process with 9 and 11 photons, due to the maximum energy cut.

Channel	N. of prompt γ '	Efficiency
$\pi^0\gamma$	3	0.97
$\eta\gamma \rightarrow \gamma\gamma\gamma$	3	0.97
$\eta\gamma \rightarrow \pi^0\pi^0\pi^0\gamma$	7	0.80
$\eta'\gamma \rightarrow \gamma\gamma\gamma$	3	0.95
$\eta'\gamma \rightarrow \pi^0\pi^0\gamma\gamma\gamma$	7	0.90
$\eta'\gamma \rightarrow \pi^0\pi^0\pi^0\pi^0\pi^0\gamma$	11	0.98
$f_0\gamma \rightarrow \pi^0\pi^0\gamma$	5	0.88
$\pi^0\pi^0\gamma$	5	0.88
$\rho^0\pi^0 \rightarrow \pi^0\pi^0\gamma$	5	0.89
$a_0\gamma \rightarrow \eta\pi^0\gamma \rightarrow \pi^0\gamma\gamma\gamma$	5	0.97
$a_0\gamma \rightarrow \eta\pi^0\gamma \rightarrow 4\pi^0\gamma$	9	0.88
$\eta\pi^0\gamma \rightarrow \pi^0\gamma\gamma\gamma$	5	0.94
$\eta\pi^0\gamma \rightarrow 4\pi^0\gamma$	9	0.93
$\phi \rightarrow K_S K_L \rightarrow anything$	-	0.012

Table 4.1: Number of prompt clusters and ECL filter efficiency for totally neutral radiative decays.

single photons momenta, calculated with the IP origin hypothesis

4.2 Topological selection of the $\phi \rightarrow \eta\gamma \rightarrow 7\gamma$ events

The cuts used to select the events with the expected final state signature, that is seven photons coming from the interaction region, are the following:

- 7 and only 7 prompt neutral cluster (see below) with $21^\circ < \theta_\gamma < 159^\circ$ and $E_\gamma > 10$ MeV
- Opening angle between each couple of photons $> 18^\circ$

A prompt neutral cluster is defined as a cluster in the EMC with no associated track coming from the Drift Chamber (DC) and $|(t - \frac{r}{c})| < 5\sigma_t$ where t is the arrival time on the EMC, r is the distance of the cluster from the IP and c is the speed of light and $\sigma_t = 54 \text{ ps}/\sqrt{E(\text{GeV})} \oplus 150 \text{ ps}$ [4].

The cut at 10 MeV minimum energy strongly reduces the *inefficiency* induced by a wrong cluster counting when small cluster fragments are reconstructed as a different cluster (cluster splitting). Moreover it helps scaling down soft machine background photons.

The region below 21° is excluded due to the presence of DAΦNE magnetic quadrupoles near the interaction point.

The cut on the opening angle of the photons again reduces the problem of cluster splitting. In fact the splitting affects clusters which have a small angular separation $< 15^\circ$.

The overall “common” selection efficiency (including trigger,⁴ reconstruction, event classification and topological selection) is:

$$\varepsilon = (33.14 \pm 0.01) \% \quad (4.4)$$

4.3 Kinematic fit

The selection described allows to realize the first reduction of the events but, in order to ensure a kinematic closure of the event a kinematic fit has been applied to the seven photons sample.

This significantly improves the energy resolution and allows to obtain a high

⁴The trigger efficiency is very high for this sample: $\varepsilon_{trigger} = 99\%$.

level of background suppression. The basic idea is to minimize a least square function of the type:

$$X^2 = \sum_{i=1}^N \frac{(P_i - P_i^{meas})^2}{\sigma_i^2} \quad (4.5)$$

where P_i^{meas} are the measured values for the parameters and the minimization is driven by the need to fulfill the M constraining conditions:

$$C_j(P_1 \dots P_N) = 0 \quad \forall j = 1, \dots, M \quad (4.6)$$

To perform this kind of minimization we have used the well know Lagrange multipliers procedure to find a constrained minimum for a function of N variables, minimizing with an iterative procedure the function:

$$Y^2 = \sum_{i=1}^N \frac{(P_i^k - P_i^{meas})^2}{\sigma_i^2} + \sum_{j=1}^M \lambda_j^k C_j(P_1^k \dots P_N^k) \quad (4.7)$$

where k is the iteration index and the λ_j 's are the M additional parameters (Lagrange multipliers) used to insure that the minimum is found with the $P_1 \dots P_N$ parameters lying on the hypersurface defined by the M conditions (4.6).

The starting values for the fit P_i^0 are the measured values P_i^{meas} so that in the very first iteration the first part of the Y^2 function in eq. (4.7) is strictly zero.

After minimization the X^2 variable, see eq. (4.5), is expected to be distributed as a χ^2 , if all the parameters distributions are Gaussian in shape with variance σ_i^2 .

If this is not the case (as often happens in these situations since reconstructed parameters may have long non-Gaussian tails), the distribution may have a somewhat distorted shape, and the corresponding χ^2 probability may be not a flat distribution. The number of degree of freedom for this kind of fit is [47]:

$$\begin{aligned} N_{dgf} &= (\# \text{ of measured quantities}) - [(\# \text{ of parameters}) - (\# \text{ of constraints})] \\ &= N - (N - M) \\ &= (\# \text{ of constraints}) \end{aligned}$$

since the number of measured quantities is exactly equal to the number of parameters.

The parameters used in the fit are:

- Energy, time, and position for each photon (7×3 parameters),

- Beams energies (2 parameters),

for a total of $N = 23$ parameters.

The errors on these parameters are determined as follows:

- $\frac{\sigma_E}{E} = \frac{5\%}{\sqrt{E(\text{GeV})}}$
- $\sigma_t = \frac{50 \text{ ps}}{\sqrt{E(\text{GeV})}}$
- $\sigma_{r_\perp} = 1.2 \text{ cm}$ on data and 0.85 cm on MonteCarlo, with r_\perp perpendicular component of position of the *cluster*
- $\sigma_{r_\parallel} = \frac{1.2 \text{ cm}}{\sqrt{E(\text{GeV})}}$ on data and 0.85 cm on MonteCarlo, with r_\parallel parallel component of position of the *cluster*
- $\sigma_{E^+E^-} = 0.7 \text{ MeV}$, nominal spread in the beam energy of DAΦNE.

The fit constraints, and thus the number of degrees of freedom, are 11:

- $ct_i - r_i = 0$ for each photon (7 constraints)
- energy-momentum conservation (4 constraints)

At this level of analysis no invariant mass constraint is required.

The fit procedure may be tested by looking at the invariant mass distributions before and after the fit. If the fit procedure correctly modifies the measured parameters, an improvement in the invariant mass resolution before and after the fit must be observed.

The distribution of the invariant mass⁵ of three pions system ($\pi^0\pi^0\pi^0$) before and after the kinematic fit with a gaussian fit superimposed, is show in Figure 4.2. The results of gaussian fit, before and after the kinematic fit, are respectively:

$$\langle M \rangle_{ini} = 541.2 \text{ MeV}/c^2 \quad \sigma_{ini} = 39.7 \text{ MeV}/c^2 \quad (4.8)$$

$$\langle M \rangle_{fin} = 547.6 \text{ MeV}/c^2 \quad \sigma_{fin} = 12.4 \text{ MeV}/c^2 \quad (4.9)$$

A clear improvement in the invariant mass resolution is obtained.

The visible shift in the peak value is due to an overall $1 \div 1.5\%$ miscalibration in the energy scale.

⁵The invariant mass of three pions system has been obtained after the procedure of photons pairing to the right π^0 .

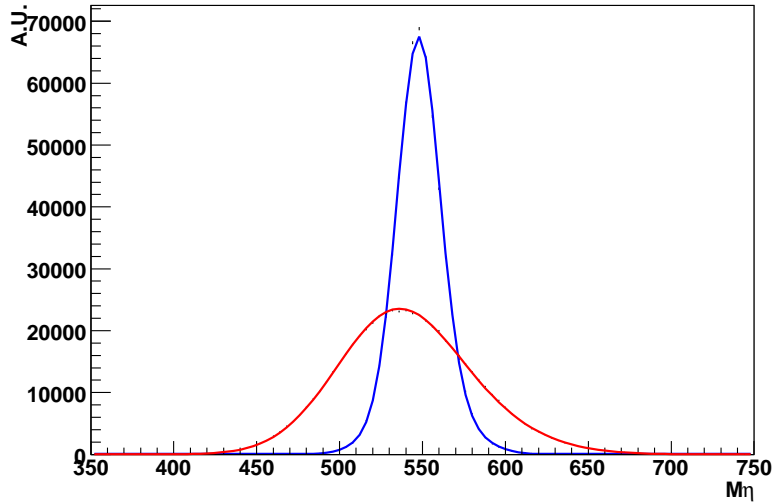


Figure 4.2: *The invariant mass of three pions system. The distribution before (red line) and after (blue line) a kinematic fit with no mass constraints are superimposed.*

In order to use the χ^2 value of the fit as a selection cut sufficiently good agreement between data and MonteCarlo χ^2 distribution should be obtained. In Figure 4.3, one can see the χ^2 distribution for data and MonteCarlo. It is seen that the behavior of the real and MonteCarlo distributions is slightly different. This shape discrepancy may be explained as due to tails of the input parameters which do not follow a Gaussian behaviour. A cut on the χ^2 probability is applied: $P_{\chi^2} > 0.01$. The efficiency of this cut is 93% leading to a final selection efficiency of $(30.73 \pm 0.01)\%$.

4.4 Photon pairing

In order to build the z variable, involved in the development of the amplitude decay (see Section 2.5), the $3\pi^0$'s energies have been know.

One of the most technical points we have to face in this analysis is the method of pairing photons to π^0 .

Before explain the pairing algorithm we note that, being the $\phi \rightarrow \eta\gamma$ a two body decay, from energy-momentum conservation one gets that the γ recoil is a monochromatic photon. Infact defining p_ϕ, p_η and p_γ the quadrimomenta

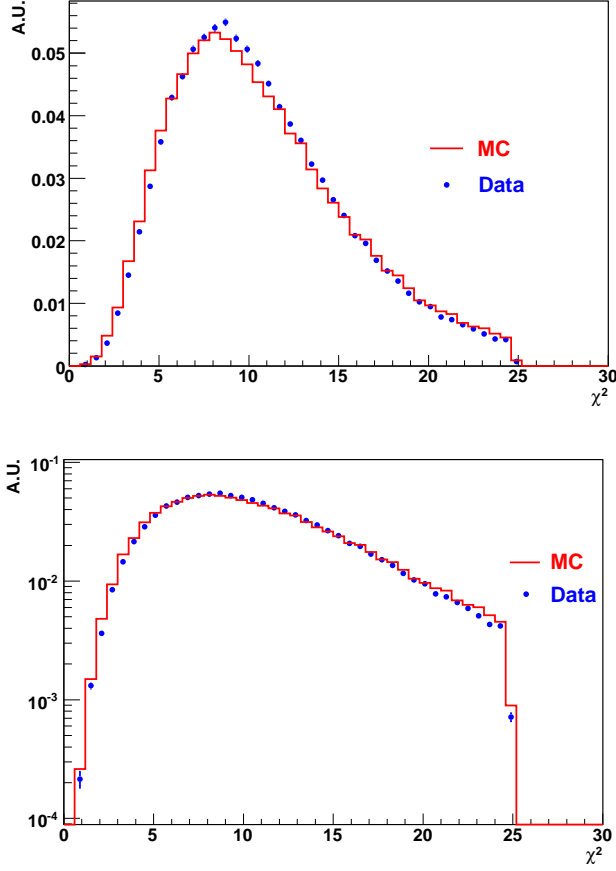


Figure 4.3: χ^2 distribution. Top: linear scale; Bottom: logarithmic scale.

of ϕ , η and γ respectively, we have:

$$p_\phi = p_\eta + p_\gamma \Leftrightarrow p_\eta^2 = (p_\phi - p_\gamma)^2 \Leftrightarrow m_\eta^2 = m_\phi^2 - 2 \cdot m_\phi E_\gamma \Leftrightarrow E_\gamma = \frac{1}{2} \left(m_\phi - \frac{m_\eta^2}{m_\phi} \right)$$

where E_γ is evaluated in the ϕ rest-frame. Using the values $m_\phi = 1019.460 \pm 0.019$ MeV/ c^2 , $m_\eta = 547.51 \pm 0.18$ MeV/ c^2 [2] one obtains $E_\gamma = 362.71 \pm 0.09$ MeV. In Figure 4.4 the energy spectrum of the photons is reported.

It is evident that the recoil photon γ_{rec} is very well separated from the others, moreover it is the hardest one; so we identify the γ_{rec} with the most energetic cluster.

An additional cut on the energy of recoil photon (after kinematic fit) is applied:

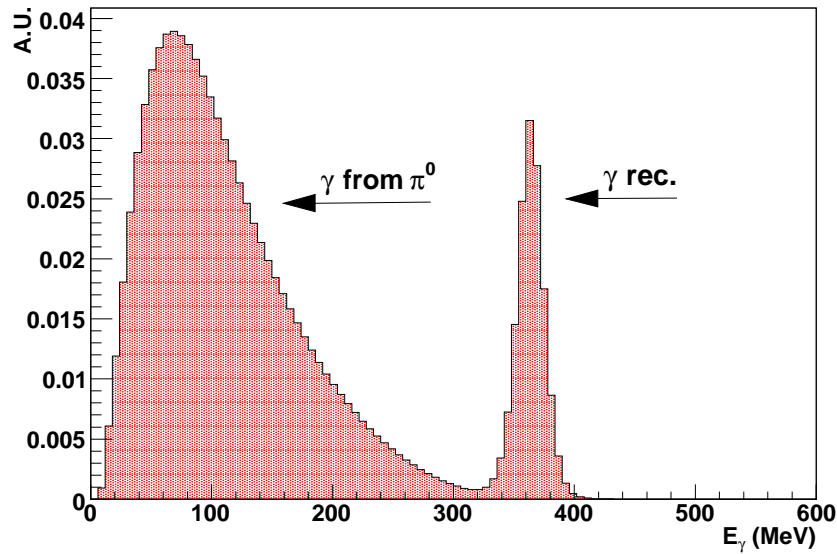


Figure 4.4: *MonteCarlo photon energy spectrum.*

$$320 < E_{\gamma_{rec}} < 400 \text{ MeV} \quad (4.10)$$

Now we have 6 photons that can make 3 pairs in 15 different ways (combinations).

Using the output of the kinematic fit, we studied by MonteCarlo the photon energy resolution. The dependence of this resolution as function of the photon energy, is reported in Figure 4.5.

A good reproduction of the data is obtained with the following function, with four free parameters:

$$\frac{\sigma_E}{E} = P_0 \left(1 - e^{-\frac{P_1}{E}} + \frac{P_2}{E} + \frac{P_3}{\sqrt{E}} \right) \quad (4.11)$$

where E is in GeV. The parameter values are reported in Figure 4.5.

The π^0 mass resolution is then parametrized as function of the quadratic sum of the photon energy resolution:

$$\frac{\sigma_{M_{\pi^0}}}{M_{\pi^0}} = \frac{1}{2} \left(\frac{\sigma_{E_1}}{E_1} \oplus \frac{\sigma_{E_2}}{E_2} \right) \quad (4.12)$$

In order to match every couple of photons to the right π^0 we build a pseudo- χ^2 variable for each of the 15 combinations:

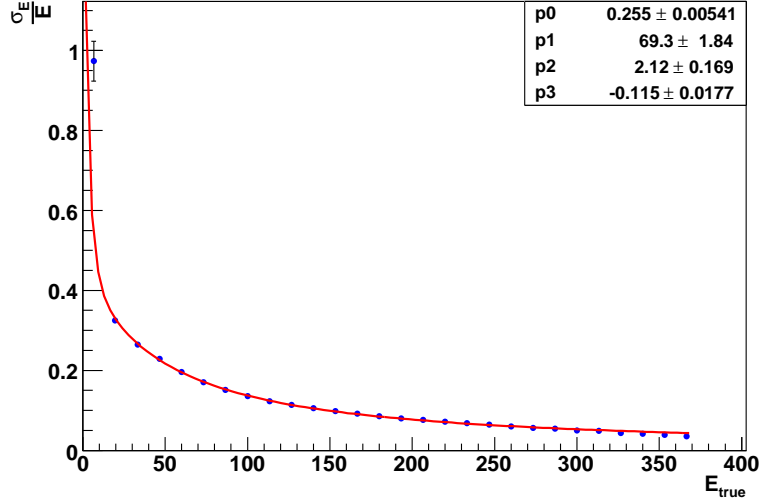


Figure 4.5: Energy resolution for photons. The straight lines represents the result of fit with the function: $\frac{\sigma_E}{E} = P_0 \left(1 - e^{-\frac{P_1}{E}} + \frac{P_2}{E} + \frac{P_3}{\sqrt{E}} \right)$.

$$\chi_j^2 = \sum_{i=1}^3 \left(\frac{m_{j,\pi_i^0} - M_{\pi^0}}{\sigma_{m_{\pi^0}}} \right)^2 \quad j = 1, 2, \dots, 15. \quad (4.13)$$

where

- m_{j,π_i^0} is the invariant mass of the $i^{th} \pi^0$, in correspondence of the j^{th} combination;
- M_{π^0} is the π^0 mass, ($M_{\pi^0} = 134.98 \text{ MeV}/c^2$ [2]);
- $\sigma_{m_{\pi^0}}$ is obtained for each combination as in the eq. (4.11).

The photon combination where the six photons of the event minimize the pseudo- χ^2 , χ_{min}^2 , is selected as the good one. In the following we have arranged the χ^2 values in decreasing way therefore:

$$\chi_{min}^2 = \chi_0^2 \quad (4.14)$$

and the next values correspond respectively to $\chi_1^2, \chi_2^2, \dots, \chi_{15}^2$.

To understand how well this algorithm works we have defined a variable ζ , such that:

- $\zeta = 0$ when the right combination is in correspondence of χ_{min}^2 , that is:

$$\chi^2 = \chi_0^2$$

- $\zeta = 1, 2, \dots, 15$ when the right combination is in correspondence of χ_1^2 and next χ^2 values,
- $\zeta = -1$ when the algorithm fails,
- $\zeta = -2$ when the radiative photon is not correctly identified.

If we define the purity as the fraction of events with all photons correctly matched to π^0 's and the efficiency as the ratio between the number of events selected and reconstructed and those generated, we found respectively:

$$P = 75.4\% \quad (4.15)$$

$$\varepsilon = 30.3\% \quad (4.16)$$

In Figure 4.6 the distribution of ζ variable is reported.

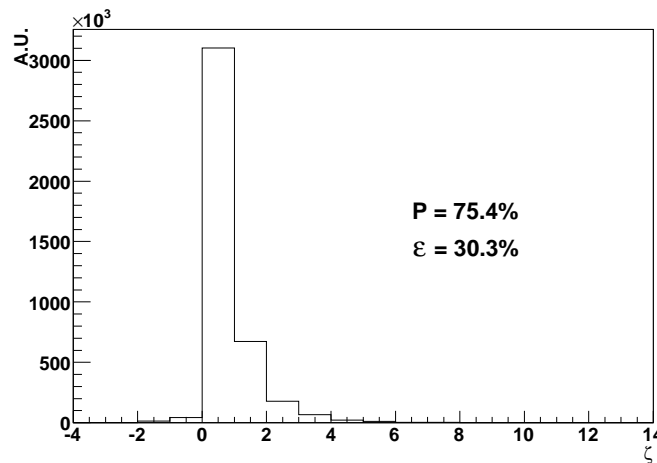


Figure 4.6: ζ distribution after the selection procedure.

In the evaluation of χ^2 , the parameters obtained by MonteCarlo (see Figure 4.5) are used also for data.

To improve the purity an additional selection has been done. The minimum value, χ_0^2 , and the difference of the two lowest value for pseudo- χ^2 , Δ_{χ^2} , are used. The Figures 4.7 and 4.8 show the χ_0^2 and Δ_{χ^2} distributions for the right (straight line) and wrong (dashed line) combination.

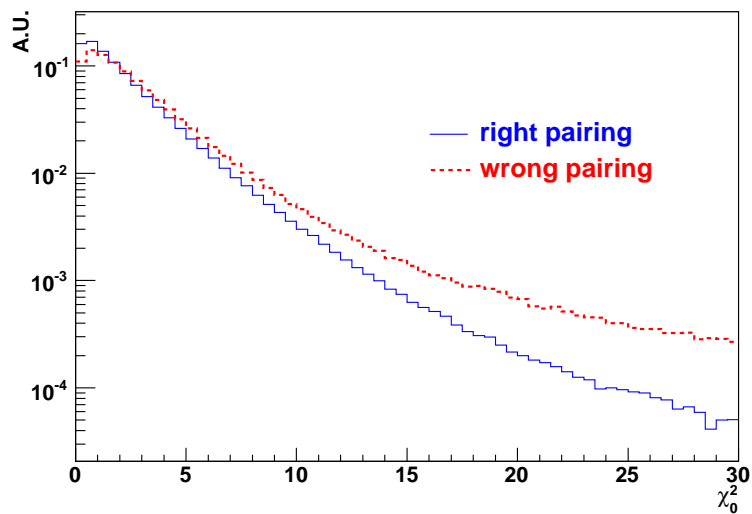


Figure 4.7: χ_0^2 shapes for events with right (straight line) and wrong (dotted line) photon pairing.

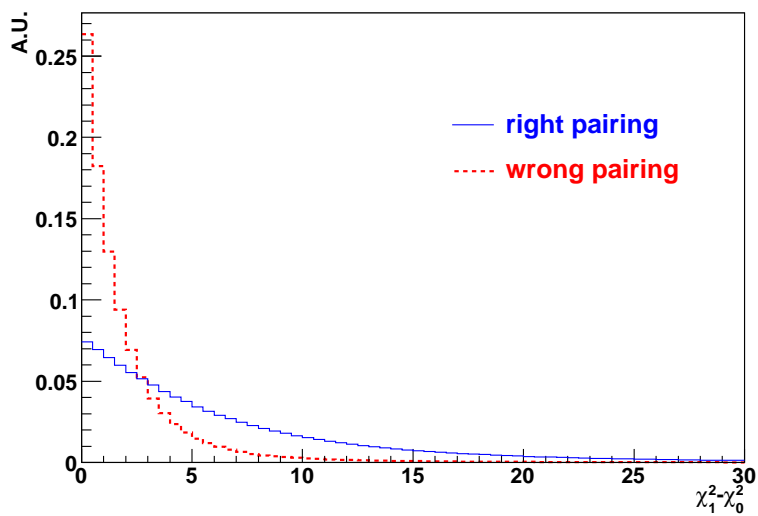


Figure 4.8: Distribution of the difference between the best and second best combination $\Delta\chi^2$, for events with right (straight line) and wrong (dotted line) photon pairing.

We use Δ_{χ^2} because, if it is true that the right combination has a better χ^2 value of the others ($\chi_0^2 \ll \chi_1^2, \dots, \chi_{15}^2$) there aren't no physical motivations to expect that the wrong combination has a better χ^2 value of the others, see Figure 4.8.

Moving the position of the cuts on these variables we can obtain samples with different purity-efficiency:

$$P = 84.5\% \qquad \varepsilon = 22\% \qquad (4.17)$$

$$P = 92.0\% \qquad \varepsilon = 13.6\% \qquad (4.18)$$

$$P = 94.8\% \qquad \varepsilon = 9.2\% \qquad (4.19)$$

$$P = 97.6\% \qquad \varepsilon = 4.3\% \qquad (4.20)$$

For each sample, in Figure 4.9 the distribution of ζ variable is reported. In the following we will use these four samples and we refer to these respectively as: “Low Purity”, “Medium Purity I”, “Medium Purity II”, “High Purity”.

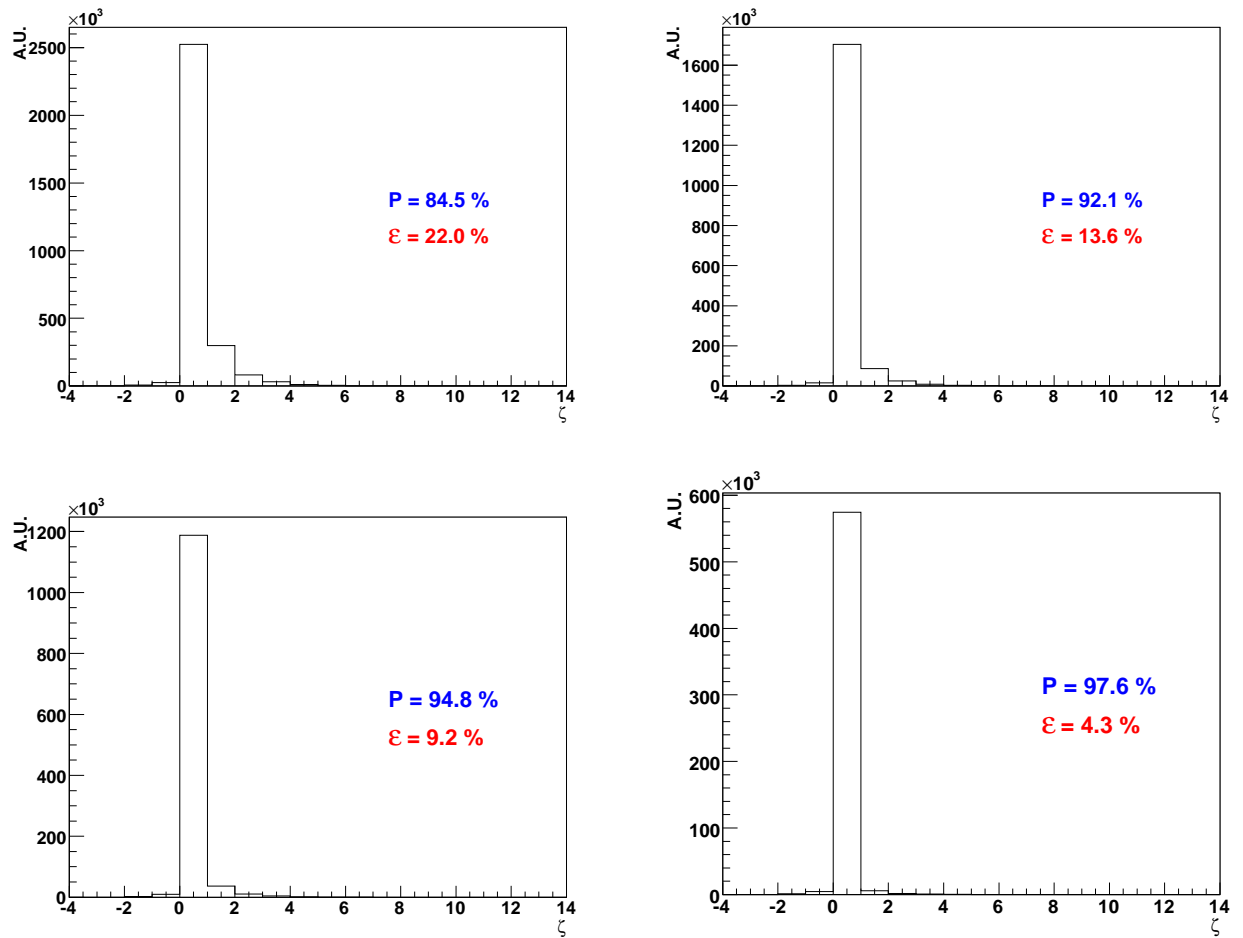


Figure 4.9: From top left in clockwise direction: reconstructed z variable for Low, Medium I, Medium II, High purity samples.

Chapter 5

Analysis

We report on a measurement of the slope parameter α which describes the energy dependence of the square of the matrix element for the $A(\eta \rightarrow 3\pi^0)$ transition amplitude.

The value of α is measured using about 250000 reconstructed $\eta \rightarrow 3\pi^0$ events. In the first part of the chapter a detail study on MonteCarlo is described. The result on data and the systematic evaluation are presented in the second part of the chapter.

5.1 Resolution and efficiency

As we have seen (see Section 2.5) the square of the transition amplitude matrix element $M = A(\eta \rightarrow 3\pi^0)$ can be parameterized as follow

$$|M|^2 \sim 1 + 2\alpha z \quad (5.1)$$

with:

$$z = \frac{2}{3} \sum_{i=1}^3 \left(\frac{3E_i - m_\eta}{m_\eta - 3m_{\pi^0}} \right)^2 = \frac{\rho^2}{\rho_{max}^2}. \quad (5.2)$$

Here E_i is the energy of the pion i in the η rest frame and ρ gives the distance from a point on the Dalitz plot to the center; ρ_{max} is the maximum value of ρ . Distributions shown in Figure 5.1 are two Dalitz-plot representation for pure phase space $\eta \rightarrow 3\pi^0$ decay.

The z distribution varies from 0, when all three π^0 's have the same energy ($E_i = M_\eta/3$), to 1, when one π^0 is at rest and others two are back to back.

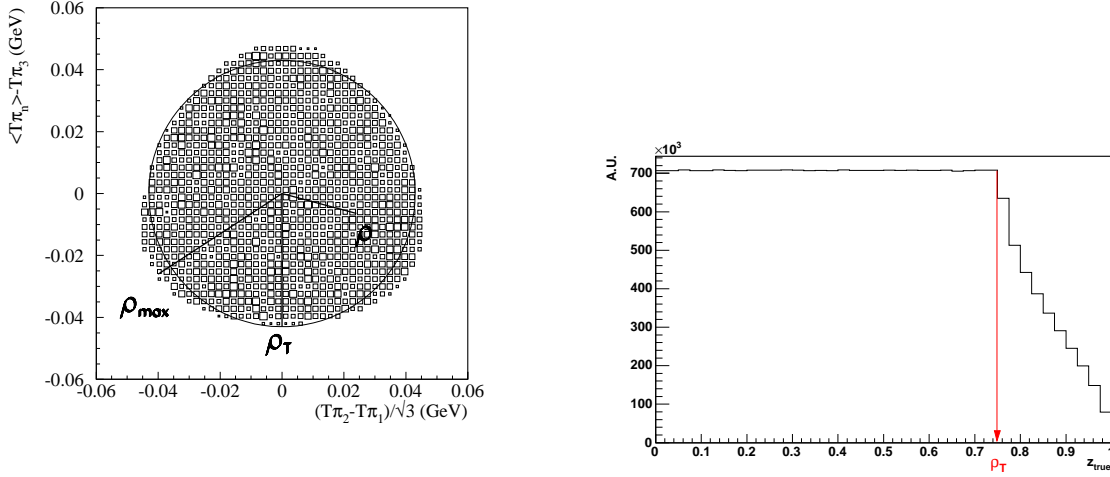


Figure 5.1: Dalitz plot for pure phase space $\eta \rightarrow 3\pi^0$ decay. Left: in variables of kinetic energies of decay product (where T_{π_i} and $\langle T_\pi \rangle$ are kinetic energy of each pion i and mean kinetic energy of three π^0 , respectively, in the η rest frame). Right: the distribution $z = \frac{\rho^2}{\rho_{max}^2}$.

This distribution is flat up to a value of z which corresponds to events inside the circle of radius ρ_T (shown in Figure 5.1), decreasing to zero for events outside this circle.

To obtain the pion energy in the η -rest frame we use for each π^0 , the measured quadrimomenta of the photons from π^0 decay:

$$P_{\pi^0}^\mu = P_\gamma^\mu + P_\gamma^\mu \quad (5.3)$$

and then we boost in the η -rest frame ($\beta = \frac{\vec{p}_\eta}{E_\eta}$).¹

For the MonteCarlo sample we use the 2001 ÷ 2002 KLOE production for the neutral radiative stream, whose integrated luminosity is five times the collected data for all the signal and background: $2.4 \cdot 10^7 \eta \rightarrow 3\pi^0$ decays.

For each sample with different purity-efficiency (see Section 4.4), the z distribution after all the analysis cuts and the resolution on z are shown in Figure 5.2. Since z assumes only positive values, the resolution does not follow a gaussian behaviour. Moreover as we expected, as the z distribution

¹From energy-momentum conservation in the $\phi \rightarrow \eta\gamma$ decay: $P_\eta^\mu = P_\phi^\mu - P_{\gamma_{rec}}^\mu$ with P_ϕ^μ and $P_{\gamma_{rec}}^\mu$ the quadrimomenta of ϕ and the recoil photon respectively.

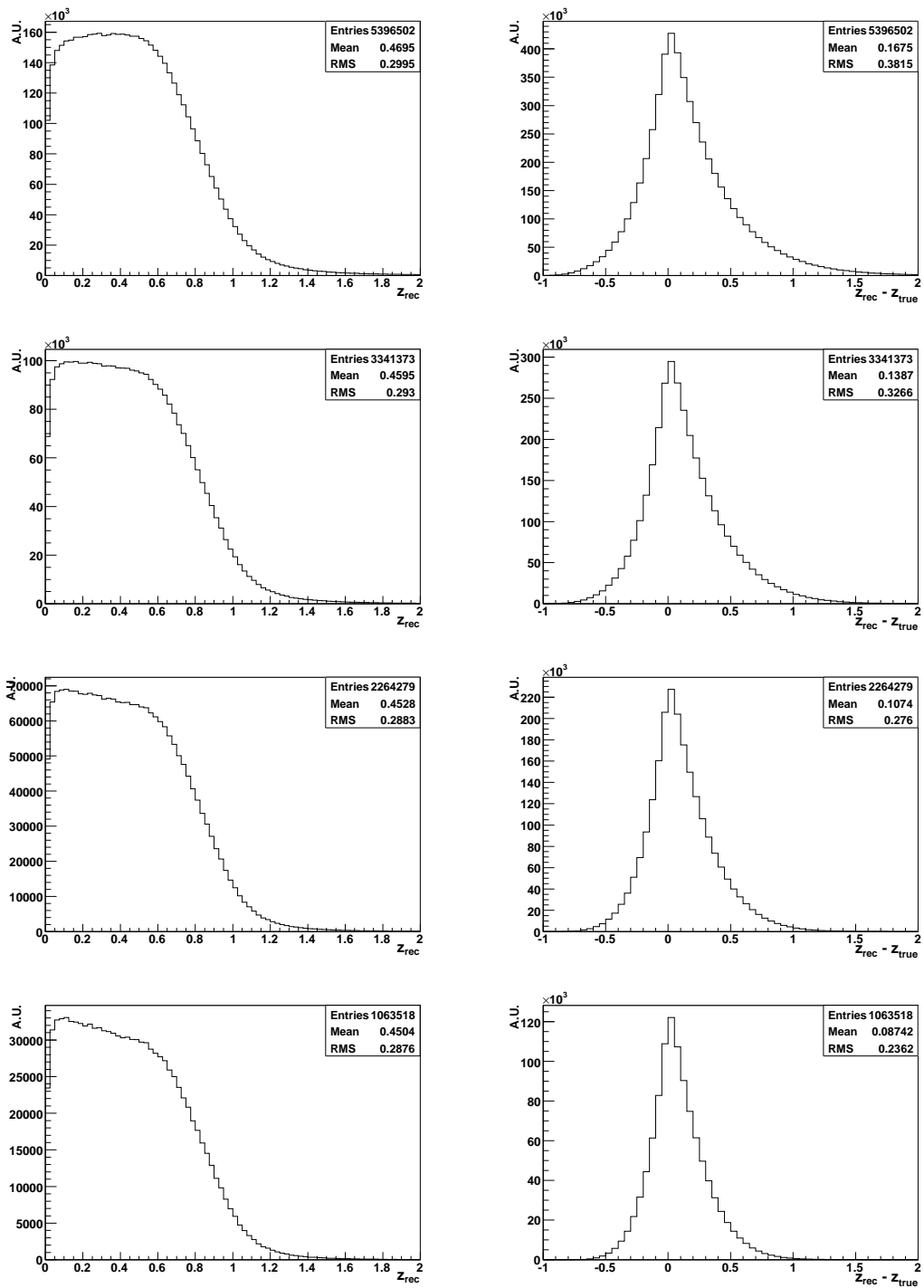


Figure 5.2: *Left: z distribution after selection and reconstruction. Right: the resolution on z . From top to bottom: Low, Medium I, Medium II, High purity samples.*

is extended beyond the pure phase space, the resolution is rather limited and consequently we do not have enough bins in the z distribution histogram. As result, it is not possible to use a straight line fit of the ratio of z distributions for real data and MonteCarlo to measure the slope parameter α .

A dependence on purity is also present: the resolution improves to increasing of the purity. In order to improve the resolution we perform a second kinematic fit which imposes the mass of the three pions. This fit proceeds after the photons pairing procedure. We obtain an improvement in the z resolution of a factor two (i.e. for High purity sample: from RMS ~ 0.236 to RMS ~ 0.128) but again it is not sufficient to have enough bins in the z distribution histograms, see Figure 5.3. As we will see, the fit of Dalitz plot procedure (see Section 5.2) takes into account the resolution effects and it is totally binning independent.

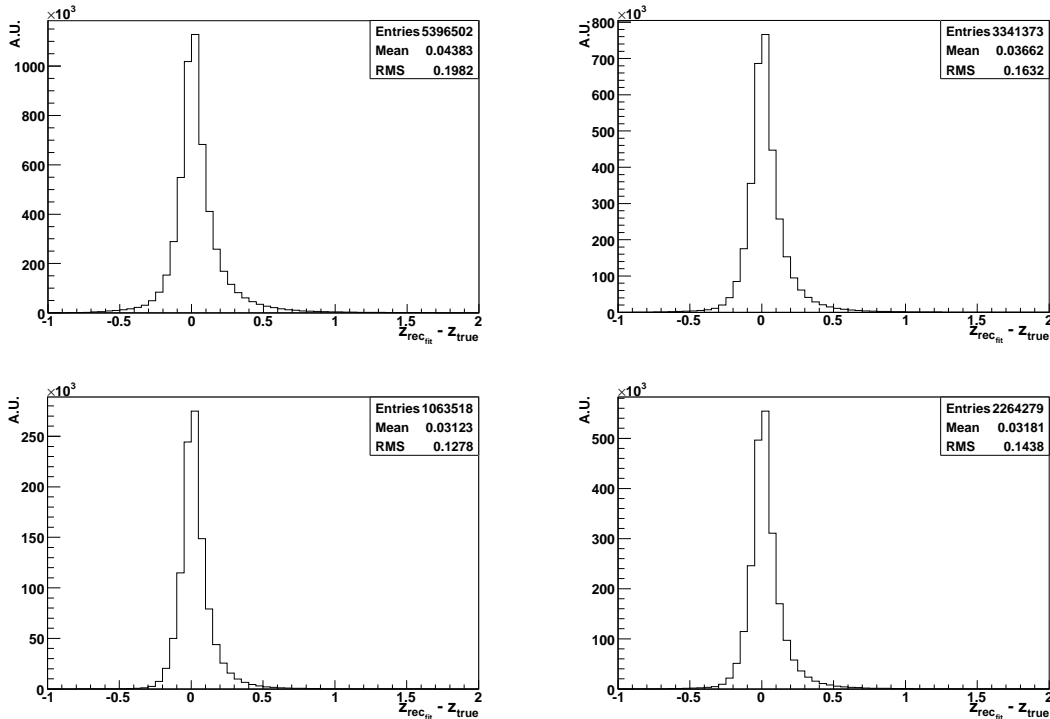


Figure 5.3: From top left in clockwise direction: the resolution of the z variable after the second kinematic fit for Low, Medium I, Medium II, High purity samples.

The efficiency as function of z is extracted from MonteCarlo: for each bin, it is defined as the ratio between the number of generated MC events, N_{gen} ,

and the number of selected MC decays in any bin, N_{rec} :

$$\varepsilon(z) = \frac{N_{rec}}{N_{gen}} \quad (5.4)$$

The estimated selection efficiencies are:

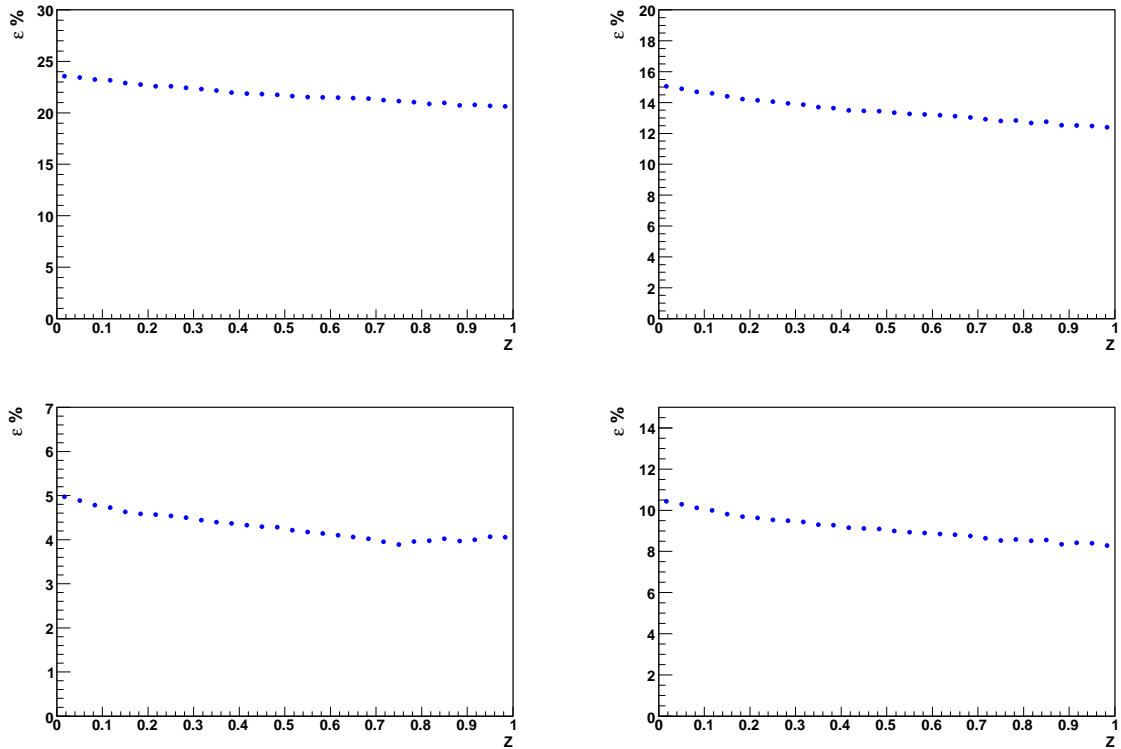


Figure 5.4: From top left in clockwise direction: the efficiency as function of z variable for Low, Medium I, Medium II, High purity samples.

Low Purity	$\langle \varepsilon \rangle = (22.02 \pm 0.01)\%$
Medium Purity I	$\langle \varepsilon \rangle = (13.64 \pm 0.01)\%$
MediumPurity II	$\langle \varepsilon \rangle = (9.24 \pm 0.01)\%$
High Purity	$\langle \varepsilon \rangle = (4.34 \pm 0.01)\%$

In Figure 5.4, the efficiency as function of z is plotted.

We notice a greater slope in the efficiency shapes to increasing of the purity: the maximum spread observed is 26%, 25%, 21%, 14% respectively for High,

Medium II, Medium I, Low purity samples. The systematic connected to the detection efficiency will be analyzed comparing the fit results for the different samples.

5.2 Fit of Dalitz-plot procedure

In order to estimate the value of the parameter α we use the Maximum Likelihood approach. This method is very general and powerful in all problems of parameter estimation where the functional form of the p.d.f. is given.

Let $f(z, \alpha)$ the p.d.f. with an unknown parameter α to be estimated from the set of observations (z_1, z_2, \dots, z_n) ; the likelihood function is:

$$\mathcal{L}(\bar{z}|\alpha) = \prod_{i=1}^n f(z_i|\alpha). \quad (5.5)$$

According to the Maximum-Likelihood Principle we should choose as an estimate of the unknown parameter α that particular $\hat{\alpha}$ which maximizes the likelihood function. Since \mathcal{L} and $\log \mathcal{L}$ attain their maxima for the same value of α we search $\hat{\alpha}$ minimizing the log-Likelihood function:

$$-\log \mathcal{L}(\bar{z}|\alpha) = -\sum_{i=1}^n \log(f(z_i|\alpha)). \quad (5.6)$$

When the number of observations is very large the numerical evaluation of the likelihood function is quite laborious. In such situation one may reduce the amount of computation by making a histogram, yielding a certain number of entries $n = (n_1, n_2, \dots, n_N)$ in N bins. In Appendix A the maximum likelihood method is explained in more details. Now the log-Likelihood function to minimize becomes:

$$\log \mathcal{L}(\alpha) = \sum_{i=1}^N n_i \log \nu_i(\alpha), \quad (5.7)$$

where, for each bin

- n_i are the number of reconstructed events,
- ν_i are the entries in a MonteCarlo histogram built as follows:
for each MonteCarlo event (according pure phase space)

- . evaluate its z_{true} and its z_{rec} (if any!)
- . enter an histogram with the value of z_{rec}
- . weight the entry with $f_{true}^{th}(z_{true}; \alpha) = 1 + 2\alpha z_{true}$

The terms independent of α have been neglected in the eq. (5.7). Note that we use the events one at time, and so, even if we have histograms, we are independent of the bin size choice. Infact the procedure automatically takes into account the resolution and efficiency effect in the unbinned way. The fit procedure is performed by means of [48].

5.2.1 Testing of goodness of fit

While the principle of maximum likelihood provides a method to estimate parameters, it does not directly suggest a method of testing goodness of fit. One possibility is to use the value of the likelihood function at its maximum, \mathcal{L}_{\max} , as goodness of fit statistic. This is not simple, another approach is to construct a goodness of fit statistic, see Appendix A. In particular, for Poisson distributed data, the statistic:

$$\chi^2 = 2 \sum_{i=1}^N n_i \ln \frac{n_i}{\nu_i} \quad (5.8)$$

follows a χ^2 distribution for N-1 degrees of freedom.

In the following of this analysis we use eq. (5.8) both for constructing an estimator of α as well as for testing goodness of fit. Note that the number of degrees of freedom, ndf , is:

$$ndf = N_{bin}^{fitted} - 1$$

where N_{bin}^{fitted} are the numbers of bin fitted in the z distribution histogram.

5.3 Analysis on MonteCarlo

The fit of Dalitz plot procedure has been tested on a MonteCarlo sample generated according to pure phase space. The slope parameter α for the simulation is $\alpha = 0$.

For each of the four samples we find:

$\alpha = 0.0002 \pm 0.0021$	Low purity
$\alpha = 0.0008 \pm 0.0026$	Medium purity I
$\alpha = 0.0022 \pm 0.0030$	Medium purity II
$\alpha = 0.0029 \pm 0.0044$	High purity

It is evident that the fitting procedure allows to find correctly the MonteCarlo input parameter independently from the purity of sample.

We have fitted using different ranges:

1. (0 – 0.6) and (0 – 0.7) corresponding to the regions in which z distribution is flat,
2. (0 – 0.8) corresponding to the region in which the z distribution begins to decrease,
3. (0 – 1) corresponding to the allowed region of the phase space.

In these ranges the N_{bin}^{fitted} are respectively 15, 18, 20 and 25. In order to estimate the sensibility and the possible distorsions introduced by the fit procedure we have defined samples with different values of the parameter:

$$\alpha = -0.06, -0.04, -0.02, 0., 0.02, 0.04, 0.06$$

and we have looked at the result of our fit for these samples.

In Figures 5.5 and 5.6 the different evaluations obtained, $\hat{\alpha}$, are plotted with the linear fit superimposed.

No appreciable distorsion in the α evaluation is present. However, for each sample with different purity and in the different fit ranges we use the results of linear fit to correct the value of α parameter on data.

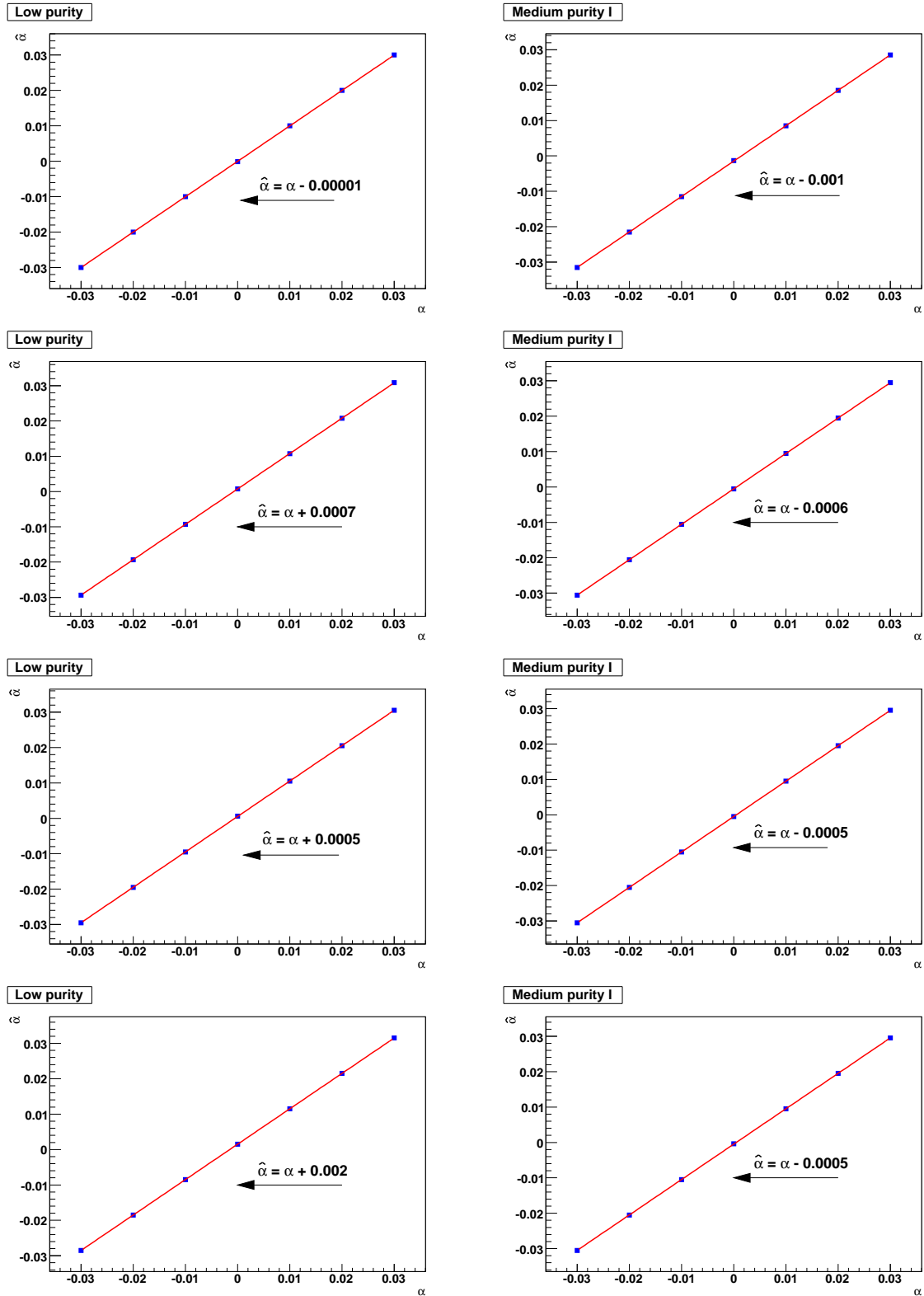


Figure 5.5: Results of the fit to the Dalitz plot on MonteCarlo for different values of α in input. From top to bottom: the results in the ranges $(0 - 1)$, $(0 - 0.8)$, $(0 - 0.7)$ and $(0 - 0.6)$. Left: Low purity sample. Right: Medium I purity sample.

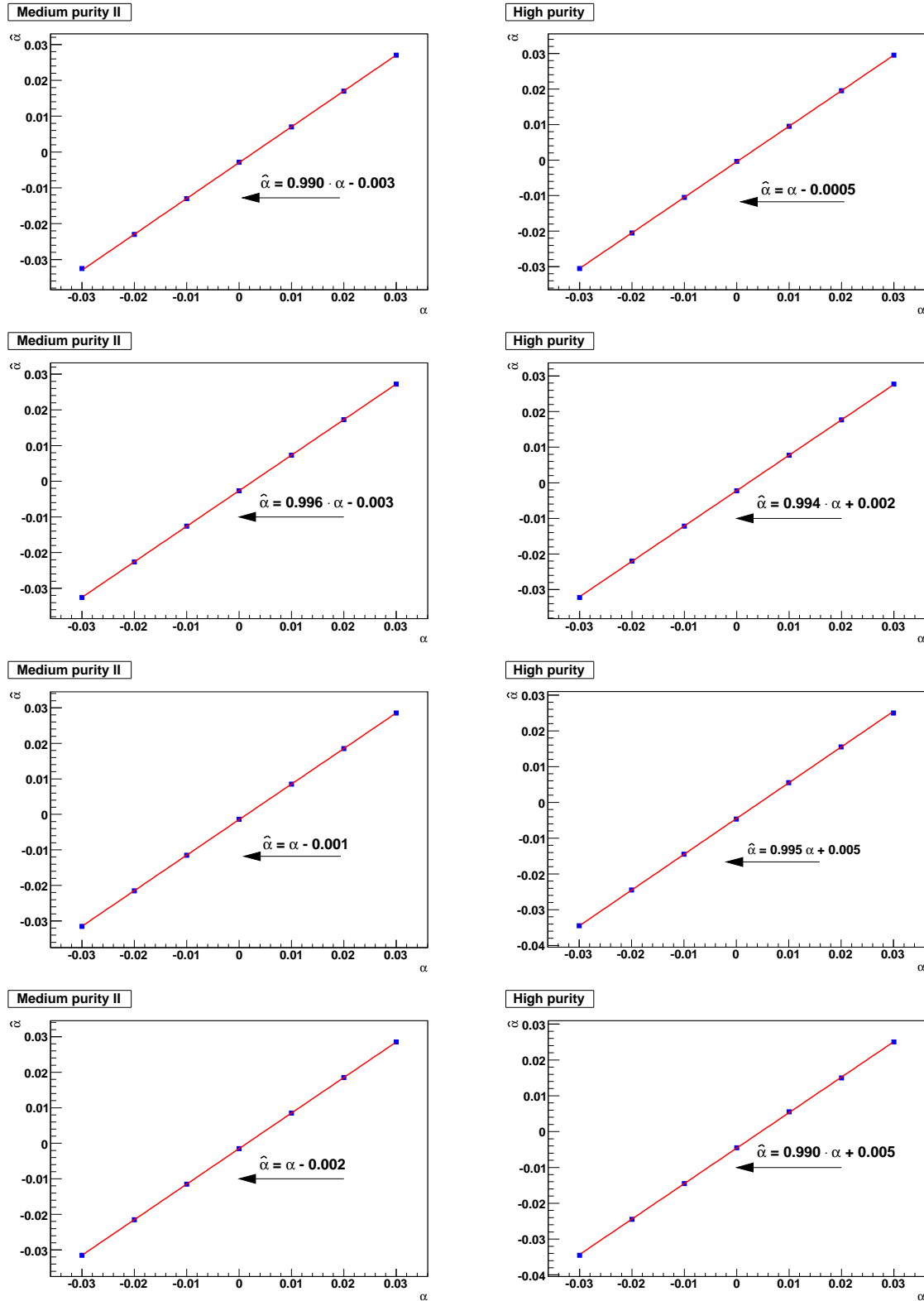


Figure 5.6: Results of the fit to the Dalitz plot on MonteCarlo for different values of α in input. From top to bottom: the results in the ranges $(0 - 1)$, $(0 - 0.8)$, $(0 - 0.7)$ and $(0 - 0.6)$. Left: MediumII purity sample. Right: High purity sample.

5.4 Data sample

We report the measurement of the slope parameter α for the $\eta \rightarrow 3\pi^0$ decay performed using $L_{int} = 418 \text{ pb}^{-1}$ of e^+e^- collisions collected in the 2001–2002 data taking period.

Note that the luminosity measurement, L_{int} , has been obtained using the Very Large Angle Bhabha (VLAB) sample [49].

The number of events in the Dalitz plot is:

$N_1 = 1.2082 \pm 0.0011 \text{ Mevts}$	Low purity
$N_2 = 0.7589 \pm 0.0009 \text{ Mevts}$	Medium purity I
$N_3 = 0.5233 \pm 0.0007 \text{ Mevts}$	Medium purity II
$N_4 = 0.2498 \pm 0.0005 \text{ Mevts}$	High purity

The distribution of the z variable obtained from the different samples of the real data is shown in Figure 5.7.

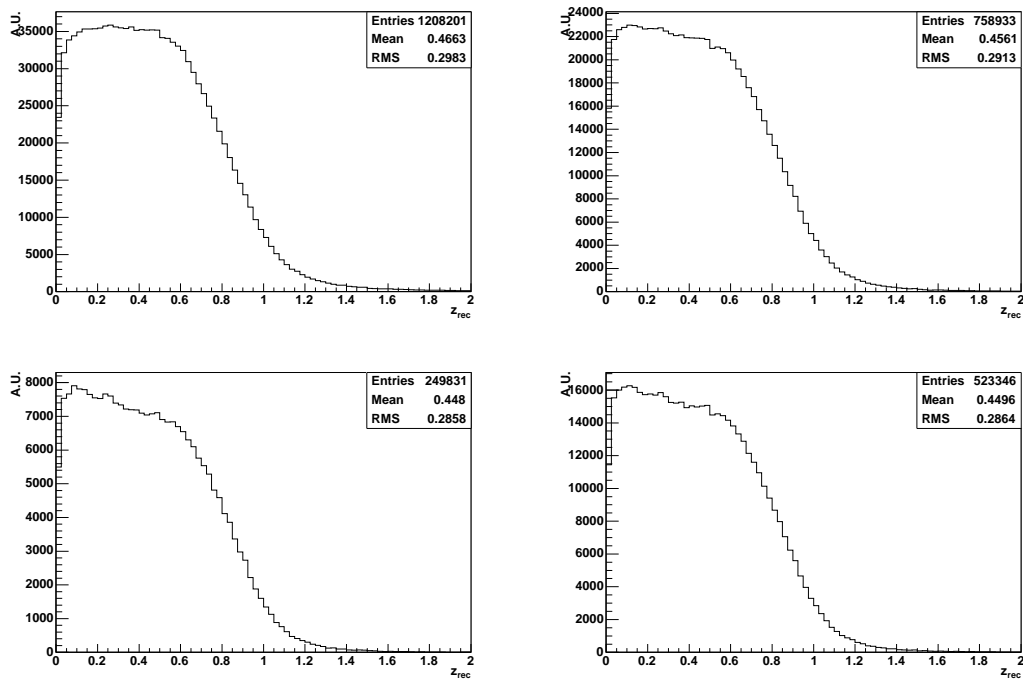


Figure 5.7: From top left in clockwise direction: the z distribution on data for Low, Medium I, Medium II, High purity samples.

5.5 Analysis on data

The procedure of fit described in Section 5.2 and successfully tested on MonteCarlo has been applied on the four data samples.

In Table 5.1, the results for the fit ranges $(0 - 1)$ and $(0 - 0.7)$ are reported. In the following the fitted parameter values has been corrected for the bias introduced by the fit procedure, see Section 5.3.

Range	Low Pur.	Medium Pur. I	Medium Pur. II	High Pur.
(0,1)	-0.018 ± 0.002	-0.018 ± 0.003	-0.011 ± 0.003	-0.008 ± 0.004
(0,0.7)	-0.030 ± 0.003	-0.026 ± 0.003	-0.018 ± 0.004	-0.018 ± 0.006

Table 5.1: Results of fit to Dalitz plot for different purity samples. For each sample, the slope parameter α has been evaluated in the fit range $(0, 1)$ and $(0, 0.7)$.

The fitted parameter value depends on the purity sample, and comparing the results in the two different ranges a systematic shift is observed. The two ranges, due to the presence of the contour of Dalitz plot, are sensitive to the parametrization of the phase space.

To better understand this problem, we observe that the value of invariant mass of three pions system ($\pi^0\pi^0\pi^0$) used on MonteCarlo, $M_\eta = 547, 30$ MeV, differs with respect to the one recently measured on real data [50]

$$M_\eta = 547.822 \pm 0.005_{stat} \pm 0.069_{syst} \text{MeV} \quad (5.9)$$

consequently, we have an accessible phase space on data greater than the one on MonteCarlo simulation, see Figure 5.8. In the plot the effect on the phase due to the different value of the η mass has been overdrawn.

In order to point out how this discrepancy affects the slope parameter α , we developed a MonteCarlo simulation to produce two dedicated samples of 300000 $\eta \rightarrow 3\pi^0$ decays, generated according to the following hypothesis:

1. $M_\eta = 547.30$ MeV
2. $M_\eta = 547.822$ MeV

The Dalitz plot variable z depends on the M_η value

$$z = \frac{2}{3} \sum_{i=1}^3 \left(\frac{3E_i - m_\eta}{m_\eta - 3m_{\pi^0}} \right)^2 \quad (5.10)$$

we use the dedicated MonteCarlo production to build three different Dalitz plot:

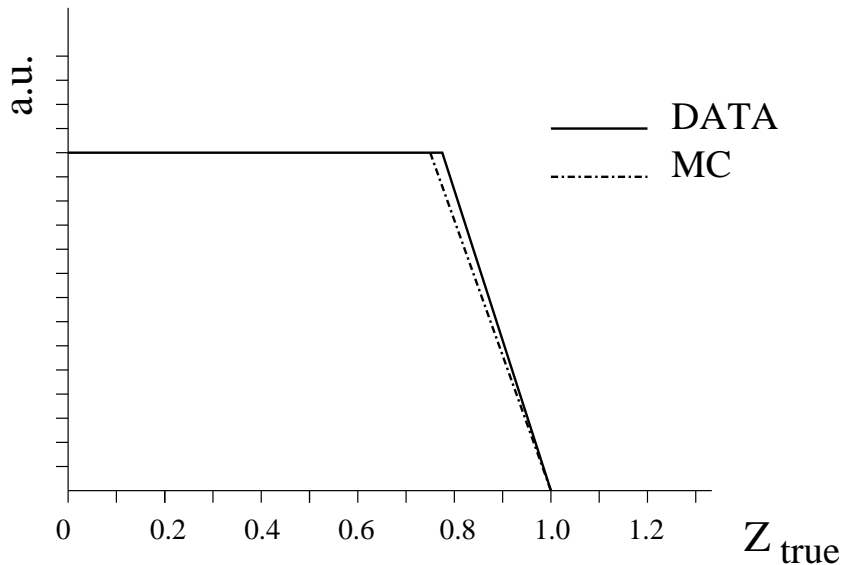


Figure 5.8: Data MonteCarlo comparison of the Dalitz plot density distribution for the $\eta \rightarrow 3\pi^0$ decay. The effect on the phase due to the different value of the η mass has been overdrawn.

- Z_{MC} is obtained from the sample 1 using the numerical value $M_\eta = 547.30$ MeV in the eq. (5.10) to build the z variable starting from the observed pion energies;
- Z_{Data} is obtained from the sample 2 using the numerical value $M_\eta = 547.30$ MeV in the eq. (5.10) to build the z variable starting from the observed pion energies;
- Z'_{Data} is obtained from the sample 2 using the numerical value $M_\eta = 547.30$ MeV in the eq. (5.10) to build the z variable starting from the observed pion energies.

The first two Dalitz plot reproduce respectively the standard MonteCarlo and the data as we handle till now; while the third, Z'_{data} , takes into account the shift in the η mass value.

As we foresee, the Z_{data}/Z_{MC} ratio evidences an excess of events on data in the range $(0.7 - 1)$; while the Z'_{data}/Z_{MC} ratio is flat in all the range, as you can see in Figure 5.9.

Consequently, the right parametrization of the Dalitz plot variable is Z'_{data} . In the following the fit to the slope parameter will be done using on data the value $M_\eta = 547.822$ MeV.

In Table 5.2 the new valuations of the Dalitz plot parameter α , are reported.

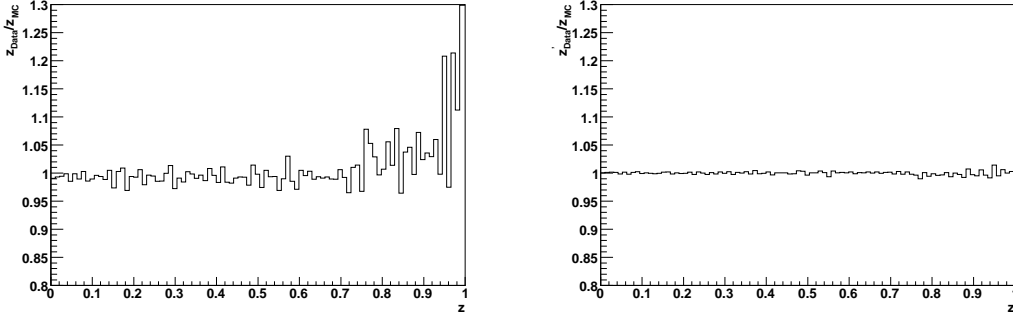


Figure 5.9: *Distribution of Z_{data}/Z_{MC} (left) and Z'_{data}/Z_{MC} (right).*

The new approach recovers the systematic shift between the two fit range,

Range	Low Pur.	Medium Pur. I	Medium Pur. II	High Pur.
(0,1)	-0.035 ± 0.002	-0.033 ± 0.003	-0.028 ± 0.003	-0.025 ± 0.004
(0,0.8)	-0.035 ± 0.003	-0.032 ± 0.003	-0.025 ± 0.004	-0.021 ± 0.005
(0,0.7)	-0.035 ± 0.003	-0.032 ± 0.004	-0.026 ± 0.004	-0.025 ± 0.006
(0,0.6)	-0.038 ± 0.004	-0.035 ± 0.004	-0.025 ± 0.005	-0.024 ± 0.008

Table 5.2: *Fitted results for the slope parameter α . The results refer to a value of η mass on data: $M_\eta = 547.822$ MeV.*

(0, 0.7) and (0, 1). To display how the η mass value affects the slope parameter α , we have shown, for the sample with low purity in Figure 5.10 a straight-line fit of the ratio of z distributions for real data and MonteCarlo: on the left using for data the value $M_\eta = 547.30$ MeV and on the right the value $M_\eta = 547.82$ MeV. In the old approach we can see two different slopes, while in the new one it is possible to fit with a straight line in the physical range. Let me stress that this is a rough evaluation of the slope parameter α , in which resolution effects are not correctly included.

In order to give the final result for the slope parameter α the fit range (0–1), correspondent to the allowed region of the phase space, will be utilized.

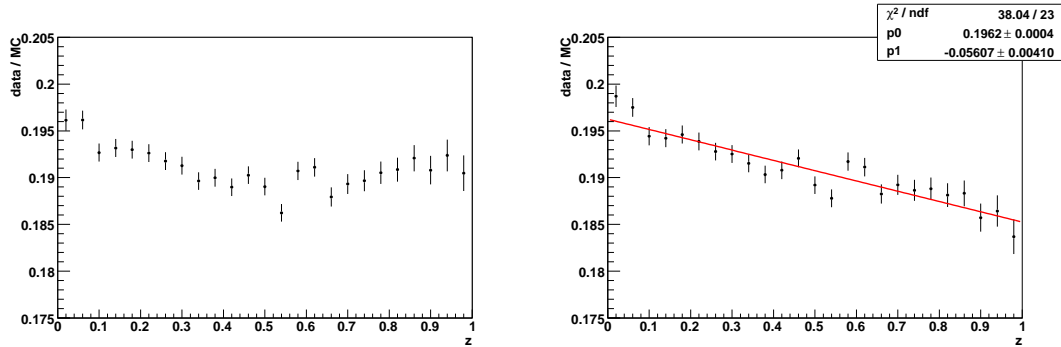


Figure 5.10: *Data-MonteCarlo ratio of the z distribution obtained using on data. Left: $M_\eta = 547.30$ MeV; right: $M_\eta = 547.822$ MeV; the linear fit is superimposed. Note that p_1 equals to two times the slope parameter α .*

5.6 The systematic checks

As we have seen, the whole analysis relies heavily on the behaviour of MonteCarlo simulation. In order to evaluate the systematical uncertainty of the measured value of the parameter α one has to obtain good agreement between the real and the MonteCarlo data.

Good agreement should be obtained in reproducing the experimental resolutions, efficiencies, and the background. We have also studied the slope parameter α moving the fit range and taking into account the systematic error on the η mass, eq. (5.9). A summary of systematic uncertainties is reported in Table 5.6.

5.6.1 Systematics on resolution

In order to study the calorimeter energy response, we considered the energy related variables used in the construction of the χ^2 discriminating tool, i.e. the M_π and the E_γ . In Figures 5.11 and 5.12 the comparison of these distributions between data and MonteCarlo is shown. The MonteCarlo histograms are normalized to the same number of events of the data sample. The agreement is very good on all spectra, and is evident in both linear and logarithmic scale. The small discrepancy in the photons energy spectrum has been used in correcting the MonteCarlo efficiency (see Section 5.6.2).

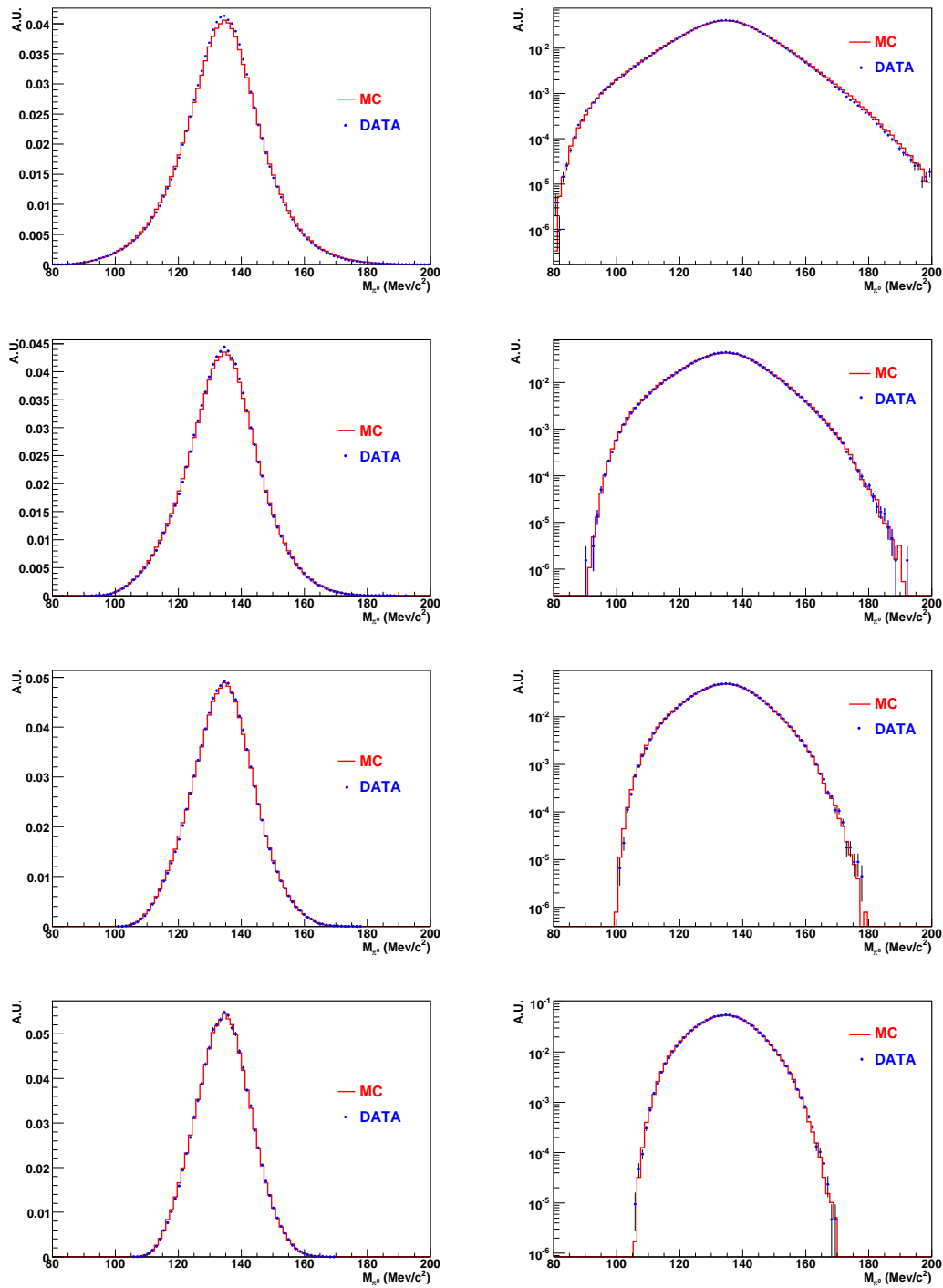


Figure 5.11: *Data-MonteCarlo comparison on invariant mass of π^0 . From top to bottom: Low purity, Medium purity I, Medium purity II, High purity samples. Left: linear scale. Right: log scale.*

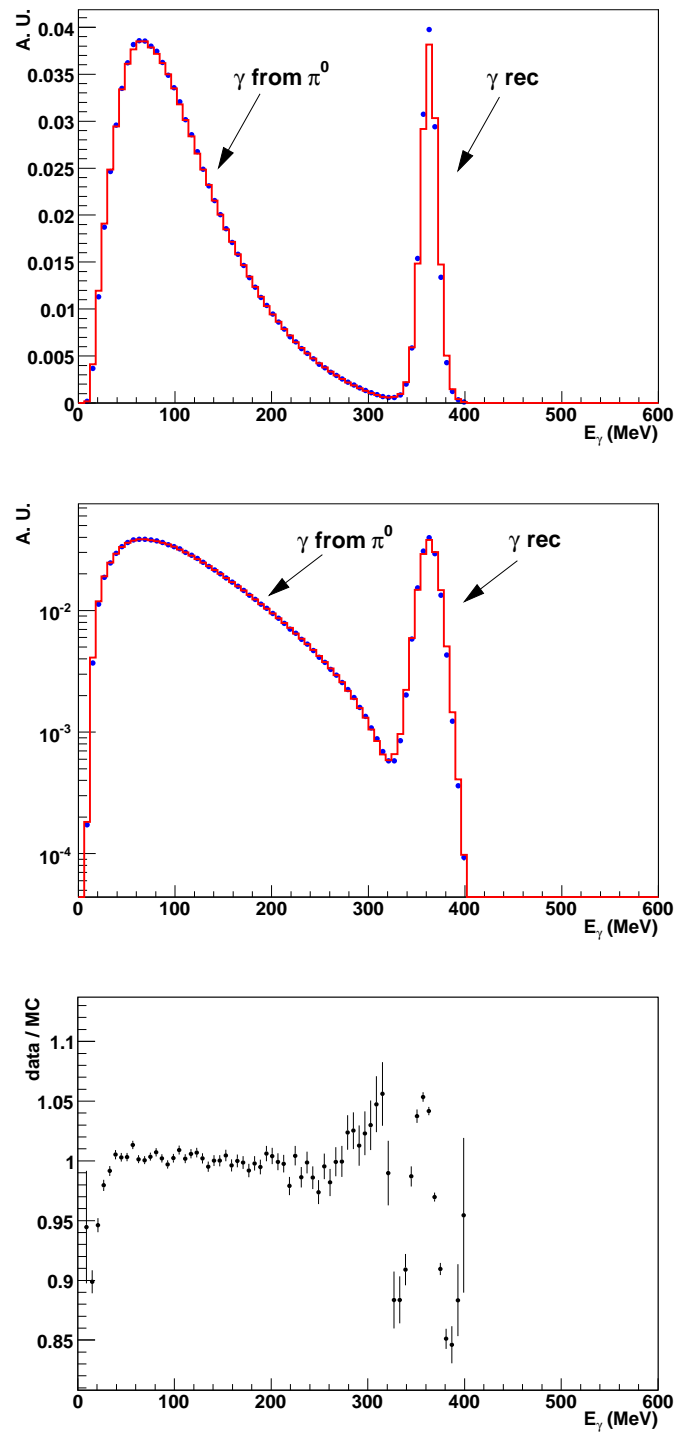


Figure 5.12: Photons energy spectrum data (dots) are compared to MonteCarlo (solid). Top: linear scale. Center: log scale. Bottom: bin by bin normalized data-MonteCarlo discrepancy.

Since in the center of Dalitz plot, $z = 0$, the 3 pions have the same energy value

$$E_{\pi^0} = \frac{M_\eta}{3} \quad (5.11)$$

a good check of the MonteCarlo performance in evaluating the energy resolution of π^0 in the η -rest frame comes from the distribution of “ $E_{\pi^0} - \frac{M_\eta}{3}$ ” in the bin $z = 0$. The results of this check are shown in Figure 5.13. Again, comparison between data and MonteCarlo is very satisfactory; we correctly reproduce the resolution in the center of Dalitz-plot independently from the purity sample.

A further check can be done comparing the energies of the two photons in the pion rest frame as function of pion energy. We divided the spectrum in bins of 10 Mev and for each bin we plotted the difference $E_{\gamma_1} - E_{\gamma_2}$ both for data and MonteCarlo. We reported the RMS of the obtained distributions as function of pion energy, see Figure 5.14.

A data MonteCarlo discrepancy at level of $1 \div 2\%$ is observed. We take care of this discrepancy in the parameter evaluation redefining, for each MonteCarlo event, z_{rec} as:

$$z'_{rec} = z_{gen} + \eta(z_{rec} - z_{gen}) \quad (5.12)$$

where η is obtained from the fit to the data-MonteCarlo ratio in Figure 5.14. We have performed the measurement of the slope parameter α using this correction, see Table 5.3.

Range	Low Pur.	Medium Pur. I	Medium Pur. II	High Pur.
(0,1)	-0.037 ± 0.002	-0.035 ± 0.003	-0.029 ± 0.003	-0.025 ± 0.005

Table 5.3: *Fitted results for the slope parameter α taking into account the data MonteCarlo discrepancy on resolution.*

For each sample with different purity, we quote as systematic uncertainty due to the resolution the difference between the two values obtained with and without the correction, see Table 5.6.

5.6.2 Systematics on efficiency evaluation

The MonteCarlo goodness in reproducing the efficiency has been evaluated with the following procedure.

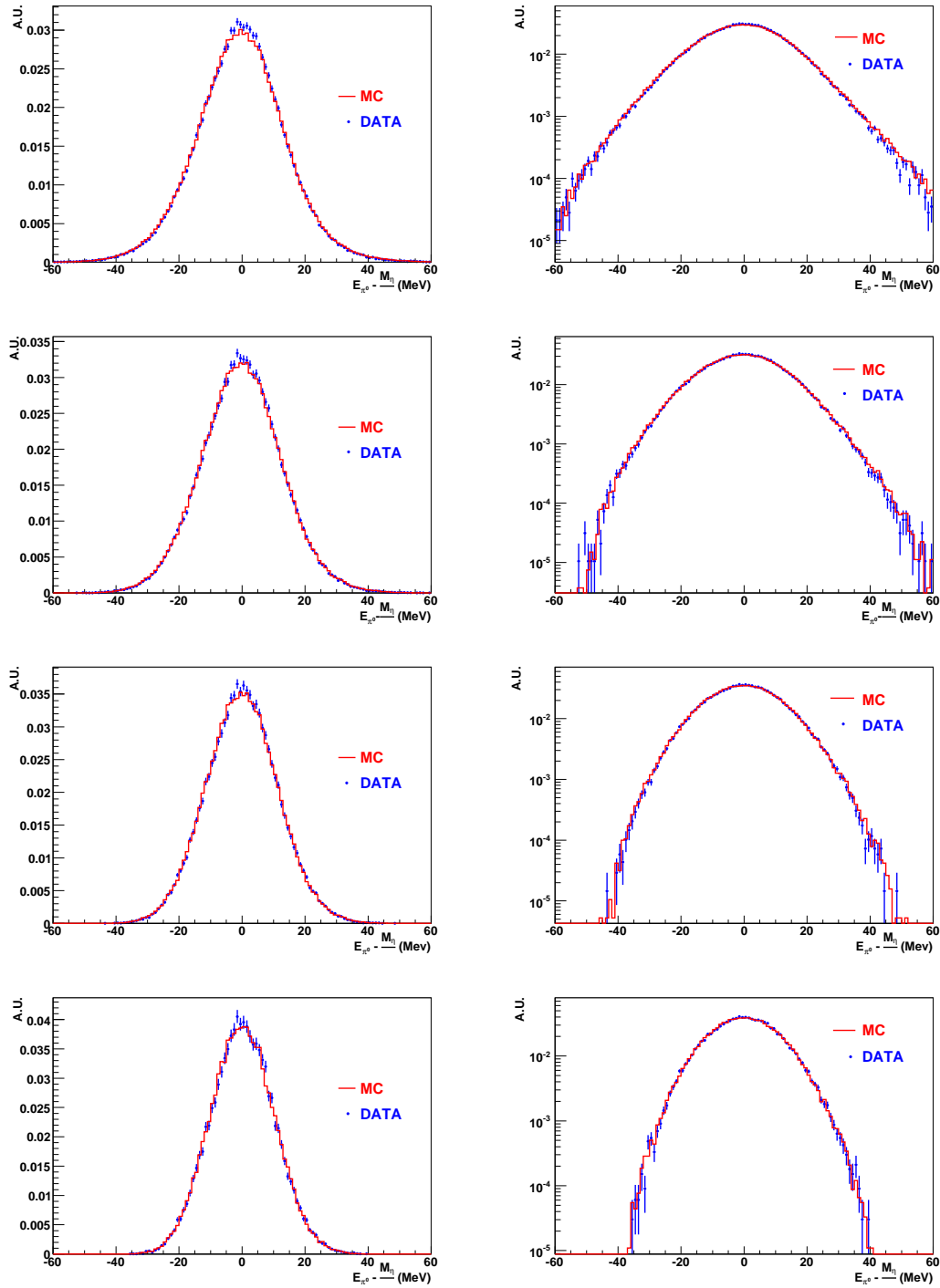


Figure 5.13: Comparison data vs Monte Carlo for the distribution of $E_{\pi^0} - \frac{M_{\pi^0}}{3}$ in the bin $z = 0$. From top to bottom: Low purity, Medium purity I, Medium purity II, High purity samples. Left: linear scale. Right: log scale.

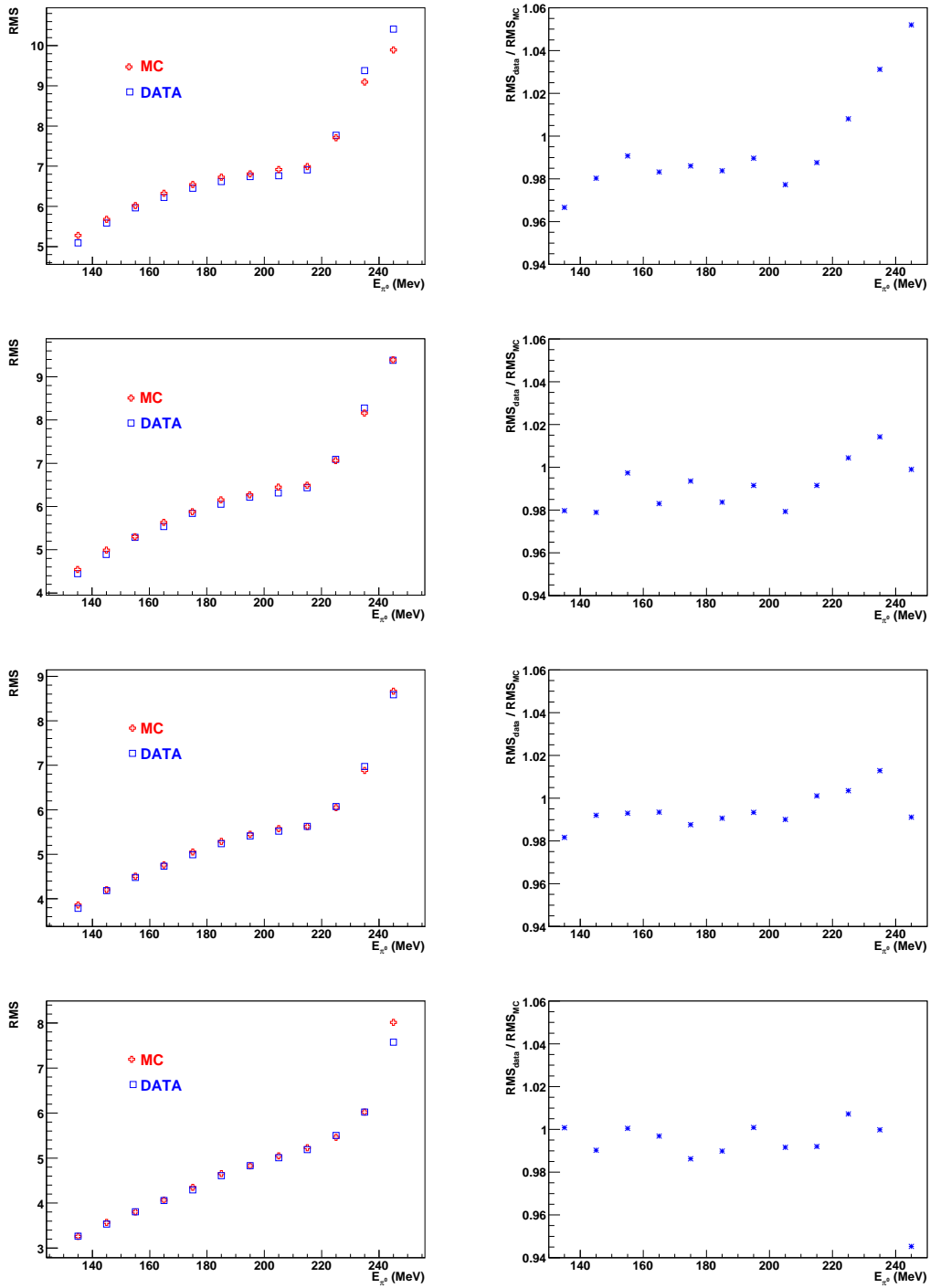


Figure 5.14: From top to bottom: Low purity, Medium purity I, Medium purity II, High purity samples. Left: distribution of the RMS in bins of E_{π^0} . Right: data MonteCarlo discrepancy in the RMS distribution.

For each sample with different purity-efficiency, we consider the number of events selected on data (see Section 5.4) and, using as a normalization sample the Low purity one, we evaluate:

$$\begin{aligned}\frac{N_2}{N_1} &= 0.6289 \pm 0.0009 \\ \frac{N_3}{N_1} &= 0.4332 \pm 0.0007 \\ \frac{N_4}{N_1} &= 0.2068 \pm 0.0005\end{aligned}$$

The comparison with the expected ones:

$$\begin{aligned}\left(\frac{N_2}{N_1}\right)^{exp} &= 0.6194 \pm 0.0232 \\ \left(\frac{N_3}{N_1}\right)^{exp} &= 0.4196 \pm 0.0161 \\ \left(\frac{N_4}{N_1}\right)^{exp} &= 0.1971 \pm 0.0073\end{aligned}$$

is satisfactory.

Note that the expected ratios coincide with the relative efficiency ratios evaluated on MonteCarlo $\frac{\varepsilon_2^{MC}}{\varepsilon_1^{MC}}, \frac{\varepsilon_3^{MC}}{\varepsilon_1^{MC}}, \frac{\varepsilon_4^{MC}}{\varepsilon_1^{MC}}$. As a result we can conclude that the factor scale of the efficiencies is well reproduced by MonteCarlo simulation. A correction to low energy photon efficiency is applied weighting the MonteCarlo events. For the photon efficiencies we have used a data-MonteCarlo photon efficiency ratio

$$1 - \exp\left(-\frac{E_\gamma}{d}\right) \quad (5.13)$$

where $d = 8.1$ MeV (compare with [51]). This function has been obtained fitting the photon energy data–MonteCarlo discrepancy, see Figure 5.12.

The ratio between the efficiency weighed and no as function of z is shown in Figure 5.15. A different slope for the sample with different purity at level of few per mill, is present. For each sample we assumed the value of the fitted slopes as systematic uncertainty due to the correction to low energy photon efficiency, see Table 5.6.

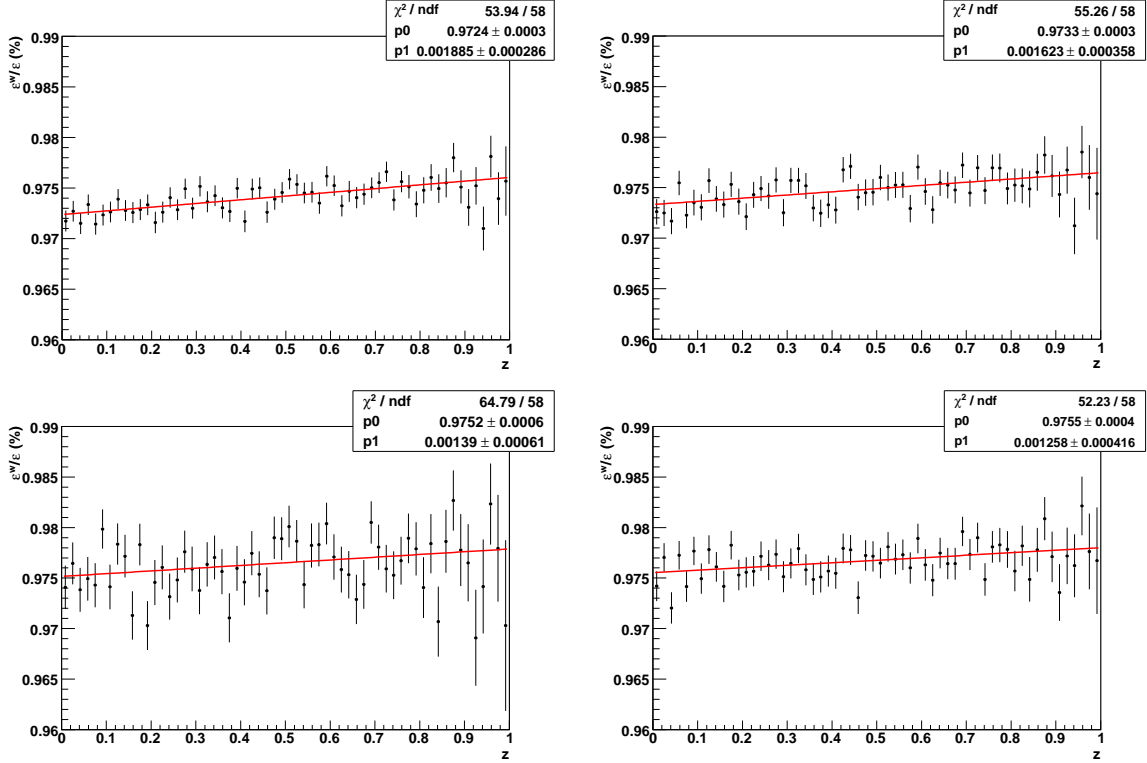


Figure 5.15: Ratio between weighed and not weighed efficiencies as function of z . The errors take into account the correlations between the efficiencies. From top left in clockwise direction: for Low, Medium I, Medium II, High purity samples.

5.6.3 Systematics on background evaluation

We have grouped the sources of systematics on the background estimation in two items:

1. physical background
2. combinatorial background

1) The $\phi \rightarrow \eta\gamma \rightarrow 7\gamma$ is essentially “background free” at KLOE. The only processes which could mimic our decay are $\phi \rightarrow K_S K_L$ events, with the K_L decaying near the IP and either five π^0 's in final state, with 3 photons getting lost, or the CP violating four π^0 's final state with one photon getting lost.

This two channel have the following branching fraction:

$$BR(\phi \rightarrow K_L K_S \rightarrow 3\pi^0 + 2\pi^0) = 0.022$$

$$BR(\phi \rightarrow K_L K_S \rightarrow 2\pi^0 + 2\pi^0) = 9.77 \times 10^{-5}$$

negligible compared with the $\phi \rightarrow \eta\gamma \rightarrow 7\gamma$. Using a MonteCarlo sample simulated with run condition from 2001÷2002 data taking we found a background contamination due to neutral kaon decays at level of 0.1%.

This background has no effect on this analysis.

2) We have evaluated the composition of background on data by using the TFractionFitter method insert in a stand alone Minuit program [48].

To estimate the background we have used the distribution of z for the second best combination, $z_{\chi_1^2}$, since it is important to evaluate the background with a variable different from that used to measure the slope parameter. In such way, possible correlations that can affect the parameter evaluation are excluded.

However the same results are obtained by using other variables, e.g. $\chi_1^2 - \chi_2^2$ (difference between the best and second best combination). Thus we fit $z_{\chi_1^2}$ distribution on data with the MonteCarlo shapes of the right and wrong photon pairing. This procedure has been succesful tested on MonteCarlo; we correctly reproduce the background fraction expected:

$$1 - P_{fitted} = (15.54 \pm 0.21)\% \quad 1 - P_{expected} = 15.5\% \text{ Low Purity}$$

$$1 - P_{fitted} = (7.92 \pm 0.25)\% \quad 1 - P_{expected} = 8.0\% \text{ Medium Purity I}$$

$$1 - P_{fitted} = (5.20 \pm 0.30)\% \quad 1 - P_{expected} = 5.2\% \text{ MediumPurity II}$$

$$1 - P_{fitted} = (2.40 \pm 0.40)\% \quad 1 - P_{expected} = 2.45\% \text{ High Purity}$$

The results on data are the following:

$$1 - P_{fitted} = (16.60 \pm 0.28)\% \quad \text{Low Purity}$$

$$1 - P_{fitted} = (8.98 \pm 0.37)\% \quad \text{Medium Purity I}$$

$$1 - P_{fitted} = (6.40 \pm 0.45)\% \quad \text{MediumPurity II}$$

$$1 - P_{fitted} = (3.47 \pm 1.00)\% \quad \text{High Purity}$$

Comparing the results with the expected ones from MC we observe a discrepancy at level of 8%, 14%, 23% and 45% respectively for Low, Medium I, Medium II and High purity sample.

In Figure 5.16 the composition of background is shown. The effect in the slope parameter measurement due to the combinatorial background has been evaluated weighting the events with a wrong photon pairing, for the observed

Range	Low Pur.	Medium Pur. I	Medium Pur. II	High Pur.
(0,1)	-0.038 ± 0.002	-0.037 ± 0.003	-0.032 ± 0.003	-0.028 ± 0.005

Table 5.4: *Fitted results for the slope α taking into account the data MonteCarlo discrepancy in combinatorial background evaluation.*

discrepancy; the fit results are reported in Table 5.4.

For each sample with different purity, we quote as systematic uncertainty due to the combinatorial background the difference between the two values obtained weighting and not weighting for the data MonteCarlo discrepancy, see Table 5.6.

5.6.4 M_η value on data

We have performed the measurement of the slope parameter α taking into account the systematic error on the η mass (± 0.069 MeV), Table 5.5. We quote the effect of the M_η value on the slope parameter α using the our standard definition of systematic uncertainty, see Table 5.6.

	Low Pur.	Medium Pur. I	Medium Pur. II	High Pur.
$M_{\eta I}$	-0.037 ± 0.002	-0.035 ± 0.003	-0.030 ± 0.003	-0.027 ± 0.004
$M_{\eta II}$	-0.032 ± 0.002	-0.031 ± 0.003	-0.026 ± 0.003	-0.023 ± 0.004

Table 5.5: *Fitted results for the slope parameter α : where $M_{\eta I} = (547.822 + 0.069)$ MeV, and $M_{\eta II} = (547.822 - 0.069)$ MeV.*

5.6.5 Fit range

As we have shown in Section 5.5, the fit procedure has been repeated using different fit range and the final evaluation for the slope parameter α has been given for the range (0–1), correspondent to the allowed region of the phase

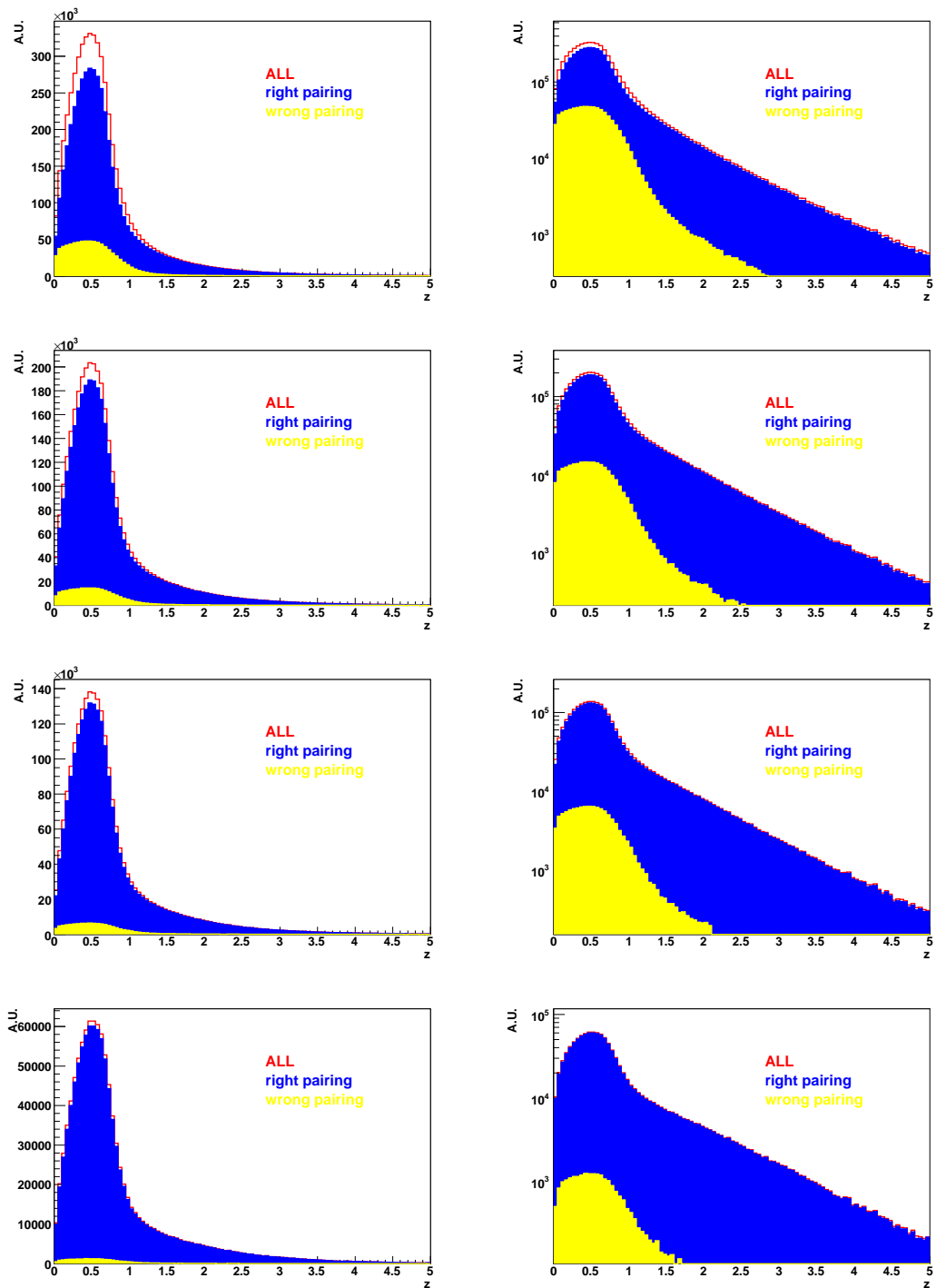


Figure 5.16: Background composition. From top to bottom: Low purity, Medium purity I, Medium purity II, High purity samples. Left: linear scale. Right: log scale.

space.

The systematic effect associated to this choice has been evaluated considering for each sample with different purity, the maximum and the minimum deviation of the slope parameter α from the choice value, see Table 5.6.

The systematic uncertainties on the measured slope parameter α are summarized in Table 5.6.

	Low Pur.	Medium Pur. I	Medium Pur. II	High Pur.
Res	-0.002	-0.002	-0.001	0.
Low E_γ	-0.0019	-0.0016	-0.0013	-0.0014
BKG	-0.003	-0.004	-0.004	-0.003
M_η	-0.002 + 0.003	-0.002 + 0.002	-0.002 + 0.002	-0.002 + 0.002
Range	-0.003	-0.002 + 0.001	+0.003	+0.004
Total systematic uncertainties				
	-0.005/ +0.003	-0.006/ +0.002	-0.005/ +0.004	-0.004/ +0.004

Table 5.6: Summary table of systematic uncertainties. The total systematic uncertainty is obtained as square root of the sum of the square of each term.

5.7 Results

We give the final result for the slope parameter α in correspondence of the sample with High Purity, about 250000 $\eta \rightarrow 3\pi^0$ decays; and we quote as systematic uncertainty due to the purity, the maximum observed variation of α .

The result including the statistical uncertainty from the fit and the estimate systematic is:

$$\alpha = -0.025 \pm 0.004 (stat) {}^{+0.004}_{-0.011} (syst) \quad (5.14)$$

Figure 5.17 shows a comparison between data and fitted function as function of the Dalitz plot variable z .

The result is within errors compatible with the result from Crystall Ball [42] based on 10^6 events

$$\alpha = -0.031 \pm 0.004 \quad (5.15)$$

Moreover the fitted slope parameter α agrees with the calculations from the chiral unitary approach [39].

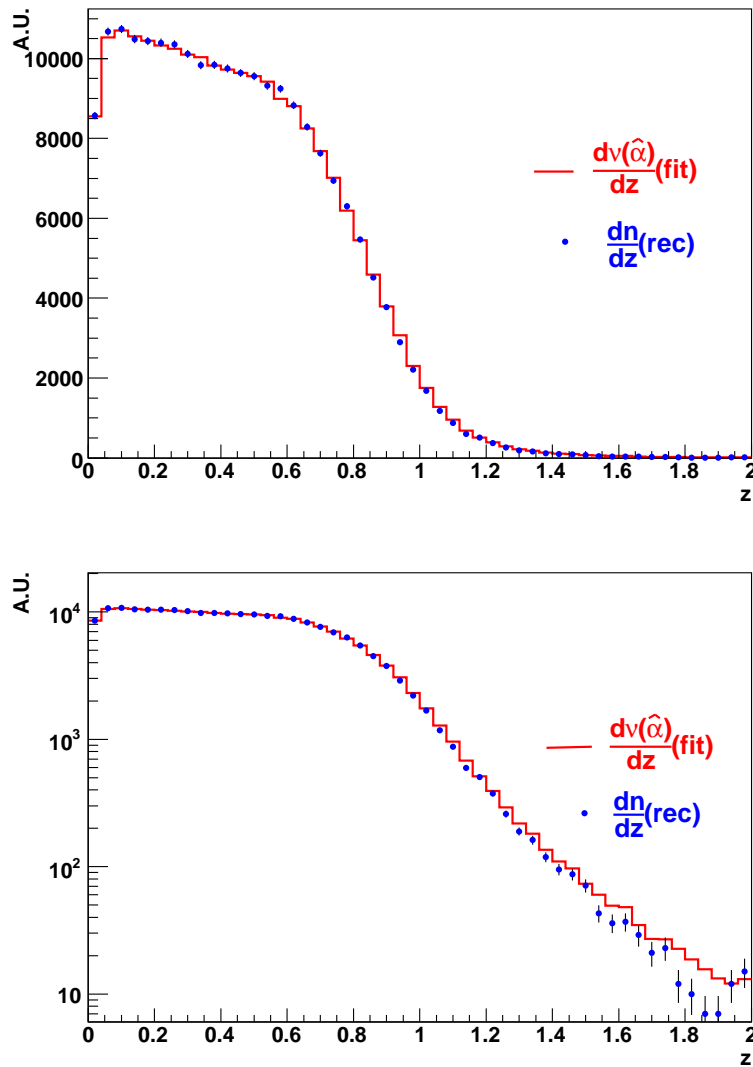


Figure 5.17: Comparison between data and fitted function. Blue points are data and the histogram is the function.

Conclusions

A measurement of the slope parameter α of the Dalitz plot for the $\eta \rightarrow 3\pi^0$ decay has been performed in the work carried out for this thesis, based on the data statistics collected by KLOE in years 2001 and 2002 corresponding to an integrated luminosity of 418 pb^{-1} .

The square of transition amplitude is expressed as a linear parametrization: $|\mathcal{A}|^2 \sim 1 + 2\alpha z$ in which the z variable is function of the pion energy and the parameter α describes the differences of the $\eta \rightarrow 3\pi^0$ decay from the pure phase space.

A very large MonteCarlo sample ($\sim 25 \cdot 10^6 \eta \rightarrow 3\pi^0$) has been used to develop a method of pairing photon to right π^0 based on a pseudo χ^2 -variable. With the selection criteria (see Chapter 4) four samples with different efficiencies and purity (fraction of event with all photons correctly matched to π^0 's) has been analyzed.

A kinematic fit which imposes the mass of three pions has been developed to improve the resolution on the Dalitz variable z .

The $\phi \rightarrow \eta\gamma \rightarrow 7\gamma$ is essentially background free at KLOE. In order to estimate the value of the parameter α the Maximum Likelihood approach has been used. The developed fit procedure automatically takes into account the resolution and efficiency in the unbinned way. This procedure has been tested on MonteCarlo pointing out no appreciable distortion in the α evaluation.

The whole analysis relies heavily on the behaviour of MonteCarlo simulation. In order to evaluate the systematical uncertainty of the measured value of the parameter α the data MonteCarlo agreement in reproducing the experimental resolution, efficiencies and the combinatorial background has been tested.

The final measurement for the slope parameter α has been obtained from a data sample of about $\sim 250000 \eta \rightarrow 3\pi^0$ events; for this sample the purity and the selection efficiency are respectively $\sim 98\%$ and $\sim 4.3\%$.

We found:

$$\alpha = -0.025 \pm 0.004 (stat) \begin{matrix} +0.04 \\ -0.011 \end{matrix} (syst)$$

The largest systematic contribution to the error is given by the purity. The our measurement for the slope parameter α agrees with the most recent experimental result:

$$\alpha = -0.031 \pm 0.004 [42]$$

and with the theoretical calculations within chiral unitary approach:

$$\alpha = -0.031 [39]$$

Appendix A

A.1 The method of maximum likelihood

“From a theoretical point of view, the most important general method of estimation so far known is the *method of maximum likelihood*” [52]. We suppose that a set of N independently measured quantities x_i came from a p.d.f. $f(x; \boldsymbol{\theta})$, where $\boldsymbol{\theta} = (\theta_1, \dots, \theta_n)$ is a set of n parameters whose value are unknown. The method of maximum likelihood takes the estimators $\hat{\boldsymbol{\theta}}$ to be those value of $\boldsymbol{\theta}$ that maximize the *likelihood function*,

$$L(\boldsymbol{\theta}) = \prod_{i=1}^N f(x_i; \boldsymbol{\theta}) \quad (\text{A.1})$$

The likelihood function is the joint p.d.f. for the data, evaluated with the data obtained in the experiment and regarded as a function of the parameters. Note that the likelihood function is not a p.d.f. for the parameters $\boldsymbol{\theta}$; in frequentistic statistics this is not defined.

It is usually easier to work with $\ln L$, and since both are maximized for the same parameter values $\boldsymbol{\theta}$, the maximum likelihood (ML) estimators can be found by solving the *likelihood equations*,

$$\frac{\partial \ln L}{\partial \theta_i} = 0 \quad i = 1, \dots, n \quad (\text{A.2})$$

Maximum likelihood estimators are important because they are approximately unbiased and efficient for large data samples, under quite general conditions, and the method has a wide range of applicability.

In evaluating the likelihood function, it is important that any normalization factors in the p.d.f. that involve $\boldsymbol{\theta}$ be included. However, we will only be interested in the maximum of L and in ratios of L at different values of the

parameters; hence any multiplicative factors that do not involve the parameters that we want to estimate may be dropped, including factors that depend on the data but not on $\boldsymbol{\theta}$.

Under a one-to-one change of parameters from $\boldsymbol{\theta}$ to $\boldsymbol{\eta}$, the ML estimators $\hat{\boldsymbol{\theta}}$ transform to $\boldsymbol{\eta}(\hat{\boldsymbol{\theta}})$. That is, the ML solution is invariant under change of parameter. However, other properties of ML estimators, in particular the bias, are not invariant under change of parameter.

The inverse V^{-1} of the covariance matrix $V_{ij} = \text{cov}[\hat{\theta}_i, \hat{\theta}_j]$ for a set of ML estimators can be estimated by using

$$\left(\hat{V}^{-1}\right)_{ij} = -\frac{\partial^2 \ln L}{\partial \theta_i \partial \theta_j} \Big|_{\hat{\boldsymbol{\theta}}}. \quad (\text{A.3})$$

For finite samples, however, Eq. (A.1) can result in an underestimate of the variances. In the large sample limit (or in a linear model with Gaussian errors), L has a Gaussian form and $\ln L$ is (hyper)parabolic. In this case it can be seen that a numerically equivalent way of determining s -standard-deviation errors is from the contour given by the $\boldsymbol{\theta}'$ such that

$$\ln L(\boldsymbol{\theta}') = \ln L_{max} - \frac{s^2}{2} \quad (\text{A.4})$$

where $\ln L_{max}$ is the value of $\ln L$ at the solution point.

The extreme limits of this contour on the θ_i axis give an approximate s -standard-deviation confidence interval for θ_i .

In the case where the size n of the data sample x_1, \dots, x_n is small, the unbinned maximum likelihood method, i.e., use of equation A.1, is preferred since binning can only result in a loss of information and hence larger statistical errors for the parameter estimates. The sample size n can be regarded as fixed or the user can choose to treat it as “extended maximum likelihood”. If the sample is large it can be convenient to bin the values in a histogram, so that one obtains a vector of data $\mathbf{n} = (n_1, \dots, n_N)$ with expectation values $\boldsymbol{\nu} = E[\mathbf{n}]$ and probabilities $f(\mathbf{n}; \boldsymbol{\nu})$. Then one may maximize the likelihood function based on the contents of the bins (so i labels bins). This is equivalent to maximizing the likelihood ratio $\lambda(\boldsymbol{\theta}) = f(\mathbf{n}; \boldsymbol{\nu}(\boldsymbol{\theta})) / f(\mathbf{n}; \mathbf{n})$, or to minimizing the quantity [53]

$$-2 \ln \lambda(\boldsymbol{\theta}) = 2 \sum_{i=1}^N \left[\nu_i(\boldsymbol{\theta}) - n_i + n_i \ln \frac{n_i}{\nu_i(\boldsymbol{\theta})} \right] \quad (\text{A.5})$$

where in bins where $n_i = 0$, the last term in A.1 is zero. In the limit of zero bin width, maximizing A.1 is equivalent to maximizing the unbinned

likelihood function A.1.

A benefit of binning is that it allows for a goodness-of-fit test. The minimum of $-2 \ln \lambda$ as defined by Eq. A.1 follows a χ^2 distribution in large sample limit. If there are N bins and m fitted parameters, then the number of degree of freedom for the χ^2 distribution is $N - m - 1$ if the data are treated as a multinomially distributed and $N - m$ if the n_i are Poisson variables with $\nu_{tot} = \sum \nu_i$ fixed. if the n_i are Poisson distributed and ν_{tot} is also fitted, then by minimizing Eq. A.1 one obtains that the area under the fitted function is equal to the sum of the histogram contents, i.e., $\sum \nu_i = \sum n_i$. This is not the case for parameter estimation methods based on a least-squares procedure with traditional weights.

Bibliography

Bibliography

- [1] “*The DAΦNE Physics handbook*”, Ed. L. Maiani, G. Pancheri e N. Paver, I.N.F.N. L.N.F. (1995).
- [2] K. Hagiwara, *et al.*, *J. Phys. G: Nucl. Part. Phys.* **33**, (2006).
- [3] F. Ambrosino *et al.* “*The tracking detector of the KLOE experiment*”, *Nucl. Inst. Meth. A* **488**, 1-23 2002.
- [4] M. Adinolfi *et al.* “*The KLOE electromagnetic calorimeter*”, *Nucl. Inst. Meth. A* **482** (2002) 363-385.
- [5] S. Bertolucci *et al.*, “*The LADON test beam of EMCAL: a full report on the data analysis*” KLOE note (62) (1993).
- [6] A. Aloisio *et al.* “*The KLOE Trigger System*”, LNF-96/043(IR) (1996).
- [7] A. Aloisio *et al.* “*The KLOE Data Acquisition system, addendum to the KLOE technical proposal*”, LNF-95/014(IR) (1995).
- [8] R. Brun *et al.* GEANT3, CERN-DD/EE/84-1 (1984).
- [9] R. Brun *et al.* GEANT: Simulation for particle physics experiments, user guide and reference manual, CERN-DD-78-2-REV (1978).
- [10] C. M. Carloni Calame *et al.* *The BABAYAGA event generator*, hep-ph/0312014 (2003).

-
- [11] F. Ambrosino *et al.* *Phys. Lett. B* in print, hep-ex/0508027.
- [12] F. Ambrosino *et al.* *Phys. Lett. B* **626**, (2005) 15-23.
- [13] F. Ambrosino *et al.* *Phys. Lett. B* **632** (2006) 76.
- [14] H. Leutwyler, M. Roos *Z. Phys. C* **25** (1984) 25.
- [15] W. J. Marciano *Phys. Rev. Lett.* **93** (2004) 231803.
- [16] C. Bernard *et al.* PoS *LAT2005* (2005) 025.
- [17] W. J. Marciano, A. Sirlin, *Phys. Rev. Lett.* **96** (2006) 032002.
- [18] N. N. Achasov, V. N. Ivanchenko, *Nucl. Phys. B* **315** (1989) 465.
- [19] G. Isidori, L. Maiani, S. Pacetti, *private communication*.
- [20] M. Boggione, M.R. Pennington, *Eur. Phys. J. C* **30** (2003) 503.
- [21] N. N. Achasov, A. V. Kiselev, hep-ph/0512047.
- [22] C. Di Donato *et al.*, KLOE *note* (214) (2006).
- [23] A. Bramon, R. Escribano, M. D. Scadron *Eur. Phys. J. C* **7** (1999) 271.
- [24] G. W. Bennett *et al.* *Phys. Rev. Lett.* **92**, (2004) 161802.
- [25] R. R. Akhmetshin *et al.* *Phys. Lett. B* **527**, (2002) 161.

-
- [26] R. R. Akhmetshin *et al.* *Phys. Lett.* **B578**, (2004) 285.
- [27] M. Davier, S. Eidelman, A. Höcker, Z. Zhang *Eur. Phys. J.* **C31**, (2003) 503.
- [28] S. Binner, J. H. Kuhn, K. Melnikov, *Phys. Lett.* **B459**, 279-287, (1999).
- [29] H. Czyz *et al.* *Eur. Phys. J.* **C27**, (2003) 563.
- [30] J. Gasser, H. Leutwyler, *Nucl. Phys.* **B250** (1985) 465; 517; 539.
- [31] S. Weinberg, *Physica* **A96** (1979) 327.
- [32] H. Weyl, *Symmetry*, Princeton University Press, Princeton (1964).
- [33] See, e.g. J. D. Bjorken, S. D. Drell, *Relativistic Quantum Fields*, McGraw-Hill, New York (1964).
- [34] D. G. Sutherland *Phys. Lett.* **23** (1966) 384.
- [35] M. Walker, $\eta \rightarrow 3\pi$ *Master Thesis*. Bern University (1998).
- [36] A. V. Anisovich, H. Leutwyler, *Phys. Lett.* **B375** (1996) 335.
- [37] J. Kambor, C. Wiesendanger, D. Wyler *Nucl. Phys.* **B465**, (1996) 215.
- [38] B. Holstein, *Physica Scripta* **T99** (2002) 55-67.
- [39] B. Borasoy, R. Niler hep-ph/0510384 v2 (2005).
- [40] D. Alde *et al.*, *Z. Phys.* **C25**, (1984) 225.

- [41] Crystal Barrel collaboration, *Phys. Lett.* **B417**, (1998) 193.
- [42] Crystal Ball collaboration, *Phys. Rev. Lett.* **87**, (2001) 19.
- [43] A. Antonelli *et al.*, *A short description of the track reconstruction program with the KLOE drift chamber*, KLOE note (157) (1996).
- [44] M. Incagli *et al.*, *VTXFIN: the KLOE Vertex Finder Algorithm*, KLOE memo (147) (1996).
- [45] K. W. Edwards *et al.*, “*The Argus Vertex Drift Chamber*”, *Nucl. Instrum. Meth. A* **252** (1986) 384.
- [46] P. De Simone *et al.*, “*Studio di tecniche sperimentali per la ricostruzione del decadimento $K_L^0 \rightarrow \pi^+\pi^-$ nell’esperimento KLOE a DAΦNE*” Ph.D. Thesis, Università degli Studi di Roma “La Sapienza”, (1994).
- [47] A. G. Frodesen *et al.*, “*Probability and Statistics in Particle Physics*” Oxford University Press, (1979).
- [48] B. Grinstein, S. J. Rey, M. B. Wise, *Phys. Rev.* **D33** (1986) 1495.
- [49] A. Denig and F. Nguyen, KLOE note (202) (2006).
- [50] B. Di Micco *Acta Phys. Slov.* **56** (2005).
- [51] M. Palutan *et al.*, KLOE note (174) (2002).
- [52] H. Cramer “*Mathematical methods of statistics*” Princeton Univ. Press, New Jersey (1958). (1967).
- [53] S. Baker, R. Cousins, “*Nucl. Instrum. Methods*” **221**, 437 (1984).
- [54] F. Jacquet *et al.* *Phys. Lett. 25 B* **574**, (1967).
- [55] F. Jacquet, U. Nguyen-Khac, A. Haatfut, A. Halsteinslid, *Nuovo Cimento* **63 A** (1969) 743.

-
- [56] W. Kim *et al.*, *The clustering algorithm for KLOE calorimeter*, KLOE Memo 6, (1995).
- [57] A. Aloisio *et al.*, “*The KLOE Collaboration*”, *Phys. Lett.* **B538**, 21-26, (2002).
- [58] F. Jegerlehner, “*DESY-03-170*” hep-ph/0310234, (2003).